SCUOLA NORMALE SUPERIORE

Classe di Scienze

Corso di perfezionamento in

Neuroscienze

XXII ciclo

Genetic and environmental factors regulating structure, function and plasticity of the visual cortex

Settore Scientifico Disciplinare **BIO/09**

Candidato
dr. Leonardo Lupori

Relatore/i

prof. Tommaso Pizzorusso

Anno accademico 2022/2023

A mamma e papà

Contents

An introductory overview

0.1 Preamble

Dear reader,

in this thesis, I will present the results that I obtained during my Ph.D. course. I studied the factors that regulate structure, function, and plasticity in the cerebral cortex, with a particular focus on the visual cortex.

The foundation of much of what we know about the development and plasticity of the cortex was laid thanks to the seminal work of Hubel and Wiesel in the 1960s. They not only described fundamental features of neuronal response properties to visual stimulation but also revealed that during postnatal development, the visual cortex undergoes a critical period of dramatic experience-dependent plasticity. These discoveries made the visual cortex one of the most used areas of the brain to investigate plasticity, and paved the way for many decades of research on the mechanisms that regulate plastic phenomena in the central nervous system. Understanding such mechanisms would have invaluable implications. From the basic research point of view, synaptic plasticity is thought to underlie essential cognitive processes like learning and memory. Instead, from the clinical point of view, a precise knowledge of possible methods to increase or decrease neuroplasticity could improve the treatment of many pathological conditions including brain injuries, stroke, cognitive decline, and neurodevelopmental disorders.

Plasticity in the visual cortex can be regulated by both intrinsic (i.e., inside the brain itself) factors, like genetic programs or spontaneous activity, and extrinsic (i.e., peripheral or external) ones, like sensory experience and interaction with the environment. Moreover, the postnatal development of visual cortical circuits is also well studied and is characterized by structural and functional developmental milestones that are indicative of the maturation of the circuits after birth. This feature makes the visual cortex an appealing model for studying functional alteration in neurodevelopmental disorders models.

In this thesis, I tried to address these themes from different perspectives and, for this reason, this document will be split into three main parts.

Part I

In the first part (Part I), I studied how extrinsic stimuli coming from the environment can modulate the plasticity of the central nervous system. A lifestyle characterized by a rich set of multisensory, social and motor stimuli, is able to promote neuroplasticity. In animal models, this has often been modelled by raising animals in an *enriched environment* (EE), characterized by larger cages, with more animals, access to a running wheel and periodic rearrangements of toys. This experimental manipulation results in an increase in cortical plasticity and many mechanisms of action have been proposed to explain how environmental stimuli can exert this effect on the brain. Most of the research on this theme, however, focused on searching such mechanisms into the brain itself, however EE

is by nature a global manipulation that influences the whole body. In this part, I analyzed the effect of EE on the gut microbiome and tested the hypothesis that the EE-induced modulation of the gut microbiome might be one of the mechanisms by which EE enhances neuroplasticity.

Part II

Neuronal circuits in the brain are often immature at birth and necessitate of a postnatal phase of maturation. During these periods of heightened plasticity, called critical periods, neural activity, driven by the sensory experience of the external world, can profoundly shape brain wiring. One of the hallmarks of the closure of critical periods is the aggregation of reticular structures called perineuronal nets (PNNs) around a subset of inhibitory neurons in the brain. These structures, intrinsic to the brain, belong to the extracellular matrix and are composed of many molecules including chondroitin sulfate proteoglycans. A great amount of studies throughout cortical and subcortical regions implicated PNNs in the control of plasticity, however we still lack a systematic description of the distribution of PNNs in the entire mouse brain. The second part (Part II) aims at generating a highly quantitative whole-brain atlas of PNNs and parvalbumin-positive interneurons, that are thought to be preferentially enwrapped by PNNs. The dataset generated in this project will serve as a base to generate novel hypotheses, highlight interesting questions, and design experiments to better understand the function of PNNs and their implication in pathological conditions.

Part III

Alterations in the plasticity mechanisms of postnatal circuit maturation can give rise to neurodevelopmental disorders. In the third part (Part III) I used the visual cortex as a model circuit to study cortical function in a mouse model of CDKL5 deficiency disorder. Understanding functional correlates of the lack of the CDKL5 protein *in-vivo* might, on one side, provide insight on the cellular processes that are altered in the disease, and on the other, could reveal quantitative biomarkers that can be used to measure disease progression and evaluate therapeutic approaches in preclinical and, possibly, clinical settings.

0.2 How contributions are specified

The research questions presented in this thesis have been addressed through the years thanks to a collaborative effort from many people in Pizzorusso's Lab and outside of it. In order to make it easier for the reader to fully appreciate the background and scope of these projects, I included in this thesis some experiments or analysis that have not been performed by me

With the intent to clarify my specific contribution, each part (Part I, Part II, Part III) includes a section after the Introduction titled *"Personal contribution to the project"*. In these sections, I summarize my involvement in each conceptual, experimental or analytical part of the work.

Part I

The gut microbiota of environmentally enriched mice regulates visual cortical plasticity

1 Introduction

This part represents a project that I first-authored and that has been published in Cell Reports (Lupori et al. 2022). The full article is available at this link.

1.1 Summary

Exposing animals to an enriched environment (EE) has dramatic effects on brain structure, function, and plasticity. The poorly known *"EE-derived signals"* mediating the EE effects are thought to be generated within the central nervous system. Here, we shift the focus to the body periphery, revealing that gut microbiota signals are crucial for EE-driven plasticity. Developmental analysis reveals striking differences in intestinal bacteria composition between EE and standard rearing (ST) mice, as well as enhanced levels of short-chain fatty acids (SCFA) in EE mice. Depleting the microbiota of EE mice with antibiotics strongly decreases SCFA and prevents activation of adult ocular dominance plasticity and spine dynamics. SCFA treatment in ST mice mimics EE induction of ocular dominance plasticity. Remarkably, transferring the microbiota of EE mice to ST recipients activates adult ocular dominance plasticity. Thus, experience-dependent changes in gut microbiota regulate brain plasticity.

1.2 Introduction to the project

The complexity of brain circuits is sculpted both by innate genetic programs and environmental stimuli capable of activating brain plasticity and, in turn, reshaping brain circuits and behavior. This process is particularly evident in the development and refinement of neuronal circuits belonging to sensory modalities (Hübener et al. 2014).

Since the 1960s, scientists noticed that raising rodents in an enriched housing condition characterized by elevated social interactions, and cognitive, sensory, and motor stimulations (Kempermann 2019) could improve their learning and memory abilities (Rosenzweig et al. 1996). Interestingly, the benefits of this enriched environment (EE) go beyond memory features and embrace several aspects of brain functionalities, including healthy development, emotional behavior, recovery from neural damage, and positive effects on a variety of preclinical models of neuropsychiatric diseases (Nithianantharajah et al. 2006). Indeed, EE is known to enhance neuronal activation, signaling, and plasticity throughout various brain regions, including sensory areas, and at different ages (L. Baroncelli et al. 2010). For example, ocular dominance plasticity, a change in eye preference of cortical cell responses induced by monocular deprivation (MD), is typically observed during a critical period of postnatal development (Hensch 2005; Levelt et al. 2012). However, EE mice showed strong ocular dominance plasticity (Greifzu et al. 2014) and recovery from amblyopia also during adulthood (Sale et al. 2007; Tognini et al. 2012). Moreover, EE was found to accelerate several molecular and functional aspects of visual cortical development

(Cancedda et al. 2004), indicating that the visual system is highly influenced by EE both during development and adulthood.

A variety of mechanisms have been discovered to contribute to the EE plasticity enhancement, such as increased hippocampal neurogenesis, changes in the excitatory/inhibitory circuit ratio, promotion of structural plasticity of dendritic spines, alteration in BDNF levels, microglia rearrangement, chromatin remodeling, and others (L. Baroncelli et al. 2010; Kempermann 2019; Pizzorusso et al. 2007). So far, all the mechanisms explaining EE influence on neural plasticity have been searched inside the brain. However, the complexity of EE stimuli should bring benefits to the whole body. Thus, we seek to investigate if signals coming from the periphery could participate in EE-driven plasticity in the central nervous system, focusing on the gut microbiota.

The intestinal microbiota has emerged as a complex regulator of system-wide physiology (B. O. Schroeder et al. 2016). Classically, gut microbes have been studied in the context of host metabolic homeostasis and immune system development and function (Nicholson et al. 2012; Rooks et al. 2016; Tremaroli et al. 2012). Nevertheless, the relationship between the intestinal microbiota and its host seems to be deeply intricate, going far beyond the influence on metabolism and immunity (Murakami et al. 2020). Indeed, recent reports have suggested the commensals to play an important role in brain-related processes: myelination (Gacias et al. 2016; Hoban et al. 2016), microglia maturation (Erny et al. 2015), neurogenesis (Möhle et al. 2016), blood-brain-barrier permeability (Braniste et al. 2014), and finally influence on behavioral outcomes (Boehme et al. 2021; Cowan et al. 2020; Forsythe et al. 2016; Hsiao et al. 2013; Tognini 2017) and neural plasticity (Darch et al. 2021; Buffington et al. 2016; Buffington et al. 2021). Despite this evidence, little is known about how intestinal bacteria impinge on neuronal function and, especially, if there is a link between experience-dependent plasticity and the gut microbiota.

In this study, we show that EE significantly alters the intestinal microbiota in C57BL/6J mice, and that microbiota manipulation through antibiotics interferes with EE-driven visual cortical plasticity, dendritic spine dynamics, and microglial rearrangement. Strikingly, the fecal microbiota transplant (FT) from EE donors to adult standard (ST) mice was able to enhance ocular dominance plasticity in the ST recipients. Overall, our study introduces a key concept: environment-dependent changes in the gut microbiota composition can regulate brain plasticity.

1.3 Personal contribution to the project

Here I summarize, for clarity, the details of my specific personal contribution to this project. All of the conceptual, experimental and analytical tasks are grouped according to the level of my involvement in three categories as follows:

- I was the only/main contributor
  - Intrinsic Signal Optical Imaging (IOS) experiments
  - Writing software for IOS analysis
  - Two-photon imaging experiments
  - Writing software for dendritic spine analysis
  - Figures layout and data visualizations

- I collaborated in the tasks
  - Conceptualization of the project
  - 16S Data analysis
  - SCFA quantification and analysis
- Task performed by other people or institutions
  - Feces collection and processing
  - 16S Sequencing

2 Results

2.1 EE modulates the composition of the gut microbiota

C57BL/6J mice were reared from birth in ST (standard laboratory cage, containing only bedding and nesting material), or EE conditions (large cage, containing also running wheels, and differently shaped toys; Figure 2.1a) from birth (EE birth).

In order to investigate the intestinal bacteria composition, fresh feces were collected in a longitudinal way from ST and EE birth mice before weaning: postnatal day (P) 20, a few days after weaning (P25), and during adulthood (P90) (Figure 2.1b). The bacterial DNA was extracted from the feces and analyzed through 16S rRNA sequencing (seq).

To analyze the results, we first calculated alpha-diversity, a parameter reflecting species richness in a microbial ecosystem (Thukral 2017). We observed that there was a significant increase in alpha-diversity in both ST and EE mice between P20 and P90 (Figure 2.1c); however, there were no intergroup differences at any age tested, indicating that housing animals in EE did not alter the alpha-diversity in the microbial ecosystem.

Second, we computed beta-diversity, which measures the degree of phylogenetic similarity between microbial communities, using the unweighted UniFrac algorithm (Lozupone et al. 2005). Principal coordinate analysis (PCoA) of unweighted UniFrac distance showed that the microbiota of ST animals clustered in different groups at P20, P25, and P90 (Figure 2.1d). EE birth mice also displayed an age-dependent difference between P90 and P20 or P25 mice, although P20 and P25 were not significantly different (Figure 2.1e).

Third, we sought to explore differences in the bacterial composition between EE birth and ST conditions by using linear discriminant analysis (LDA) effect size (LEfSe) method (Segata et al. 2011). LEfSe revealed a relatively small, although significant difference in some taxa in P20 ST mice versus P20 EE. In particular, at P20 species in Mollicutes class, Anearoplasmataceae family and Anearoplasmatales order were significantly more abundant in EE with respect to ST. PCoA of the unweighted UniFrac distance matrix confirmed the phylogenetic similarities between ST and EE at P20. At P25, the cladogram displayed a situation similar to P20, in addition taxa in the Erysipelotrichia class, Erysipelotrichales order, and Erysipelotrichaceae family were more abundant in EE than in ST mice. Also, beta-diversity showed clustering in more separate groups.

Intriguingly, at P90 the composition of the microbiota in EE birth mice dramatically diverged from that of age-matched ST rodents, as displayed by the cladogram in Figure 1F. The enrichment in taxa belonging to Tenericutes already present at P20 and P25 was maintained. Furthermore, species present in the family Rikenellaceae, the order Bacteroidales and the class Bacteroidia, all included in the phylum Bacteroidetes, were more abundant in EE. On the other hand, several taxa belonging to the phylum Firmicutes were significantly enriched in ST (Figure 2.2a). As expected, PCoA of beta-diversity calculated through the unweighted UniFrac distance demonstrated that EE and ST microbes clustered in separate groups at P90 (Figure 2.2b), indicating robust differences in the membership of gut bacteria between EE and ST mice.

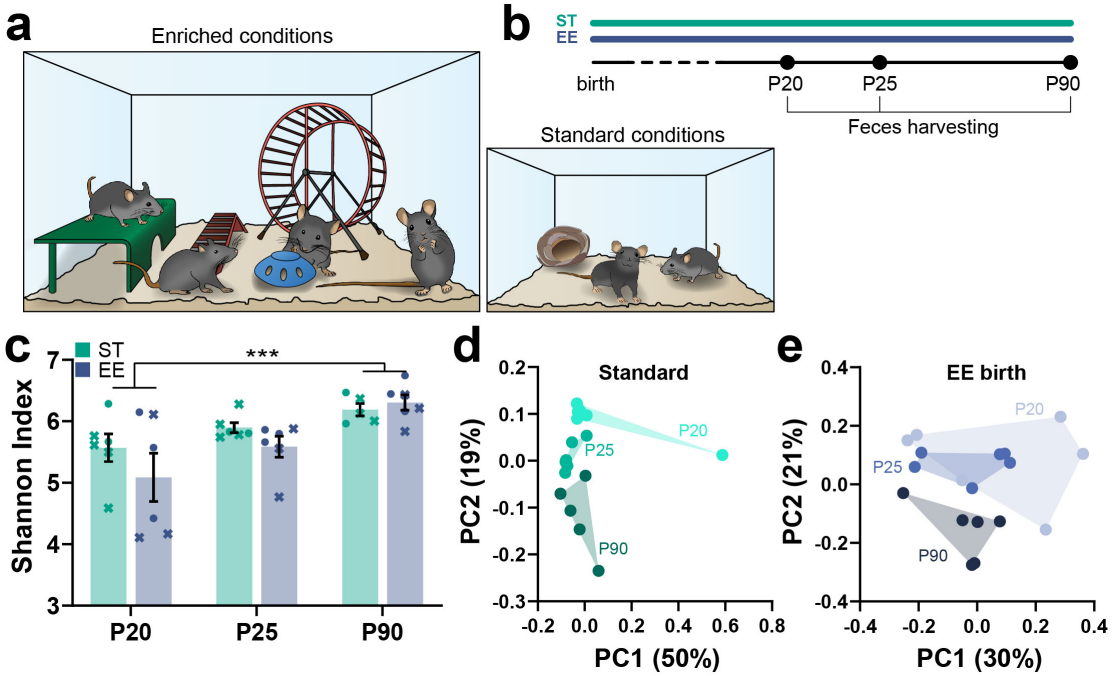

Figure 2.1: **EE modulates the gut microbiota composition**. **(a)** Schematic of enriched and standard housing conditions. **(b)** Experimental timeline. **(c)** Shannon Index for all the conditions, showing alpha-diversity (n=6 EE (three males and three females), n=6 ST (four males, two females), n=5 in P90 ST (three males and two females), two-way ANOVA, age∗housing, age, $F_{2,29} = 8.764$ p=0.0011, post hoc Tukey test P20 versus P90 p<0.001. Crosses represent males and circles represent females). **(d,e)** PCoA showing beta-diversity (unweighted UniFrac distance) at different ages in ST and EE birth animals (ANOSIM test, ST group: P20 versus P25 R=0.32 p=0.002, P25 versus P90 R=0.424 p=0.004, P20 versus P90 R=0.461 p=0.009; EE group: P20 versus P25 R=-0.007 p=0.46, P25 versus P90 R=0.483 p=0.0015, P20 versus P90 R=0.291 p=0.008).

Principal component analysis (PCA) of operational taxonomic units (OTU) abundance comparing ST and EE birth mice at all ages and considering the first component (PC1) indicated that the differences in the microbiota composition were significant only at P90, while higher similarity was present in microbe composition at P20 and P25 (Figure 2.2c).

Thus, our 16S rRNA-seq data demonstrated a progressive developmental divergence of the microbiota composition between mice living in EE and ST conditions. Considering that EE is able to promote different forms of plasticity in a variety of brain areas during adulthood, we further explored the possible link between gut microbiota and EE-driven plasticity in the adult visual cortex.

2.2 Depletion of the gut microbiota in EE mice prevented ocular dominance plasticity

Short periods of MD do not induce ocular dominance plasticity in adult ST mice (Lehmann et al. 2008), whereas they induce strong plasticity in adult EE mice, demonstrating that

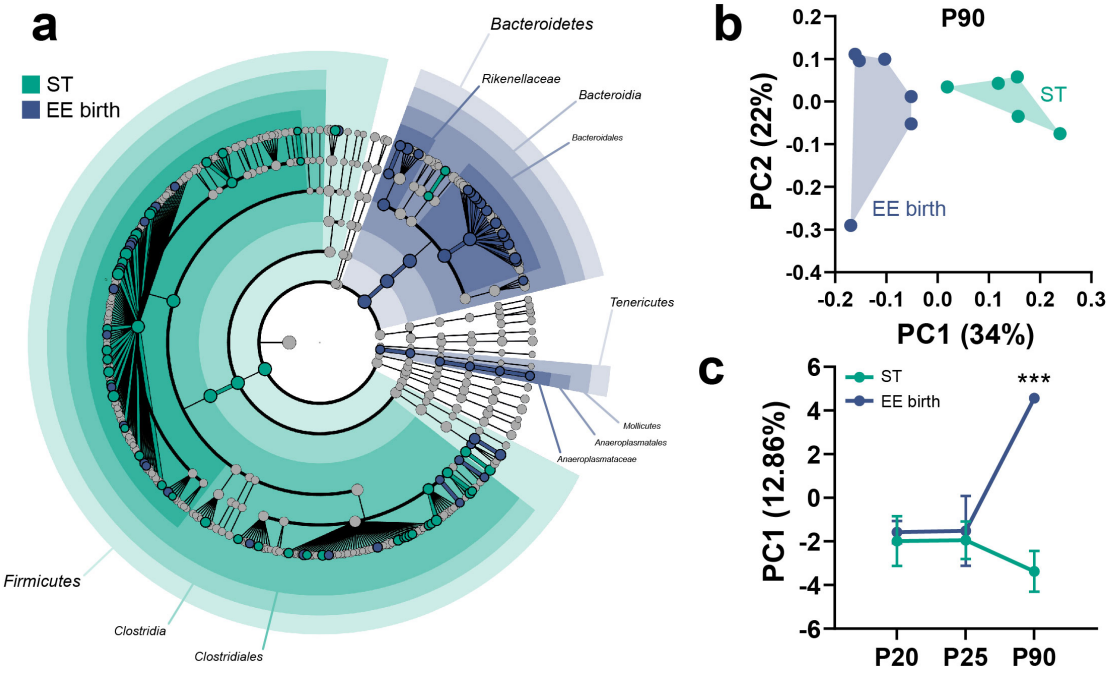

Figure 2.2: **EE modulation of the gut microbiota in adult animals**. **(a)** Cladogram of differential bacterial composition (ST versus EE, P90) using LEfSe analysis. Shaded areas represent taxa significantly enriched in one of the conditions. **(b)** PCoA between ST and EE birth animals at P90 (ANOSIM test, ST versus EE birth, P90: R=0.445 p=0.0015). **(c)** First principal component from an integrated PCA of OTU abundance of all the experimental groups (two-way ANOVA time∗housing, interaction $F_{2,28}$ = 8.482 p=0.0013, post hoc Holm-Sidak ST versus EE birth (P90) t_{28} = 5.18 p<0.001).

EE potently activates visual cortical plasticity (Greifzu et al. 2014; Sale et al. 2007). To investigate the contribution of signals coming from the intestinal microbes on EE-induced visual cortical plasticity, the microbiota of the animals living in EE was depleted using a wide-spectrum antibiotic cocktail (ABX: ampicillin, neomycin, metronidazole, and vancomycin) in drinking water. The ABX treatment started 1 week before birth (ABX in dams' water) and continued until P120 (Figure 2.3a). The efficacy of the treatment was demonstrated by 16S rRNA-seq of fecal bacteria after ABX administration. In order to test ocular dominance plasticity, mice were subjected to optical imaging of the intrinsic optical signal (IOS, Figure 2.3b-d). IOS was performed before and after 3 days of MD (3dMD) in the same subjects (Figure 2.3a). Strikingly, ABX treatment completely prevented ocular dominance plasticity in adult EE mice (Figure 2.3e,f).

As a control, we also confirmed that 3dMD elicited an ocular dominance shift in ST mice during the critical period, but not in adult mice (Figure 2.5a,b). Overall, these data indicate that an intact intestinal microbiota is necessary for the enhancement of adult plasticity observed in EE rodents.

As metronidazole could cross the blood-brain-barrier (Champagne-Jorgensen et al. 2019), an ABX devoid of metronidazole (only ampicillin, vancomycin, and neomycin) was tested in adult EE mice. The new antibiotic cocktail was able to prevent visual cortical plasticity as the ABX (Figure 2.5c). Conversely, the treatment with metronidazole alone

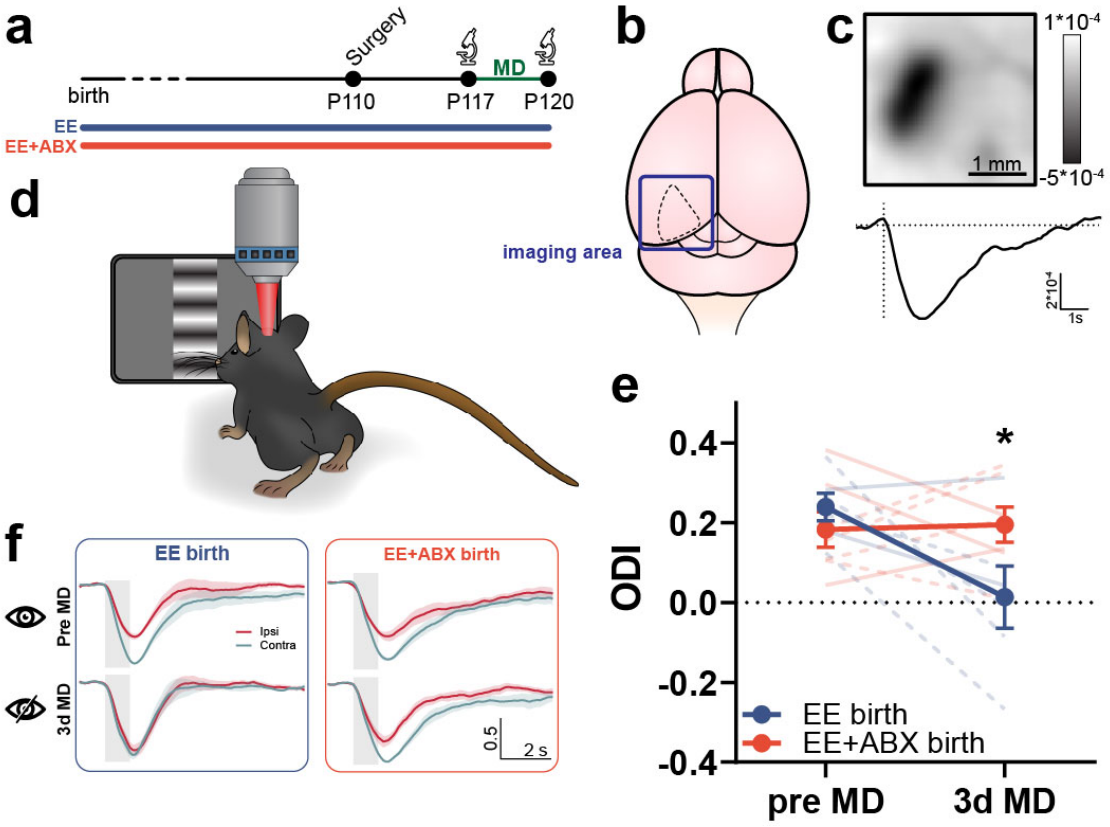

Figure 2.3: **Lifelong ABX treatment prevents the plasticity enhancing effect of EE**. **(a)** Experimental timeline. **(b,d)** Schematic of the imaging setup and imaging area. **(c)** Representative intrinsic signal response (top: response image, bottom: signal timeline) from the binocular primary visual cortex to visual stimulation. Scale bar, 1 mm. **(e)** Ocular Dominance Index (ODI) before and after MD. Thin lines represent single animals (n=6 (two males and four females) EE birth, n=7 (three males and four females) EE + ABX-birth, two-way RM ANOVA time∗housing, interaction $F_{1,11} = 6.716$ p=0.025, post hoc Holm-Sidak, EE birth versus EE + ABX-birth (3dMD) $t_{11} = 3.3$ p=0.013). **(f)** Normalized response timeline to contralateral (contra) and ipsilateral (ipsi) eye stimulation before and after MD for both groups. Shaded area represents visual stimulus duration. In (e), solid lines represent males and dashed lines represent females. Data in (e) and (f) are presented as mean ± SEM.

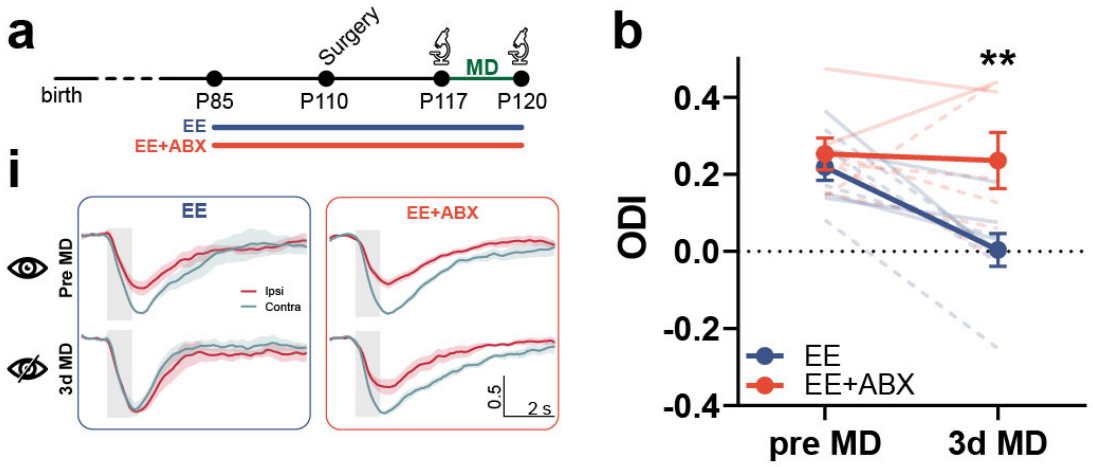

Figure 2.4: **Short-term ABX treatment prevents the plasticity enhancing effect of EE.** **(a)** Experimental timeline. **(b)** ODI before and after MD (n=8 EE (four males, four females), n=7 EE + ABX (two males, five females), two-way RM ANOVA time∗housing, interaction $F_{1,13} = 5.936$ p=0.030, post hoc Holm-Sidak, EE versus EE + ABX (3dMD) $t_{26} = 3.342$ p=0.0051). **(c)** Normalized response timeline to contralateral (contra) and ipsilateral (ipsi) eye stimulation before and after MD for both groups. Shaded area represents visual stimulus duration. In (b), solid lines represent males and dashed lines represent females. Data in (b) and (c) are presented as mean ± SEM.

for 5 weeks simultaneously to EE did not block the EE-driven enhancement of ocular dominance plasticity in adult mice (Figure 2.5c), suggesting that the specific antimicrobial effects of metronidazole are not sufficient to counteract the EE enhancement in plasticity, and ruling out a direct action of metronidazole on cortical neurons.

To rule out any developmental effects of the ABX treatment from birth, we performed the 3dMD experiment in mice reared in EE and treated with ABX for only 5 weeks from P85 until P120 (Figure 2.4). This short EE protocol during adulthood was sufficient to induce ocular dominance plasticity in response to 3dMD (Figure 2.4b and c, EE group). The induction of ocular dominance plasticity by brief EE was also sensitive to microbiota depletion. Indeed, if ABX was administered simultaneously to EE, the EE-driven plasticity was blocked (Figure 2.4b and c, EE + ABX group).

Importantly, before 3dMD, visual responses and baseline ocular dominance of both EE + ABX-birth and EE + ABX mice were not different from their controls (Figure 2.5d,e), thus excluding a possible direct effect of ABX treatment on cortical responses.

In conclusion, an unperturbed intestinal microbiota is necessary for EE promotion of ocular dominance plasticity.

2.3 EE effects on dendritic spines is blocked by ABX administration

Dendritic spines are protrusions harboring the postsynaptic machinery of excitatory synapses. Spines are dynamic compartments, and their structural remodeling is thought to be one of the signatures of the ongoing rewiring of neuronal circuits (A. Holtmaat et al. 2009). Since EE is known to increase the density and dynamics of dendritic spines in the

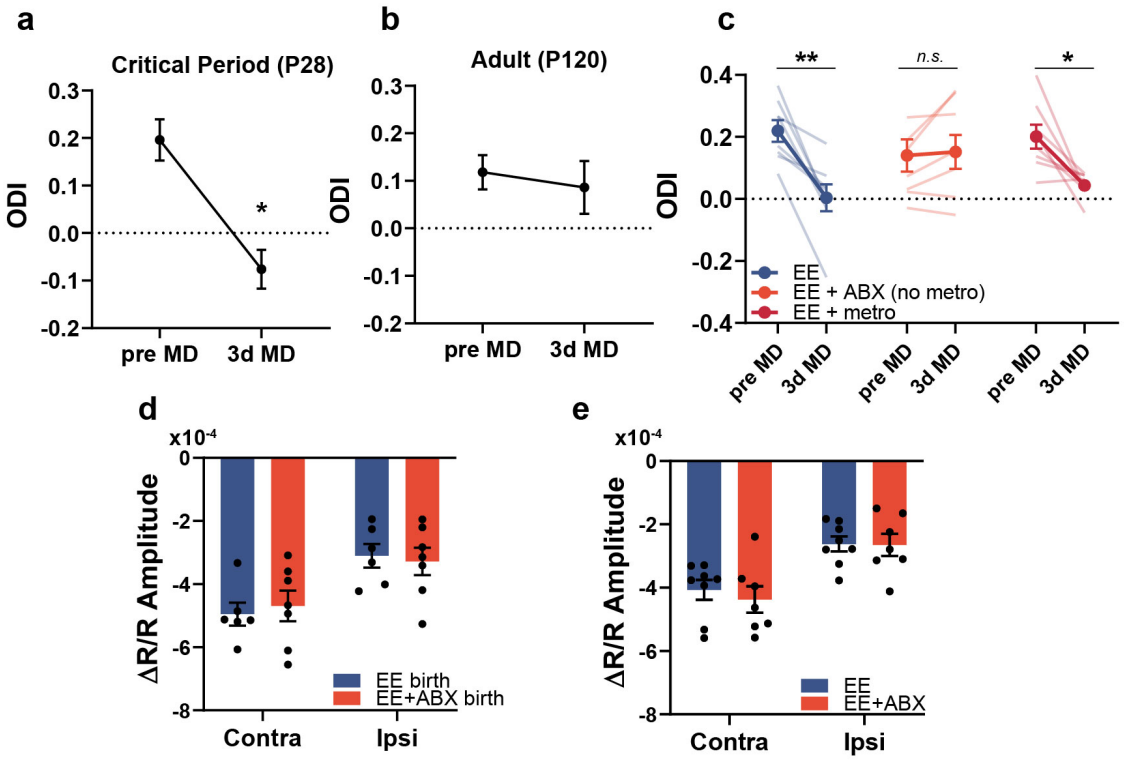

Figure 2.5: **Details of the effects of ABX and its components on OD plasticity. (a)** Ocular Dominance Index (ODI) before and after monocular deprivation in young (P28, critical period) mice (N=4 two-tailed paired t-test $t_3 = 3.25$ p=0.047) **(b)** ODI before and after monocular deprivation in adult (P120) mice (N=5 two-tailed paired t-test $t_4 = 0.36$ p=0.74). **(c)** ODI before and after MD in: adult mice in EE (EE; N=8, 4 males 4 females, same data as in Figure 2.2b for comparison) adult mice in EE treated with an antibiotic cocktail lacking metronidazole (N=8, 4 males, 4 females EE+ABX(no metro)), and adult mice in EE treated with metronidazole (N=8, 3 males 5 females EE+metro) two-way RM ANOVA treatment∗MD, interaction $F_{2,21} = 5.341$ p=0.0133. Post-hoc Holm-Sidak: EE preMD vs EE 3dMD $t_{21} = 4.223$ p=0.0011; EE+ABX(no metro) preMD vs EE+ABX(no metro) 3dMD $t_{21} = 0.2299$ p=0.820; EE+metro preMD vs EE+metro 3dMD $t_{21} = 3.070$ p=0.012. **(d)** Intrinsic signal response amplitude to contralateral and ipsilateral eye stimulation in EE birth and EE+ABXbirth animals before MD (N=6, 2 males 4 females EE-birth; N=7, 3 males 4 females EE+ABX-birth) two-way RM ANOVA eye∗housing, interaction $F_{1,11} = 1.322$ p=0.27, eye $F_{1,11} = 70.96$ p¡0.0001, housing $F_{1,11} = 0.005$ p=0.95. **(e)** Intrinsic signal response amplitude to contralateral and ipsilateral eye stimulation in EE and EE+ABX animals before MD (N=8, 4 males 4 females EE; N=7, 2 males 5 females EE+ABX); two-way RM ANOVA eye∗housing, interaction $F_{1,13} = 0.609$ p=0.449, eye $F_{1,13} = 80.60$ p¡0.0001, housing $F_{1,13} = 0.146$ p=0.71. Data are presented as mean ± SEM.

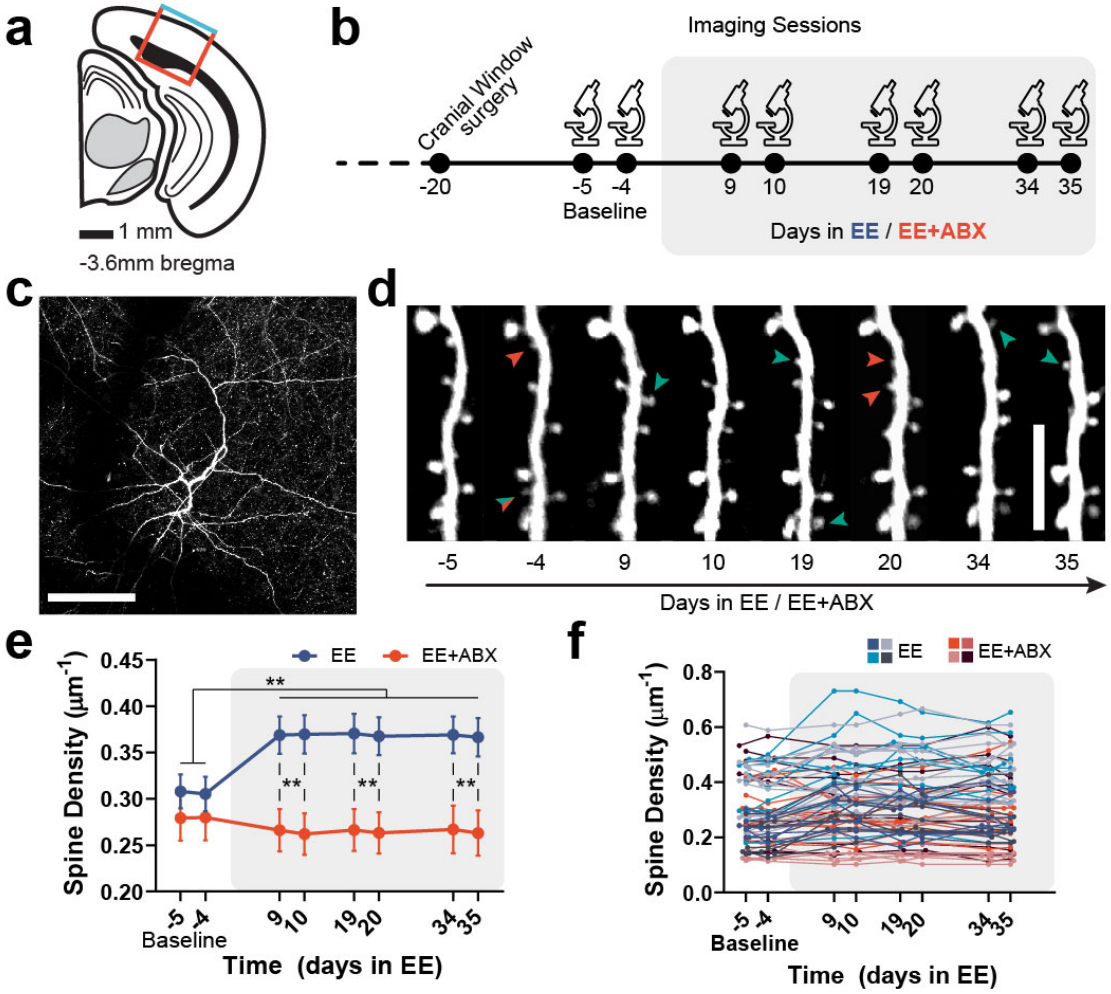

Figure 2.6: **ABX treatment modulates the effect of EE on dendritic spine density.**. **(a)** Schematic coronal section of the primary visual cortex showing the imaging site. **(b)** Experimental timeline. **(c)** Representative low magnification image of a neuron. Scale bar, 100µm. **(d)** Representative high-magnification images of a dendritic segment at eight consecutive time points. Green arrowheads: spine formation, red arrowheads: spine elimination. Scale bar, 10µm. **(e,f)** Spine density over time. Averages per dendrites (e) and single dendrites (e), color coded for the animals to which they belong (n=39 EE, n=28 EE + ABX, two-way RM ANOVA time∗treatment, interaction $F_{7,455} = 20.97$ p<0.0001, post hoc Holm-Sidak, EE versus EE + ABX (9d-35d) t_{54-61}>3.15 p<0.01 for all comparisons; EE(9d-35d) versus EE(baseline) t_{38}>5.73 p<0.0001 for all comparisons.

cortex (Xu et al. 2016), we asked whether manipulating the gut microbiota could interfere with EE-driven plasticity through mechanisms involving spines remodeling. We performed repeated two-photon in vivo imaging to analyze dendritic spines in a cohort of transgenic Thy1-GFP-M mice expressing GFP in a sparse population of layer V pyramidal neurons in the visual cortex (Feng et al. 2000; Jung et al. 2014). We acquired images of the same apical dendritic segments for 40 days in the visual cortex Figure 2.6. After two baseline imaging time points (1-day interval), animals were put in EE cages for 35 days (5 weeks) and received ABX in drinking water (EE + ABX group) or regular water (EE group) (Figure 2.6b). The same dendritic segments were imaged in the two groups 9, 10, 19, 20, 34, and 35 days after the beginning of EE (Figure 2.6b-d).

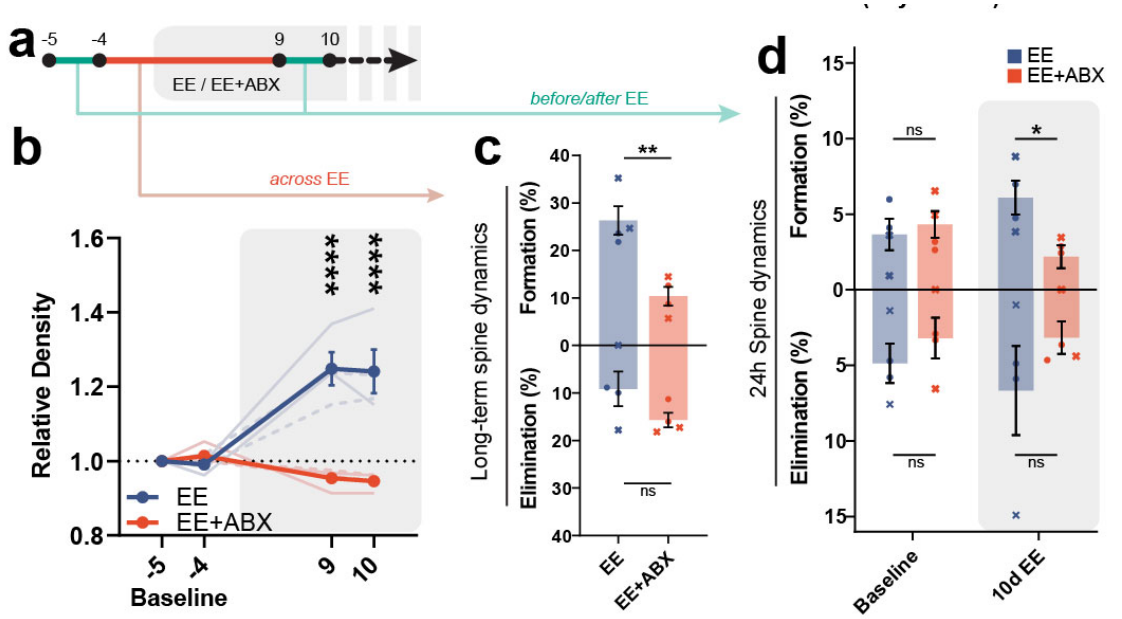

Figure 2.7: **Dendritic spine dynamics on ABX-treated mice in EE. (a)** Schematic of the analysis for spine dynamics in (c) and (d). **(b)** Spine density relative to the first imaging time point. Thin lines represent single animals (n=4 EE (two males, two females), n=4 EE + Abx (two males, two females), two-way RM ANOVA time∗treatment, interaction $F_{3,18} = 28.60$ p<0.0001, post hoc Holm-Sidak, EE versus EE + Abx (9d-10d) t_{24}>7.52 p<0.0001 for al comparisons; EE(9d-10d) versus EE(-4) t_{18}>7.56 p<0.0001 for all comparisons). **(c)** Long-term (10d) spine dynamics across the beginning of EE (n=4 EE (two males, two females), n=4 EE + ABX (two males, two females), Formation: unpaired two-tailed t test $t_6 = 4.42$ p=0.0045; Elimination: unpaired 2-tailed t test $t_6 = 1.65$ p = 0.15) **(d)** Short-term 24-h spine dynamics before and after EE. (n=4 EE (two males, two females), n=4 EE + ABX (two males, two females). Formation: two-way RM ANOVA time∗treatment, interaction $F_{1,6} = 6.620$ p=0.042, post hoc Holm-Sidak EE versus EE + ABX (10dEE) $t_{12} = 2.87$ p = 0.028; Elimination: two-way RM ANOVA time∗treatment, no significant differences). In (c) and (d), crosses represent males and circles represent females; in (b), solid lines represent males and dashed lines represent females.

The analysis of spine density revealed a significant interaction between time and housing conditions. Post hoc tests showed that spine density in EE mice was significantly larger than in EE + ABX mice at all times after EE start, but it did not differ at baseline.

Comparing spine density within each group at different time points confirmed that spine density did not change over time in the EE + ABX group. By contrast, the EE group displayed a dramatic increase in spine density occurring between the baseline and the first imaging time point after the beginning of EE (10 days after EE start, Figure 2.6e,f).

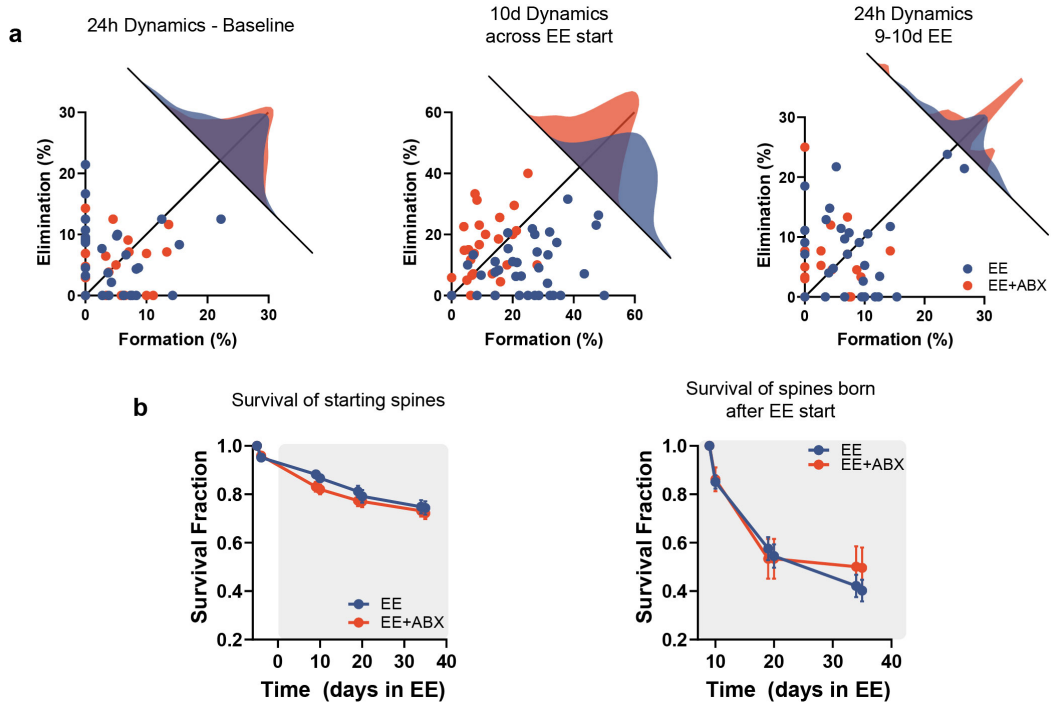

Figure 2.8: **Dendritic spines dynamics and survival. (a)** Each dendrite spine elimination plotted as a function of spine formation for the time points analyzed in Figure 2.7c-d. **(b)** Left: spine survival curve of the spines present at the first time point (N=39 EE, N=28 EE+ABX; two-way RM ANOVA time*treatment, interaction: $F_{7,455} = 1.54$ p=0.15, time: $F_{1.739,113.0}$=133.5 p¡0.001, treatment: $F_{1,65} = 0.86$ p=0.36). Right: spine survival curve of the spines born between -4d and 9d timepoint (N=39 EE, N=26 EE+ABX; two-way RM ANOVA time*treatment, interaction: $F_{5,310} = 1.27$ p=0.28 time: $F_{1.989,123.3} = 93.57$ p¡0.001, treatment: $F_{1,62} = 0.12$ p=0.73).

This observation was confirmed by analyzing the data from single animals. Indeed, animals in the EE group showed a significant 25% increase in spine density after 10 days of EE with respect to baseline levels, while this effect was prevented in animals treated with ABX (Figure 2.7b). To further dissect this effect, we calculated spine formation and elimination rates during this critical time window (Figure 2.7a, Figure 2.8a). Across the first 10 days of EE, spine elimination rates were not different between the two groups; however, animals treated with ABX had a remarkably lower spine formation rate compared with controls, thus explaining the lack of increase in spine density in the ABX-treated group (Figure 2.7c). Moreover, the EE + ABX group had a significantly lower spine formation rate with respect to EE controls, also analyzing the short-term 24-h spine dynamics. Indeed, short-term formation rate was comparable between the two groups at baseline, but significantly differed after 10 days of EE. Conversely, elimination rates were similar between the two groups (Figure 2.7d).

These data suggest that the ABX treatment prevents the increase in spine density typical of enriched animals by interfering with the process of formation of new spines and not by destabilizing existing spines or increasing the opposing process of spine elimination. This interpretation is further corroborated by the analysis of dendritic spine survival curves. Indeed, both for the subset of spines originally present at the first time point and for the subset of newborn spines that appeared after the start of EE, the treatment with ABX did not have any effect on survival curves (Figure 2.8b).

2.4 Short-chain fatty acid administration enhances ocular dominance plasticity in adult mice

To dissect the possible mechanisms through which the gut microbiota of EE mice could promote cortical plasticity in adulthood, we focused on commensal-derived metabolites.

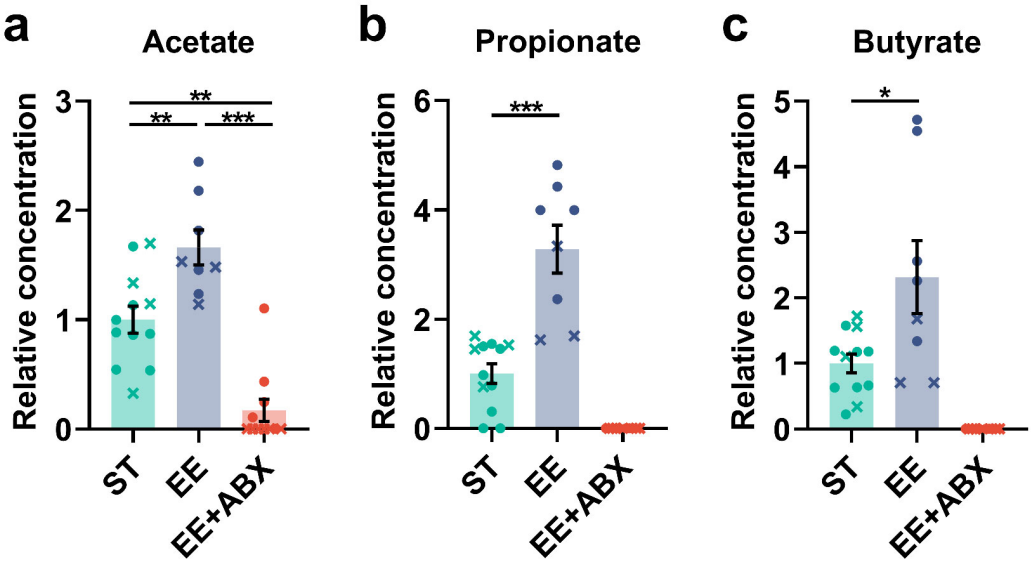

Figure 2.9: **EE increases fecal SCFAs content. (a-c)** Gas chromatography analysis (GC-FID) of SCFAs components from feces samples collected from standard reared mice (ST, N=12 4 males 8 females), mice reared in Environmental Enrichment (EE, N=8 3 males, 5 females) and mice raised in EE and treated with an antibiotics cocktail (EE+ABX, N=10, 5 males, 5 females) for five weeks. Concentrations are relative to the mean of the ST group. **(a)** Acetate concentration in the different groups (one-way ANOVA p=0.001, $F_{2,28} = 32.00$, post-hoc Holm-Sidak, ST vs EE $t_{28} = 3.56$, p=0.0013; ST vs EE+ABX $t_{28} = 4.89$, p<0.001; EE vs EE+ABX $t_{28} = 7.89$, p<0.001). **(b)** Propionate concentration in the different groups (unpaired two-tailed t-test ST vs EE $t_{18} = 5.45$, p<0.001; EE+ABX not included in the statistical analysis because it was under the instrument detection limit). **(c)** Butyrate concentration in the different groups (unpaired two-tailed t-test ST vs EE $t_{18} = 2.73$, p=0.014; EE+ABX not included in the statistical analysis because it was under the instrument detection limit).

Short-chain fatty acids (SCFAs), the main metabolites produced in the colon by bacterial

fermentation of dietary fibers and resistant starch, have been shown to play a key role in neuro-immuno-endocrine regulation, and in several aspects of the gut-microbiota-brain axis (Dalile et al. 2019). Gas chromatography coupled with flame ionization detector (GC-FID) analysis of fecal-derived SCFA showed a significant increase in EE with respect to ST mice in acetate, propionate, and butyrate concentration, whereas ABX administration completely blocked this effect (Figure 2.9).

Based on these results, we explored the possibility that SCFA could be microbiota-derived metabolites mediating the pro-plasticity effect of EE. An SCFA mix, containing butyrate, propionate, and acetate, was dissolved in the drinking water and administered to ST adult mice for 4 weeks.

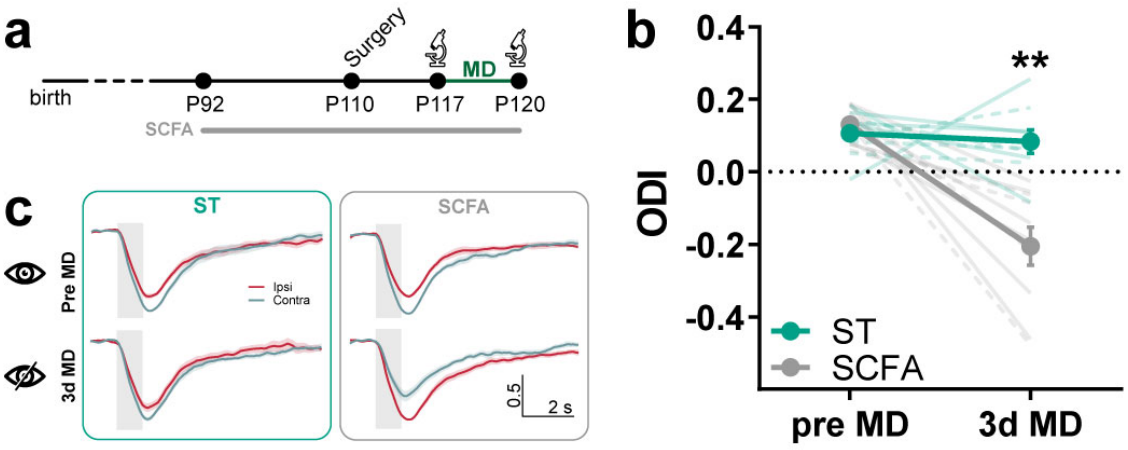

Figure 2.10: **SCFA administration mimics the effect of EE on plasticity. (a)** Experimental timeline. **(b)** ODI before and after MD. Thin lines represent single animals (n=9 ST (five males, four females), n=10 SCFA (six males, four females), two-way RM ANOVA time*treatment, interaction $F_{1,17} = 15.28$ p=0.0011, post hoc Holm-Sidak, ST versus SCFA (3dMD) $t_{34} = 5.94$ p<0.001). Solid lines represent males and dashed lines represent females. **(b)** Normalized response timeline to contralateral (contra) and ipsilateral (ipsi) eye stimulation before and after MD for both groups. Shaded area represents visual stimulus duration.

During the last week of treatment, mice were subjected to IOS imaging before and after 3dMD (Figure 2.10a). Strikingly, SCFA in drinking water was able to promote visual cortical plasticity in adult ST mice, while, as expected, control age-matched ST animals drinking regular water did not show the ocular dominance shift (Figure 2.10b,c).

Our results suggest that SCFAs could be candidate molecules through which the microbiota influence cortical plasticity.

2.5 Fecal transplantation transfers the plastic phenotype from EE to ST adult mice

To provide further independent evidence to support the role of intestinal microbes in ocular dominance plasticity of EE mice, adult ST mice were subjected to an FT experiment.

Fresh feces from EE mice or ST animals as a control were collected and a PBS suspension was freshly prepared. The FT was performed in conventionally raised ST recipient mice,

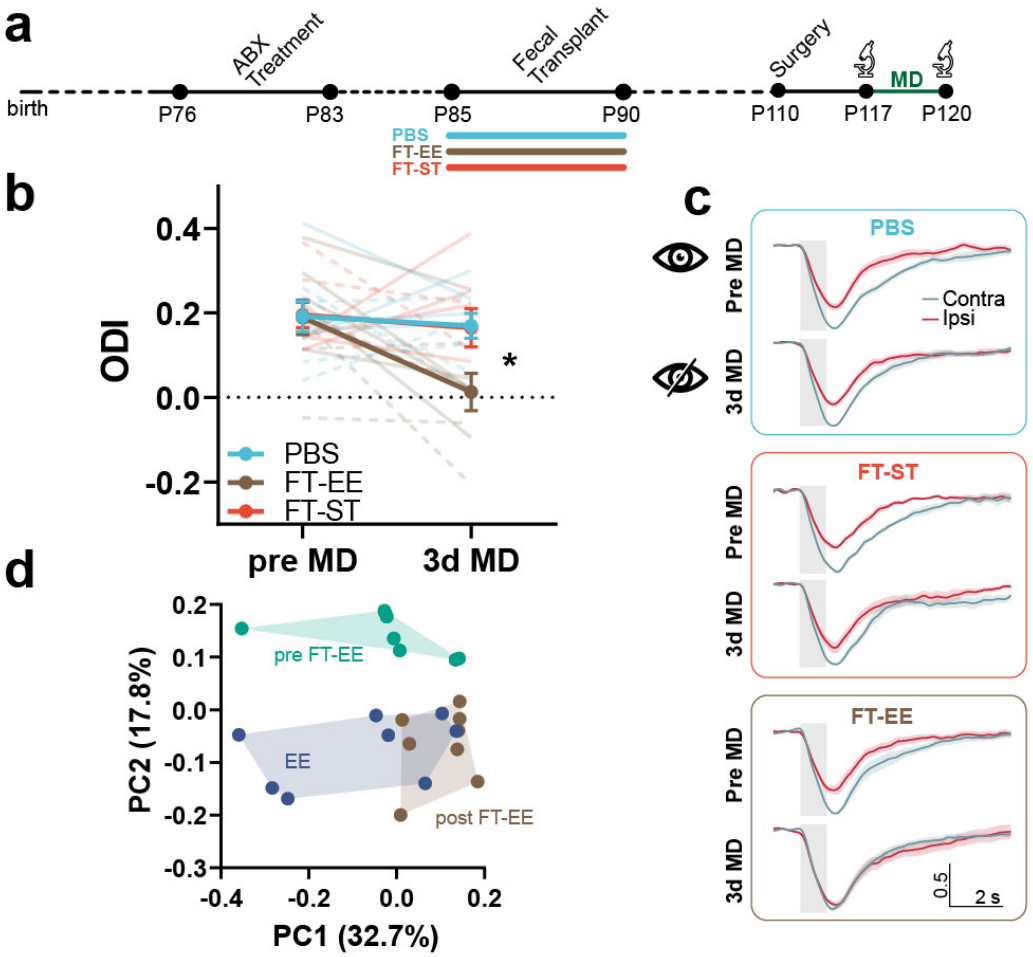

Figure 2.11: **Fecal transplant ODI (a)** Experimental timeline. **(b)** ODI before and after MD. Thin lines represent single animals (n=9 PBS (four males, five females), n=9 FT-EE (five males, four females), n=8 FT-ST (five males, three females), two-way RM ANOVA time*treatment, interaction $F_{2,23} = 2.888$ p=0.076, post hoc Holm-Sidak, PBS versus FT-EE (3dMD) $t_{46} = 2.92$ p=0.029); PBS versus FT-ST (3dMD) $t_{46} = 0.094$ p>0.99; FT-EE versus FT-ST (3dMD) $t_{46} = 2.773$ p=0.039. **(c)** Normalized response timeline to contralateral (contra) and ipsilateral (ipsi) eye stimulation before and after MD for all groups. Shaded gray area represents visual stimulus duration. **(d)** PCoA (unweighted UniFrac distance) of EE, preFT-EE and postFT-EE animals (n=8 per group, ANOSIM test, preFT-EE versus EE, R=0.32, p=0.003; preFT-EE versus postFT-EE, R=0.40, p=0.001; EE versus postFT-EE R=0.17, p=0.03). In (b), solid lines represent males and dashed lines represent females. Data in (b) and (b) are presented as mean ± SEM.

previously treated with ABX to favor the engraftment of the new species (Figure 2.11a). FT mice were subjected to oral gavage with the donor feces suspension for 5 days. To exclude a direct effect of the ABX pretreatment on plasticity, a further control group of mice was administered with PBS (the vehicle of the donor feces suspension). After 4 weeks, ocular dominance plasticity was investigated through IOS imaging (Figure 2.11a). Remarkably, transferring feces from EE donors to ST recipients was able to induce visual cortical plasticity in ST mice, while, as expected, control animals inoculated with feces from ST donor mice or the PBS vehicle did not display any ocular dominance shift after 3dMD (Figure 2.11b,c).

Importantly, PCoA of unweighted UniFrac distance showed that the microbiota of ST recipients after the FT with EE feces (postFT-EE) was overlapping the microbiota of EE donor mice, while the microbiota of ST animals before FT (preFT-EE) clustered in a separate group with respect to EE donors and postft (Figure 2.11d). Although still significantly different, the analysis of similarities (ANOSIM) R was only 0.17 in the EE donors versus postFT-EE comparison, indicating the presence of a substantial overlap in the phylogenetic composition of ST recipient and EE donor microbiota (Figure 2.11d).

Altogether, those data demonstrate the efficacy of our FT protocol, and indicate that the "plastic phenotype" of the adult EE mouse can be transferred to an ST animal through the fecal microbiota.

3 Discussion

Since the pioneering studies of Rosenzweig and his collaborators, EE has been widely used as a model for studies on experience-dependent regulation of brain function. Those studies demonstrated that EE dramatically affects brain morphology, chemistry, and physiology; eliciting remarkable plastic responses ranging from molecular to anatomic and functional changes (Rosenzweig et al. 1996). Several investigations continued this line of research trying to understand the specific mechanisms through which EE affects brain plasticity to realize the EE translational potential. However, the mechanisms to explain the EE impact on brain circuits and behavior have been classically explored into the brain itself: among many others, studies identified changes in neurotrophin levels (Pham et al. 2002), altered expression of plasticity-related genes (Rampon et al. 2000) and synaptic proteins (Nithianantharajah et al. 2004; Song et al. 2018), inhibitory circuits remodeling, perineuronal net modifications (Sale et al. 2007; Slaker et al. 2016), and epigenetic mark changes (Fischer et al. 2007; B.-S. Wang et al. 2013). Our study shifts the focus from the central nervous system to the periphery, revealing that signals coming from the gut microbiota contribute to EE-driven cortical plasticity.

3.1 The gut microbiota is modulated by EE

Our study identifies two powerful regulators of the mouse gut microbiota: age and environment. Indeed, we found that fecal bacterial diversity (microbiota alpha-diversity) increases between P20 and P90 in both EE and ST mice. This increase in the complexity of the ecosystem was a general feature process of gut microbiota maturation, not linked to the rearing environment. Significant differences in the phylogenetic composition (beta-diversity) of the bacteria community at distinct ages were observed in ST and EE animals.

Notably, EE dramatically altered the fecal microbiota composition. Importantly, this regulation is specific to EE and it is independent from the dietary regimen or other rearing conditions since the ST and EE cages were housed one next to the other and mice received the same food. The number of species differing between ST and EE mice was relatively small, but still significant, before and a few days after weaning. In particular, the LEfSe analysis at P20 revealed that species in the Mollicutes class, Anearoplasmataceae family, and Anearoplasmatales order were significantly more abundant in EE with respect to ST. At P25, species belonging to the same taxa were still significantly high in EE with respect to ST, in addition to species in the Erysipelotrichia class. However, the most striking difference was present in adulthood, when species belonging to the phyla Tenericutes and Bacteroidetes were significantly enriched in EE. Why the effect of EE was so prominent in adulthood, while at juvenile ages the species distinction was lower, has not been explored yet.

We could speculate that this developmental regulation of EE effect on microbiota might be caused by the fact that adult animals could fully experience the complexity of the stimulation offered by EE. The gut microbiota could be particularly sensitive to

features of the EE including physical activity, exploring new toys, spatial patterns of objects, which are activities preferred by older than little mice. However, we cannot exclude other microbiota remodelers starting to impinge on its composition during early postnatal development. For instance, differences in maternal care from enriched dams might account for the distinct composition observed before weaning. Also, the immune system of EE mice could be influenced to send specific signals to the intestinal microbes by still unknown stimuli, thus shaping the ecosystem toward a precise composition. Finally, as metabolism and the microbiota are deeply intertwined, metabolic cues might also play a role. For instance, physical exercise is an important EE component capable of modulating brain plasticity (Praag et al. 2000); however, it cannot explain the full ocular dominance plasticity enhancement observed in EE rodents (Laura Baroncelli et al. 2012).

Some studies demonstrated changes in the microbiota composition and diversity of rodents after physical exercise, and an increase in the Bacteroidetes phylum and the Lachnospiraceae family (Evans et al. 2014; Mika et al. 2015), and recently EE has been shown to modulate the gut microbiota composition in adult rats (Higarza et al. 2021). Changes in bacteria families after diet or physical exercise were also correlated to behavioral alterations. For instance, increases in taxa belonging to the Lachnospiraceae family were associated with reduced anxiety in exercised mice (Kang et al. 2014). Thus, enhancement in exercise might, indeed, contribute to the experience-dependent modifications observed in our microbiota data; however, other still unidentified cues coming from EE could work as commensal remodelers.

Since the gut-brain axis is a bidirectional communication system, we cannot exclude that messages coming from the enriched brain may also shape the intestinal microbes in order to shift their metabolic potential toward specific biochemical pathways to sustain more dynamic and plastic neural circuitries.

3.2 Cellular underpinnings of gut microbiota action on ocular dominance plasticity

Strikingly, the depletion of the microbiota in EE mice completely blocked visual cortical plasticity. This effect was present both when animals were raised in EE from birth or only with a 5-week EE experience during adulthood. These experiments suggest that an intact microbiota contributes to the EE-dependent enhancement in cortical plasticity.

The microbiota depletion was performed using a classic approach consisting of the administration of a wide-spectrum antibiotic mix used in several gut-microbiota-brain axis studies (Chu et al. 2019; Desbonnet et al. 2015; Gacias et al. 2016; Olson et al. 2018). Furthermore, to exclude off-target effects of the antibiotic metronidazole on neural cells, we performed the same experimental protocol housing adult mice in EE for 5 weeks and administering metronidazole only. Metronidazole alone was not able to prevent the EE-driven enhancement in visual cortical plasticity. Instead, an ABX devoid of metronidazole blocked ocular dominance plasticity in EE mice, thus ruling out the possibility that plastic phenomena could be induced by a direct influence of metronidazole on the brain, and indicating that synergistic alterations of the gut microbiota, rather than individual antimicrobial agents, are necessary to impinge on brain plasticity.

Importantly, microbiome depletion induced by 5-week ABX administration also affected two important EE-induced cellular mechanisms that have been previously involved in

plasticity. Indeed, ABX-treated animals did not show increased dendritic spine dynamics typical of EE mice (Xu et al. 2016).

Notably, microglia has been suggested to phagocytose pre- and postsynaptic elements participating in synapse remodeling during development and plasticity (Cheadle et al. 2020; Hong et al. 2016; Paolicelli et al. 2011; Schafer et al. 2012; Schecter et al. 2017). Here, we observed that ABX-depletion of a functional microbiota not only impacted microglia morphology, but also dendritic spine dynamics in the visual cortex of adult EE rodents. Recent studies demonstrated that EE is able to increase dendritic spine dynamics in the cerebral cortex (Jung et al. 2014). Furthermore, spine remodeling has been shown to be a structural feature of plasticity in the visual system (Bochner et al. 2014; Chakravarthy et al. 2006; El-Boustani et al. 2018; Hofer et al. 2009; Mataga et al. 2004; Oray et al. 2004; Sajo et al. 2016; Sun et al. 2019; Vidal et al. 2016; Villa et al. 2016) and other sensory modalities (A. Holtmaat et al. 2009), suggesting that experience actively sculpts the synaptic landscape to modulate neural circuit function. Our data demonstrated that EE significantly enhanced spine density, through an increase in the growth of new spines.

Remarkably, ABX administration counteracted EE-dependent structural plasticity in the visual cortex, as ABX inhibited the increase in spine density, while spine removal was virtually unaltered. Interfering with the microbiota in EE was essentially translated into hampering the biological processes underlying new spine formation. Our results are in line with previous work suggesting that the gut microbiota can modulate structural properties of the brain. In fact, germ-free mice show dendritic morphology and spine density alterations in various areas of the brain with positive or negative effects, depending on the brain area investigated (Luczynski et al. 2016; Luczynski et al. 2017). Importantly, our data were collected in adult animals in which the microbiota was depleted only in adulthood at the same time as EE, thus suggesting that paradigms that interfere with spine dynamics like EE, still rely on a healthy microbiome in adult age.

3.3 Searching a causal link between microbiota and cortical plasticity

The gut microbiota could communicate with the brain influencing neural function through a variety of communication routes. Among them, our commensals contribute and complement host metabolism by modulating metabolic reactions and producing specific substrates such as SCFA. SCFAs act locally in the intestine and also participate in the maintenance of the host metabolic homeostasis by enhancing nutrient absorptions, and curbing the glycemic response (Alexander et al. 2019). Intriguingly, SCFAs can be released in the systemic circulation, cross the blood-brain-barrier, and reach the brain, where they have been demonstrated to be fundamental for blood-brain-barrier integrity (Braniste et al. 2014), microglia maturation, and homeostasis (Erny et al. 2015). Sodium butyrate decreases microglial activation, pro-inflammatory cytokine secretion (Patnala et al. 2017; Yamawaki et al. 2018), and promotes visual cortical plasticity (Silingardi et al. 2010). Also, acetate was recently shown to modulate microglial phagocytosis and disease progression during neurodegeneration (Erny et al. 2015).

Interestingly, we found that living in EE increases the production of SCFAs. Furthermore, treating ST adult mice with oral SCFAs for 4 weeks mimicked the effects of fecal

transplantation and EE, promoting ocular dominance plasticity. As SCFAs are highly versatile molecules, it is extremely difficult to envision a molecular mechanism for their effects on neural circuits, and the complexity and crosstalk among SCFA pathways acting on the brain further complicate the picture. SCFAs might affect microglia surveillance activity, and neural tissue epigenetic landscape, and thus gene expression, neurotransmitter levels, or SCFAs might act through indirect modulation of endocrine and immune pathways (Dalile et al. 2019).

Here, we observed that SCFA treatment was associated with changes in microglia morphology in the visual cortex, rendering it hyper-ramified with respect to ST control. This shape has been observed in conditions of high plasticity, such as EE, and could favor ocular dominance plasticity through still unknown signals. Therefore, we are tempted to speculate that the microbiota could activate cortical plasticity mechanisms through SCFA-driven microglia remodeling. Future studies using metagenomic and metabolomic techniques will further dissect the bacteria-derived molecules involved, hopefully helping in the identification of specific mechanisms that could be targeted by new microbiota-based strategies for neurological diseases.

Transferring a specific phenotype by transplantation of the intestinal microbes is an important proof to causally link the microbiota to physiology and behavior. Strikingly, the transplantation of the fecal microbiota of EE mice to adult ST animals clearly induced ocular dominance plasticity. This is a key indication that the intestinal microbiota is involved in sensory system plasticity, a developmentally regulated process of plasticity. This observation suggests that EE-derived microbiota might be a powerful tool to trigger juvenile forms of plasticity, facilitating the recovery from amblyopia or other serious conditions such as traumatic brain injury, stroke, and posttraumatic stress disorder, leading to alternative therapeutic strategies for neurodegenerative and neurodevelopmental diseases, or possibly enhancing cognitive performance in healthy subjects. Also, our data prove that signals coming from the intestine overran the stability of the adult sensory circuits and the plasticity brakes.

In summary, these findings introduce a paramount concept: experience-dependent changes in the gut microbiota composition can modulate brain circuit function and plasticity. We propose the idea of an "experience-gut microbiota-brain" link: experience does not only impact the brain directly, but also through a pathway involving signals coming from the body periphery.

3.4 Limitations of the study

Although our study broadly assessed bacterial populations present in the different experimental condition mice using 16S rRNA-seq, this technique provides limited functional information about the microbiome. Future studies will explore this facet of the gut microbiota of EE mice utilizing shotgun metagenomic sequencing.

Another possible limitation of our study is related to sex-specific effects. In our work, both male and female mice were used, and we included sex as a variable in our statistical analyses; however, this reduced the number of analyzed mice. Thus, it could be that sex differences with relatively low effect size could be present. Thus, a deeper investigation with appropriate cohorts of male and female animals might unveil some distinct plasticity effects driven by the microbiota based on sex.

4 Methods

4.1 Animals

All experiments were carried out in accordance with the European Directives (2010/63/EU), and were approved by the Italian Ministry of Health (authorization number 140/2018-PR, 423/2021-PR).

Postnatal day (P)120 male and female C57BL/6J mice were used in this study, unless otherwise stated. ST mice were housed in conventional cages (365 x 207 x 140 mm, 2-3 animals per cage) with nesting material. Enriched mice were housed in larger cages (480 x 375 x 210 mm), in larger groups (5-6 mice per cage). Enriched cages were equipped with a variety of sterile toys of different shapes: running wheels, tunnels, tubes, climbing devices, triangle and igloos-shape shelter, food dispensers in different locations and nesting materials. The toys were substituted with new toys with different shapes and locations with respect to the previous week once a week, to ensure the novelty and continuous stimulation of the environment. The ST and EE cages used in all the experiments were individually ventilated cages to safely maintain the microbiota composition. Mice were housed in the same room, kept under a 12 hour dark: 12 hour light cycle, controlled temperature; and the same regimen of food (standard diet) and water administration ad libitum, was maintained for ST and EE.

4.2 Antibiotic cocktail and short chain fatty acids administration

A group of mice were raised in EE from birth. The dams of EE-pups were transferred from ST cages to EE cages 6-7 days before delivery. The large spectrum antibiotic cocktail (ABX, vancomycin 0.5 g/L, metronidazole 1 g/L, ampicillin 1 g/L and neomycin 1 g/L) was added to the dam's water when they were transferred in the EE cages. The litters continued to drink ABX after weaning (postnatal day (P) 21) until the day of ocular dominance plasticity assessment.

A second group of mice lived in EE only for 5 weeks during adulthood, from P85 to P120, and was exposed to the ABX in drinking water only during those 5 weeks. Other groups of mice living in EE for 5 weeks during adulthood also received an ABX without metronidazole ("ABX-metronidazole" vancomycin 0.5 g/L, ampicillin 1 g/L and neomycin 1 g/L), or only metronidazole (1 g/L) in the drinking water.

To study dendritic spine dynamics, Thy-1 GFP transgenic mice (line M (Feng et al. 2000)) were housed in EE cages from P90 for 5 weeks. The control group had ad libitum access to water, while the treated group had ad libitum access to the ABX in drinking water for 5 weeks. For all the experiments, the ABX was freshly prepared and changed every 2 days.

For the short chain fatty acids (SCFAs) treatment a mix of 25 mM sodium propionate, 40 mM sodium butyrate and 67.5 mM sodium acetate (Sigma-Aldrich) was added to

drinking water as previously described (Erny et al. 2015) for 4 weeks from P90. The solution was freshly prepared and changed every 2 days. Regular water was administered to control mice.

To avoid cage-effects on our experiments, the animals used in all the experimental groups came from different EE or ST cages.

4.3 Faecal DNA extraction and 16S rRNA sequencing

To analyze the composition of the microbiota of ST and EE mice at different ages, fresh faeces were collected longitudinally in the same subject at P20, P25 and P90, snap-frozen in liquid nitrogen and stored at -80°C.

To avoid the cage-effect on microbiota composition, the animals used for the analysis belonged to different cages and three different litters. Bacterial DNA was extracted using a specific kit (QIAamp Powerfecal DNA kit, Qiagen), and its concentration was quantified by Nanodrop 2000 C Spectrophotometer (ThermoFisher Scientific). The 16S rRNA sequencing and analysis was performed by a service offered by Zymo Research (Irvine, CA, USA).

4.3.1 Targeted library preparation

The DNA samples were prepared for targeted sequencing with the Quick-16S™NGS Library Prep Kit (Zymo Research). The primer sets used were Quick-16S™Primer Set V3-V4 (Zymo Research). The sequencing library was prepared using an innovative library preparation process in which PCR reactions were performed in real-time PCR machines to control cycles and therefore limit PCR chimera formation. The final PCR products were quantified with qPCR fluorescence readings and pooled together based on equal molarity. The final pooled library was cleaned up with the Select-a-Size DNA Clean & Concentrator™, then quantified with TapeStation® (Agilent Technologies, Santa Clara, CA) and Qubit® (Thermo Fisher Scientific, Waltham, WA).

4.3.2 Control samples

The ZymoBIOMICS® Microbial Community Standard (Zymo Research) was used as a positive control for each DNA extraction, if performed. The ZymoBIOMICS® Microbial Community DNA Standard (Zymo Research) was used as a positive control for each targeted library preparation. Negative controls (i.e. blank extraction control, blank library preparation control) were included to assess the level of bioburden carried by the wet-lab process.

4.3.3 Sequencing

The final library was sequenced on Illumina® MiSeq™with a v3 reagent kit (600 cycles). The sequencing was performed with <10% PhiX spike-in.

4.3.4 Bioinformatics analysis

Unique amplicon sequences were inferred from raw reads using the DADA2 pipeline (Callahan et al. 2016). Chimeric sequences were also removed with the DADA2 pipeline.

Taxonomy assignment was performed using Uclust from Qiime v.1.9.1 with the Zymo Research Database, a 16S database that is internally designed and curated, as reference. Composition visualization, alpha-diversity, and beta-diversity analyses were performed with Qiime v.1.9.1 (Caporaso et al. 2010). If applicable, taxonomy that have significant abundance among different groups were identified by LEfSe using default settings (Segata et al. 2011).

4.4 Faecal transplantation

Four different groups of adult (approx. P120) EE C57BL/6J mice, living in different enrichment cages, or 4 different cages of age matched ST mice, were used as donors for this experiment. Recipient mice were adult C57BL/6J conventionally raised in ST condition, and housed 2/3 animals per cage. Before starting the faecal transplantation, the recipient mice were subjected to 1-week ABX in drinking water. After 2 days of washout, faecal transplantation was performed through oral gavage 5 times, once/day (Murakami et al. 2016). To avoid stress for the oral gavage, the procedure was performed for three consecutive days, the animals rested for 2 days, and finally were subjected to the gavage for another 2 days. At the time of faecal transplantation, freshly harvested EE or ST donor faeces were suspended in sterile PBS and mixed with a vortex for 10 min. The suspension was filtered with a cell strainer to remove large debris and immediately used for the transplantation.

Every recipient mouse received 200 µL of suspension volume. A group of mice were orally gavaged with sterile PBS (the vehicle of the faeces suspension).

After the inoculation, mice were left in their home cage to wait for the engraftment of new bacteria species for 4 weeks. Fresh faecal pellets from EE recipient mice were collected before the ABX treatment and 4 weeks after the transplantation. The animals analysed were housed in different cages to avoid the cage-effect on microbiota composition.

4.5 Monocular deprivation

Mice were anesthetized with isoflurane (3% induction; 1% maintenance) and placed on a heated pad maintained at 37°C. The area surrounding the right eye was cleaned in a centrifugal manner with Povidone-iodine diluted 1:1 in saline using cotton swabs. The eye was covered with a thin layer of a dexamethasone/tobramycin ointment (Tobradex, Alcon Novartis) to prevent inflammation and infection. Eyelids were sutured with 3 or 4 horizontal mattress stitches by using a 6-0 surgical suture. After surgery, the animals were monitored and allowed to recover in a heated box.

4.6 Intrinsic optical signal imaging (IOS)

4.6.1 Surgery

Surgery for IOS imaging was performed as described in (Mazziotti et al. 2017). Mice were anesthetized with isoflurane (3% induction; 1% maintenance) and head fixed on a stereotaxic frame using ear bars. Body temperature was monitored using a heating pad and a rectal probe to maintain the animals' body at 37°C. A subcutaneous injection of

lidocaine (2%) was provided to anesthetize the local area and the eyes were protected with a dexamethasone-based ointment (Tobradex, Alcon Novartis). The scalp was removed and the skull cleaned with saline. The skin was secured to the skull using cyanoacrylate and a thin layer of cyanoacrylate was poured over the exposed skull to attach a custom-made metal ring (9 mm internal diameter) centered over the binocular visual cortex. A thin layer of clear nail polish was applied over the area to ameliorate optical access. After surgery, the animals were allowed to recover fully in a heated box and monitored to ensure the absence of any sign of discomfort. Before any other experimental procedure, mice were left to recover for at least 48 hours.

4.6.2 Imaging and data analysis

Mice were anesthetized with isoflurane (3% induction; 1% maintenance) and chlorprothixene anesthesia (1.5 mg/kg, i.p.) at P120 and P123 (after 3 days of monocular deprivation) Images were visualized using a custom Leica microscope (Leica Microsystems). Red light illumination was provided by 8 individually addressable LEDs (WS2812) attached to the objective (Leica Z6 APO coupled with a Leica PlanApo 2.0X 10447178) by a custom 3D-printed conical holder. Visual stimuli were generated using Matlab Psychtoolbox and presented on a gamma-corrected 24" monitor (C24F390FHU).

Horizontal sine-wave gratings were presented in the binocular portion of the visual field enclosed in a Gaussian envelope spanning -10 to +10 degrees of azimuth and -5 to +60 (full monitor height) degrees of altitude, with a spatial frequency of 0.03 cycles per degree, mean luminance 20 $\mathrm{cd\,m^{-2}}$ and a contrast of 90%. The stimulus consisted of the abrupt contrast reversal of a grating with a temporal frequency of 4 Hz for 1 second, time-locked with a 12-bit depth acquisition camera (PCO edge 5.5) using a parallel port trigger. The interstimulus time was 13 seconds. Frames were acquired at 30 fps with a resolution of 540 x 640 pixels. The signal was averaged for at least 8 groups of 20 trials, stimulating each eye alternatively to prevent biases due to different time in anesthesia for the contralateral and ipsilateral eyes. The signal was then downsampled in time to 10 fps and in space to 270 x 320 pixels. Fluctuations of reflectance (R) for each pixel were computed as the normalized difference from the average baseline ($\Delta R/R$). For each recording, an image representing the mean evoked response was computed by averaging frames between 0.5 to 2.5 seconds after stimulation. The mean image was then low-pass filtered with a 2D average square spatial filter (7 pixels). To select the binocular portion of the primary visual cortex for further analysis, a region of interest (ROI) was automatically calculated on the mean image of the response of the ipsilateral eye by selecting the pixels in the lowest 30% $\Delta R/R$ of the range between the maximal and minimal intensity pixel (Cang et al. 2005).

To weaken background fluctuations a manually selected polygonal region of reference (ROR) was subtracted. The ROR was placed where no clear response, blood vessel artifact or irregularities of the skull were observed (Heimel et al. 2007). Mean evoked responses were quantitatively estimated as the average intensity inside the ROI. To measure ocular dominance we used the Ocular Dominance Index (ODI) calculated as where C and I are the mean response amplitude evoked from contralateral and ipsilateral eye stimulation respectively.

For the illustrations in the figures of the signal time course before and after MD, for each animal the contralateral and ipsilateral responses were normalized to the peak

minimum value, and low-passed with a moving average (span: 3 samples). Signals were then averaged within each group.

4.7 Two-photon imaging

4.7.1 Surgery

Cranial windows were implanted on mice around P70. Animals were anesthetized with isoflurane (3% induction; 1% maintenance). Dexamethasone (subcutaneous 0.2 mg/kg) and Lidocaine (2%, 15-20 µL , subcutaneous, scalp area) were administered. After a few minutes, the scalp was cleaned with three swabs of povidone-iodine and a large portion of skin, covering both the hemispheres, was removed. The skull was cleaned from the periosteum by initially using saline and then by carefully scraping it with a scalpel blade. We drew a circular area of 3 mm of diameter centered 3 mm lateral, 1 mm anterior to lambda to mark the craniotomy area and we applied a thin layer of a light-curing dental cement on the rest of the exposed skull (3M Vitrebond plus). A metal head-plate was fixed to the skull by using more dental cement. By carefully using a dental drill and a biopsy punch, a 3 mm circular groove was thinned until almost transparent on the previously marked area, then a few drops of cold sterile ACSF were applied to the area. A circular island of bone was removed with the tip of a sharp forceps without damaging the dura. We placed and held in place a circular 3 mm coverslip on the craniotomy and secured it to the skull by using dental resin (Lang Contemporary Ortho Jet). We then covered thoroughly the skull and the head-plate with more dental resin to finish the surgery. The animals were allowed to recover in a heated box and monitored to ensure the absence of any sign of discomfort. Before any other experimental procedure, mice were left to recover for 12-16 days to reduce inflammation in the surgical area, thus increasing the optical access to the tissue. A more detailed explanation for surgical procedures can be found in (A. Holtmaat et al. 2009).

4.7.2 Imaging and data analysis

Imaging was performed using a Bruker Ultima Investigator microscope equipped with a GaSsP Photomultiplier tube and controlled by the scanning software Prairie View. Laser excitation was provided by a tunable Ti:Sapphire pulsating LASER (Chameleon Ultra, Coherent) tuned at 920 nm and excitation power was controlled with a Pockels Cell. LASER power was maintained under a maximum of 40 mW on the sample.

Images were acquired using a 20x long WD water immersion objective (Olympus XLUMPlanFL N 20x N.A. = 1.00). For each mouse, 1-3 pyramidal neurons with soma position in layer V were imaged. For each neuron, in the first session, we acquired an epifluorescence image of the vasculature of the imaging area to relocate the same dendritic segments on subsequent days. We then acquired a low-magnification two-photon stack of the entire apical dendritic arborization of the cell (1024x1024 pixels, x-y resolution: 0.46 µm /px, z step: 3 µm). 1-5 dendritic segments (imaging depth: 0-200 µm from the brain surface) per cell were chosen randomly between those that had better optical clarity, and a high-magnification stack of those segments was acquired (1024x1024 pixels, x-y resolution: 0.09 µm /px, z step: 1 µm). We ensured similar fluorescence across imaging sessions and,

to prevent phototoxicity, the lowest laser power (<40 mW) that could resolve all spines was used.

Dendritic spines were counted manually with a custom-written MATLAB software by comparing simultaneously single, aligned z planes from the z-stacks of all 8 experimental time points. Images were first low-pass filtered with a 2D Gaussian filter (MATLAB function imgaussfilt, sigma: 1.1). We counted all clear spine protrusions emanating laterally from the dendrite, regardless of their shape (stubby, mushroom, thin). We considered the spines to be the same from one session to the other based on their relative position to structural landmarks and to very clear persistent spines present in all time points. Spines were considered different if they branched out from the dendritic segment more than 1 µm away from their previous position.

Spine Density was defined as the number of spines per µm of length of the dendritic segment. Similarly, the fraction of spines gained (F_{gained}) and lost (F_{lost}) between two time points t1 and t2 were defined as follows $F_{gained} = (N_{gain}/N_{t2}) * 100$ and $F_{lost} = (N_{lost}/N_{t2}) * 100$ (A. J. G. D. Holtmaat et al. 2005; Murmu et al. 2013). The time-dependent survival function was defined as $SF = N_t/N_0$ (Murmu et al. 2013) where N_0 is the number of spines present at the first imaging time point, and N_t is the number of spines of the original set surviving after time t.

4.8 Quantification and statistical analysis

The sample sizes were based on prior studies and are indicated in the figure legend for each experiment. Whenever possible, quantification and analyses were performed blind to the experimental condition.

The majority of statistical analyses were performed using GraphPad Prism version 7 (GraphPad Software, San Diego, CA, USA).

4.8.1 IOS experiments

Differences between groups were tested for significance using two-way RM ANOVA, unless otherwise indicated. Holm–Sidak's multiple comparisons post hoc tests were performed, when appropriate, to correct for multiple hypothesis testing.

4.8.2 Dendritic spines analysis

Differences in spine density were evaluated using a two-way RM ANOVA time∗housing. Holm–Sidak's multiple comparisons post hoc tests were performed, when appropriate, to correct for multiple hypothesis testing. Spine formation and elimination were compared with two-tailed t-test when comparing two housing groups, or with two-way RM ANOVA when comparing more than two groups.

Part II

A brain-wide analysis of perineuronal nets in the mouse reveals complex interactions with parvalbumin neurons and correlations with gene expression

5 Introduction

This part represents a project that is still unpublished.

5.1 Introduction to the project

Perineuronal Nets (PNNs) are specialized reticular structures of the extracellular matrix (ECM) that ensheath neurons. They are present throughout the entire mouse brain, surrounding primarily parvalbumin-expressing (PV) fast-spiking GABAergic interneurons (Galtrey et al. 2008; Hendry et al. 1988; Köppe et al. 1997; Seeger et al. 1994). PNNs aggregate progressively during postnatal development, in parallel with the closure of critical periods for developmental plasticity (Pizzorusso et al. 2002; Elena Maria Boggio et al. 2019; Reichelt et al. 2019; Ye et al. 2013), and, although their precise composition varies between brain regions, there are three essential molecular constituents: hyaluronic acid, glycosylated proteins called chondroitin-sulfate proteoglycans (CSPGs), and link proteins like "hyaluronan and proteoglycan link protein 1" (HAPLN1) and Tenascin-R, that stabilize the binding between the other components (Carulli et al. 2010; Dauth et al. 2016; Kwok et al. 2010). CSPGs are also the binding target of the lectin Wisteria floribunda agglutinin (WFA), the most widely used marker to visualize PNNs in histological analyses (Fawcett et al. 2019; Härtig et al. 1999).

The precise contribution of PNNs in regulating neuronal and brain function is a strongly active area of research. Many roles have been proposed, but a key overarching theme is that PNNs tightly control the plasticity and stability of neuronal circuits. This function has been studied throughout many cortical and subcortical regions of the brain. For example, PNNs control ocular dominance plasticity in the visual cortex (Pizzorusso et al. 2002; Carulli et al. 2010), fear memory extinction in the amygdala (Gogolla et al. 2009), spatial representation stability of grid cells in the entorhinal cortex (Christensen et al. 2021), associative motor learning in the cerebellum (Carulli et al. 2020), and social memory in the hippocampus (Cope et al. 2021). Enzymatically digesting PNNs has also been shown to promote plasticity and to improve recovery after damage to the central nervous system (Bradbury et al. 2002). Moreover, PNNs stabilize neuronal circuitry by protecting fast-spiking neurons against oxidative stress (Cabungcal et al. 2013) a risk factor for psychiatric diseases. Indeed, abnormalities in PNNs that render PV cells more susceptible to oxidative damage, have been described in schizophrenic patients (Pantazopoulos et al. 2010).

Despite these general features, however, PNNs also show a remarkable degree of variability between different brain regions both in terms of structure and function (Ueno et al. 2018). For example, while in most of the isocortex, PNNs aggregate primarily around PV neurons, in the hippocampal CA2 they also ensheath excitatory pyramidal neurons, suggesting a different biological function in this region (Carstens et al. 2016). Moreover, at the functional level, the enzymatic removal of PNNs has diverging effects in the cortex, where it enhances LTD (Romberg et al. 2013), and in the hippocampus, where

it impairs both early-phase LTP and LTD (Bukalo et al. 2007). The lack of understanding of the principles of PNN organization throughout the brain hinders our comprehension of their functional role and possible therapeutic implications. Moreover, the degree to which PNNs are linked to PV cells across brain areas has not been systematically studied.

To solve this problem, it is essential to build a common and highly quantitative atlas of PNNs and PV in the entire brain. Such data would be of critical interest for many reasons. First, by studying the brain-wide expression of PNNs and co-localization with PV neurons, it would be possible to highlight patterns that are suggestive of their functional role. Second, quantitative data are increasingly necessary to guide and constrain computational models of the brain. Third, since PNNs are a converging target for global genetic and environmental regulatory factors (Fawcett et al. 2019) like microRNAs (Napoli et al. 2020), environment (Bartoletti et al. 2004), and diet (Reichelt et al. 2021), such an atlas would allow comparing the effects of experimental manipulations in an unbiased and brain-wide manner against a common reference. To achieve maximal utility, this dataset should be registered to a coordinate space that is shared across researchers and research fields, like the Allen Institute Common Coordinate Framework version 3 (CCFv3) (Q. Wang et al. 2020). In this way, it would be possible to correlate the distribution of PNNs with publicly available region-specific datasets of different area properties, like gene expression (Lein et al. 2007), connectivity patterns (Oh et al. 2014), and neuronal activity (Vries et al. 2020), thus enabling researchers to unveil, in a hypothesis-free manner, molecular and functional correlates of PNN presence. Moreover, it would streamline and encourage replication and validation studies to converge on a community-driven picture of PNNs in the mouse brain.

Several studies analyzed PNNs in multiple brain regions (Dauth et al. 2016; Ueno et al. 2018), however, they have been limited by a combination of factors including the focus on only a subset of areas, a qualitative approach, or the usage of a non-standard reference volume. Overcoming all of these limitations poses a complex set of challenges. First, in order to upscale the analysis to whole-brain data from many animals, it is mandatory to have an automatic method for cell detection and segmentation. While many computational tools are available to this end, PNNs are particularly hard to automatically detect, due to their vast morphological variability between areas. As a result, simple machine learning models fail to generalize across the entire brain. Furthermore, the number and density of nets might not be the only relevant metrics to get a complete picture of the relevance of PNNs in an area. In fact, the intensity of staining of individual cells or nets has been correlated to different functional properties both for PV cells (Donato et al. 2013) and for PNNs (Napoli et al. 2020). Moreover, most CSPGs are present in a diffuse form in the ECM, and not aggregated in PNNs (Deepa et al. 2006), thus implying that the distribution pattern of PNNs has to be disambiguated from that of WFA diffuse staining. A final challenge is also to make such multidimensional data accessible and browsable so that it can be readily used to support other researchers in formulating new hypotheses or experiments.

Here, we present an atlas for PNNs and PV neurons in the mouse brain. We provide multiple quantitative measurements for PNNs, PV cells, and their interaction for about 600 different brain areas. We release two deep learning models, pre-trained on a dataset of about 0.8 million manually annotated PNNs and PV cells for their automatic detection. We then show that thanks to our dataset, it is possible to detect connectivity and gene expression patterns that correlate with PNN presence. We think these resources will have

a high impact in facilitating research on PNNs.

5.2 Personal contribution to the project

Here I summarize, for clarity, the details of my specific personal contribution to this project. All of the conceptual, experimental and analytical tasks are grouped according to the level of my involvement in three categories as follows:

- I was the only/main contributor
  - Conceptualization of the project
  - Histology preparations
  - Image acquisition
  - Design of a standardized pipeline for image registration and analysis
  - Writing software for image registration and analysis
  - Figures layout and data visualizations
  - Image alignment to the reference atlas and preprocessing
- I collaborated in the tasks
  - Assembled training dataset for the deep learning models
  - Development of software for interacting with the Allen-Brain Institute API
  - Development of a Random Forest model for PNN and PV segmentation
- Task performed by other people or institutions
  - Development of a Deep-Learning architecture for counting PNNs and PV cells

6 Results

6.1 PNN and PV cells quantification in the mouse brain

In our analysis pipeline, we first performed immuno-/lectin histochemistry on serially collected whole-brain coronal slices of 5 adult mice, staining sections with both WFA and an anti-PV antibody (Figure 6.1A). We then acquired fluorescence images and registered them to the Allen Institute CCFv3 to achieve two goals: first, that each image pixel was annotated with an ID corresponding to a brain area, and second, that for each slice, we could define a transformation that maps 2D coordinates in the experimental images to 3D coordinates in the CCFv3 reference volume (Figure 6.1A).

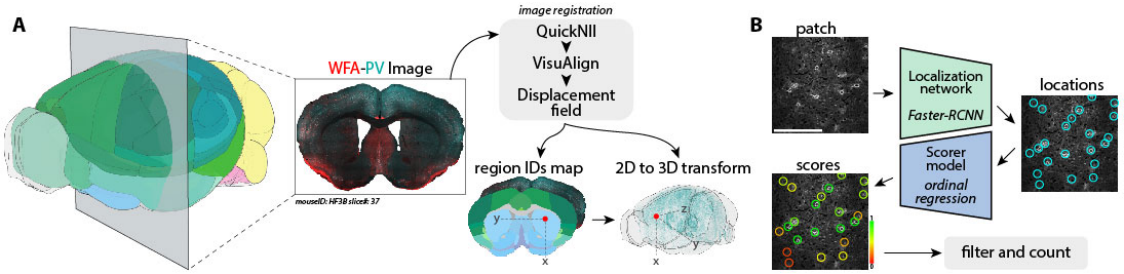

Figure 6.1: **Image registration pipeline. (A)** Schematic of the pipeline for slice registration to the Allen Institute CCFv3 reference volume. **(B)** Schematic of the strategy for cell counting. Two different modules were used, a larger convolutional neural network for localization and a smaller one for scoring. Scale bar: 200 µm

To automatically detect the (x,y) coordinates of PNNs and PV cells, we trained two deep convolutional neural networks with a dataset comprising roughly 0.67 million manually annotated PNNs and 0.16 million PV cells (Figure 6.1B). When an experimenter manually counts non-trivial structures on a large scale, the resulting annotations can contain inconsistencies due to changing illumination conditions, experimenter fatigue, or different judgements, spanning from conservative to liberal. This could potentially produce a training dataset that inherits biases from the experimenter who labeled it. To address this issue, we implemented a second stage whereby we assigned a confidence score to each object detected in the previous stage. This scorer module was trained on two smaller datasets (4727 PNNs and 5833 PV cells) labeled by 7 independent expert raters. The aim is to produce scores for each putative object that are specifically calibrated to maximally correlate with the raters' agreement. A detailed description of this method is available in (Ciampi et al. 2022). In our multi-rater dataset, the average agreement (Jaccard index) between expert raters was 64% for PNNs and 70% for PV cells, demonstrating relevant individual differences in counting strategies between scorers (Figure 6.2C).

After detecting PNNs and PV cells, we assigned each one an intensity value by averaging the values of the pixels belonging to the object, segmented from a small (80x80pixels)

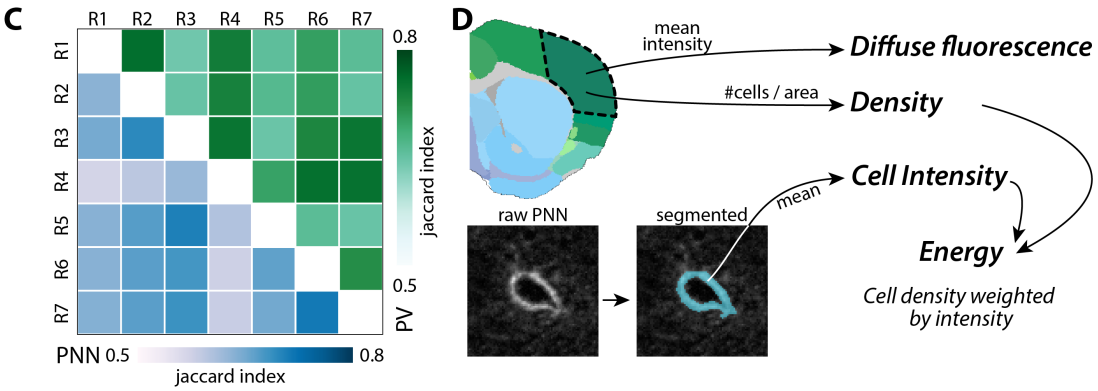

Figure 6.2: **Image analysis pipeline. (C)** Agreement (Jaccard index) between the manual cell annotations of 7 independent raters (R1-R7). The lower part of the matrix (blue shade) represents agreement in PNN counts, while the upper part (green shade) represents agreement in PV counts. **(D)** Diagram showing a graphical explanation of the four metrics used to quantify PNN staining.

patch centered on the (x,y) coordinates of the object. We then defined metrics to describe different aspects of the immunostaining signal in each brain region. To quantify global staining intensity in a region, we defined diffuse fluorescence as the average pixel intensity value in a region. This measure includes the signal coming from diffuse CSPGs not aggregated in a PNN, and the PNN signal. To describe the distribution of single PNNs/PV-cells we defined density, corresponding to the number of objects per unit of surface area, and cell intensity, describing the average staining intensity of individual PNNs or PV cells in a region in the range (0-1). Finally, we reasoned that the functional relevance of PNNs or PV cells in a region might be better represented by a single metric that integrates both the density and the intensity of cells. We thus defined energy, as the density multiplied by the average cell intensity (Figure 6.2E, see 8.7.1 for details). Diffuse fluorescence and energy were normalized within each mouse by dividing them by their respective value calculated on the entire brain. As a result, a value of 1 equals the brain's average and, importantly, the two metrics have the same scale. In the rest of the paper, we will use diffuse fluorescence and energy respectively as "global" or "cellular" measurements.

6.2 Dishomogeneous distribution of PNNs across the mouse brain

To describe the distribution of PNNs in the entire brain we first aggregated data in 12 major brain subdivisions (Figure 6.3A, see Table 1). These regions had highly different values for both WFA diffuse fluorescence and PNN energy (see Table 6.1 for statistical comparisons). Diffuse fluorescence, which includes the signal from CSPGs not aggregated in PNNs, was highest in the olfactory areas, followed by more posterior parts of the brain including the midbrain, pons, and medulla. Isocortex, hippocampal formation, cortical subplate, and hypothalamus displayed intermediate fluorescence levels, while striatum, pallidum, thalamus, and cerebellum had lower diffuse fluorescence. We then looked at

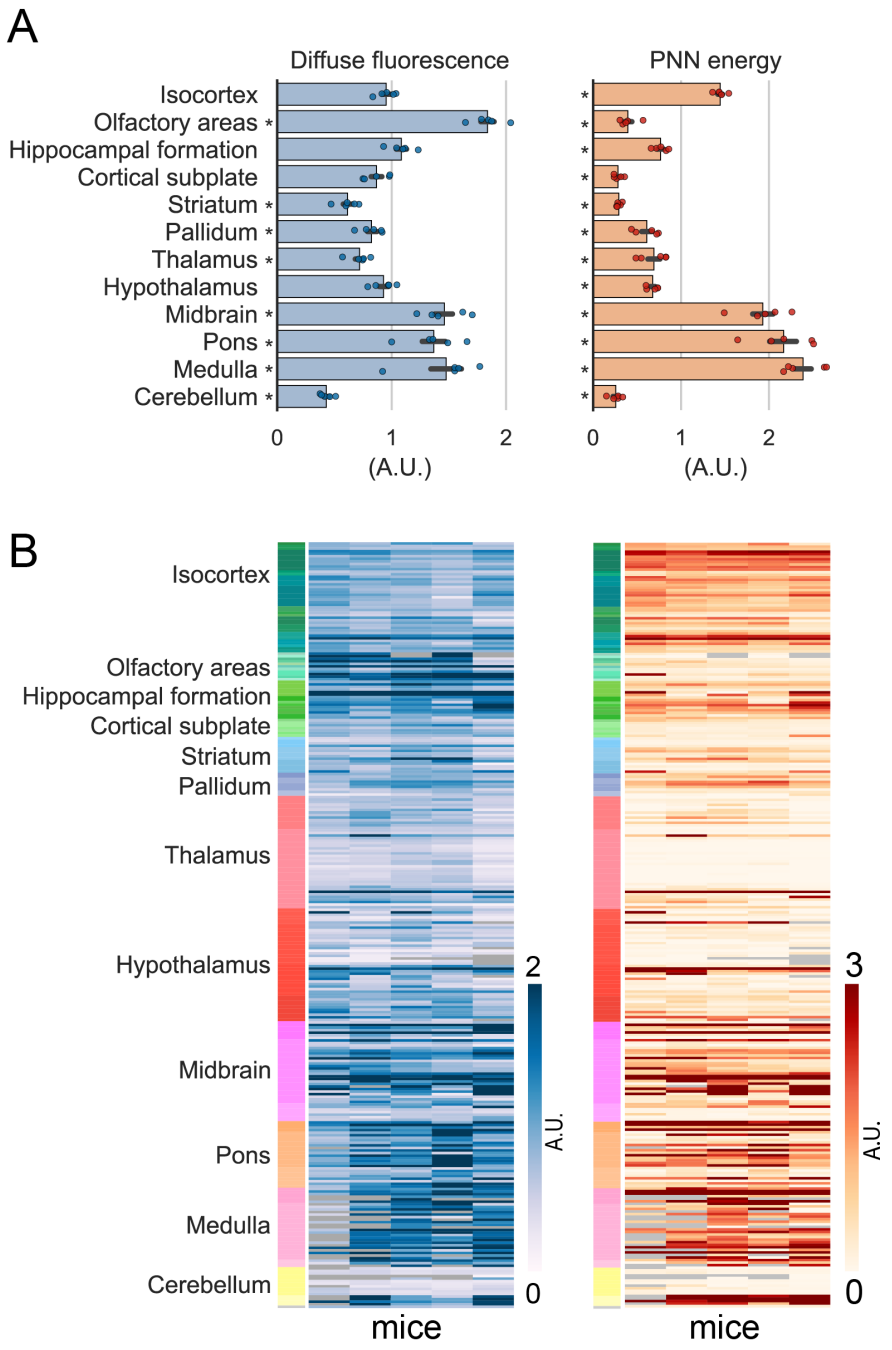

Figure 6.3: **Distribution of WFA-positive PNNs coarse and mid resolution. (A)** Quantification of diffuse fluorescence and PNN energy for 12 aggregated major brain subdivisions. Dots represent mice. Asterisks indicate brain subdivisions significantly different from the brain average (value of 1) (one sample t-test). **(B)** Heatmap showing the same quantification metrics for mid-ontology brain regions in individual mice. Grayed-out cells represent brain regions where data is not available due to no sampling of that region. See Table 6.1 for statistical comparisons.

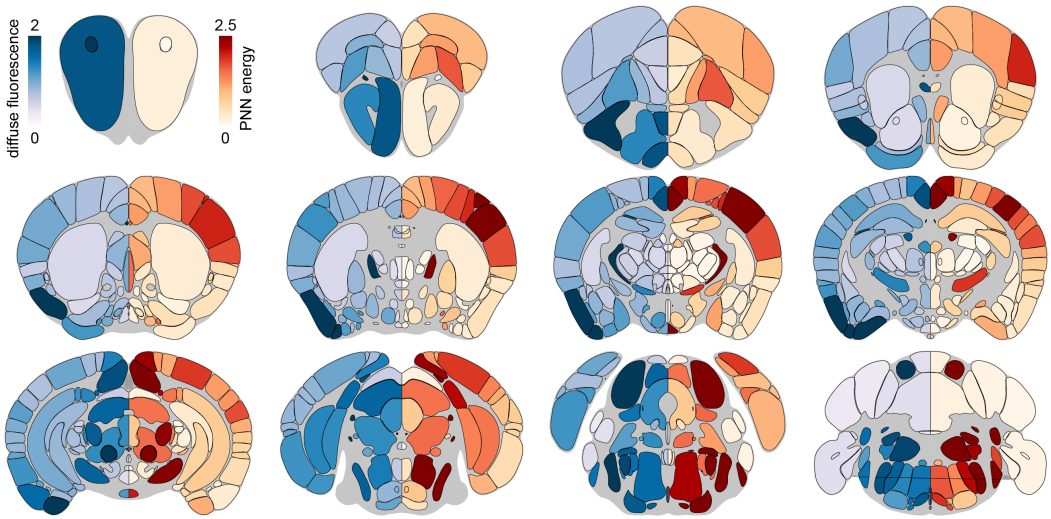

Figure 6.4: **Heatmaps for the distribution of WFA-positive PNNs.** Heatmaps showing coronal sections of the brain, sliced at different anteroposterior locations. On the left hemisphere (blue colormap) is displayed average diffuse WFA fluorescence, while on the right hemisphere (red colormap) is displayed average PNN energy for each brain region.

PNN energy, representing aggregated PNNs in a region. The general pattern was similar, but the differences between areas were much sharper: midbrain, pons, medulla, and isocortex had more PNN energy than the brain average, while all the other areas had significantly lower.

We then grouped data in a set of 316 mid-ontology brain regions (Figure 6.3B, see Table 3). The profile of both metrics was consistent across individual mice and it showed that, within the same major subdivision, individual brain regions can have remarkably diverse values for both diffuse fluorescence and PNN energy (Figure 6.6). To better visualize results at this level of resolution, we plotted the average of both metrics across mice in a series of brain heatmaps coronally sliced at 12 anteroposterior locations ((Figure 6.4). This visualization highlighted that both the diffuse and the cellular measurements of PNNs often varied together, but some areas showed striking differences between the two metrics. To quantify this, we plotted WFA diffuse fluorescence versus PNN energy for the major brain subdivisions (Figure 6.5A). Isocortex, midbrain, pons, and medulla were skewed towards the top-left side of the plot, indicating that they are characterized by strong individual aggregated PNNs, but relatively weak diffuse CSPG signal. Conversely, all the other brain subdivisions showed an opposite effect. Notably, for the olfactory areas, we measured the highest difference between the two metrics, with a strong level of diffuse fluorescence but almost absent aggregated PNNs.

We then split these subdivisions into mid-ontology regions and explored the relationship between the two metrics within each group of brain areas (Figure 6.5B). We found that WFA diffuse fluorescence and PNN energy were significantly correlated in all subdivisions except for olfactory areas and the cortical subplate, but the strength of such correlation was not uniform with striatum and pallidum being respectively the least and most correlated areas (spearman r=0.59 and 0.95). Importantly, some regions deviated from

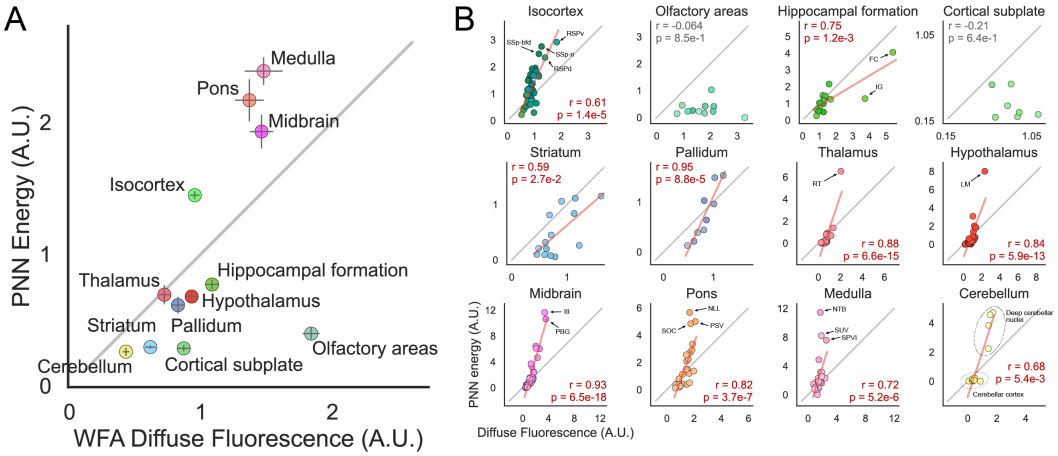

Figure 6.5: **Correlation between PNN metrics. (A)** Plots of PNN energy versus WFA diffuse signal for each of the 12 major brain subdivisions. **(B)** Same as in A but data is split in each brain region of the 12 major brain subdivisions. Text insets indicate the Spearman correlation coefficient and the corresponding p-value, the gray line indicates the X-Y bisector, and, for significant correlations highlighted in red, the red line shows the best linear fit.

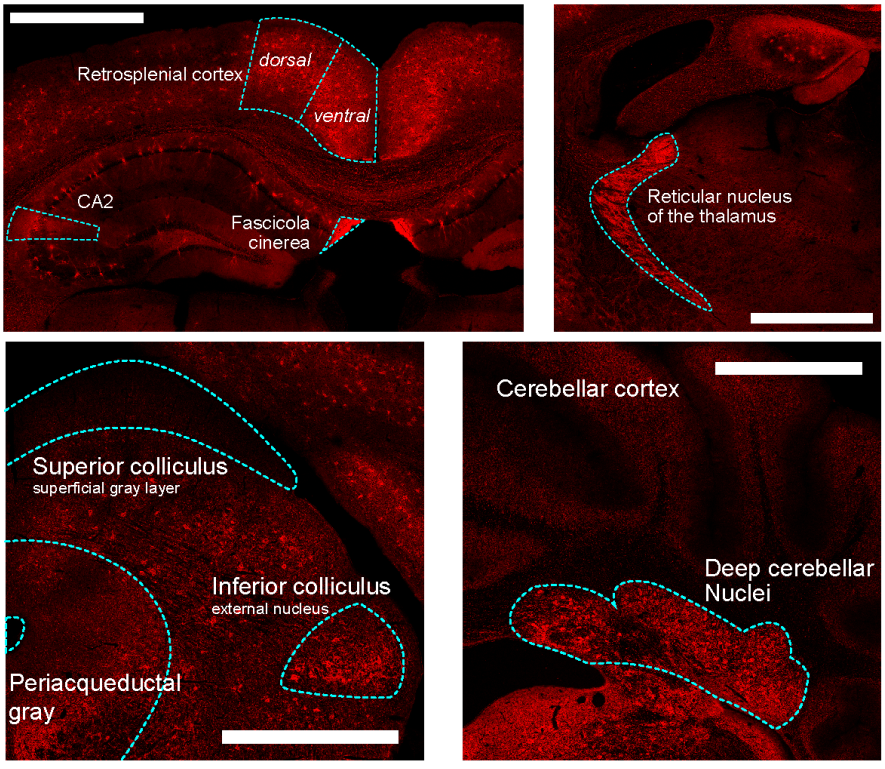

Figure 6.6: **Representative WFA staining in a selection of brain areas.** Scalebar: 1mm.

the population distribution within their major subdivision. In the isocortex, the dorsal and ventral retrosplenial cortex (RSPd, RSPv), as well as the barrel field and nose-related areas of the primary somatosensory cortex (SSp-bfd and -n), had very high PNN energy. Similarly, the reticular nucleus of the thalamus (RT) and the lateral mammillary nucleus (LM) had a stronger PNN staining compared to other areas in the thalamus and the hypothalamus respectively. In the hippocampal formation, the fascicola cinerea (FC) and induseum griseum (IG) had an extremely intense WFA signal. In the cerebellum, brain regions were clustered in areas of the cerebellar cortex, with low WFA staining, and deep cerebellar nuclei, with much stronger PNNs (Figure 6.6). These data represent the first systematic and highly quantitative description of the distribution of PNNs in the entire mouse brain.

6.3 Brain-wide colocalization of PNNs and PV cells

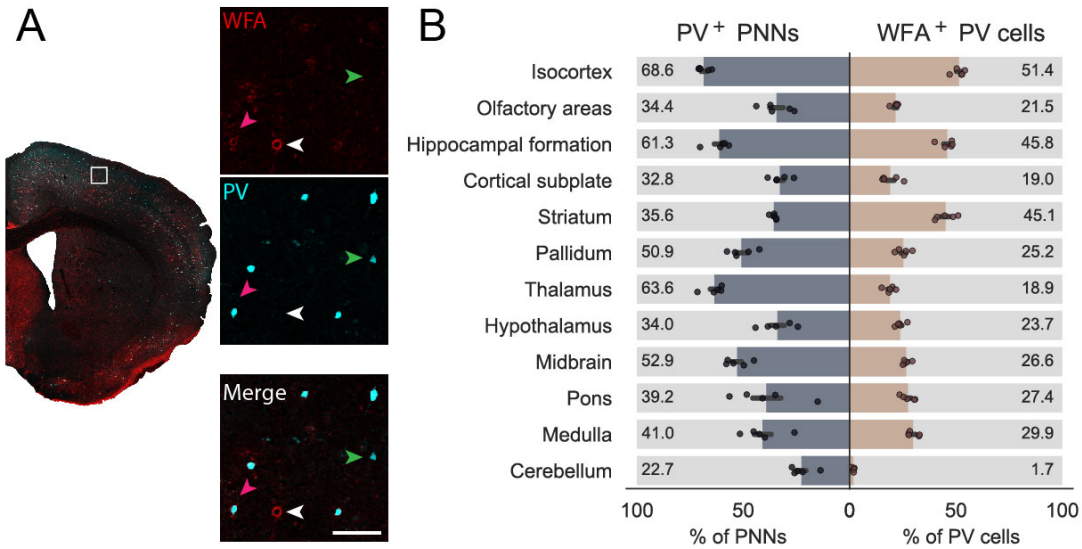

Figure 6.7: **PNN and PV colocalization. (A)** Representative image of a brain slice stained with WFA (red) and anti-PV (cyan). The white inset is magnified on the right, where split channels are also shown. Arrowheads show examples of PV cells without a PNN (green), colocalized PV-PNNs (magenta), and PNNs not surrounding a PV cell (white). Scale bar: 100µm. **(B)** Colocalization percentages across 12 major brain subdivisions (on the left, the fraction of PNNs containing a PV cell; on the right, the fraction of PV cells surrounded by a PNN). Dots represent mice. (N=5 mice, 66,345±6,051 PNNs and 110,990±10,079 PV cells per mice).

In the same brain slices used for PNN analysis, we also stained PV-positive inhibitory interneurons (Figure 6.7A). Studies performed on specific brain areas suggested that PNNs preferentially aggregate around inhibitory PV-positive interneurons (Fawcett et al. 2019), however, exceptions have been described (Carstens et al. 2016). To explore this relationship, we quantified PNN and PV colocalization as the percentage of PNNs containing a PV cell (PV+ PNNs) or as the percentage of PV cells that are surrounded

by a PNN (WFA+ PV cells). On average, in the entire brain 55.9±0.7% of PNNs were located around a PV cell, while about one third of all PV cells in the brain (33.5±1.2%) were surrounded by a PNN. After splitting the data into 12 brain subdivisions, we found that the relationship between PNNs and PV cells was highly heterogeneous (Figure 6.7B). In the isocortex, hippocampal formation, and thalamus, PNNs surrounded PV cells in more than 60% of the cases, reaching, for example, 80.3±1.4% in the retrosplenial cortex (RSPv), 77.7±0.8% in layer 4 of the primary visual cortex (VISp4), and 75.7±0.5% in the anterior cingulate area (ACAv). In all the other regions except the cerebellum, this was the case for at least one third of the PNNs, with the Arcuate hypothalamic nucleus (ARH) having the lowest value of 0.7±0.1%.

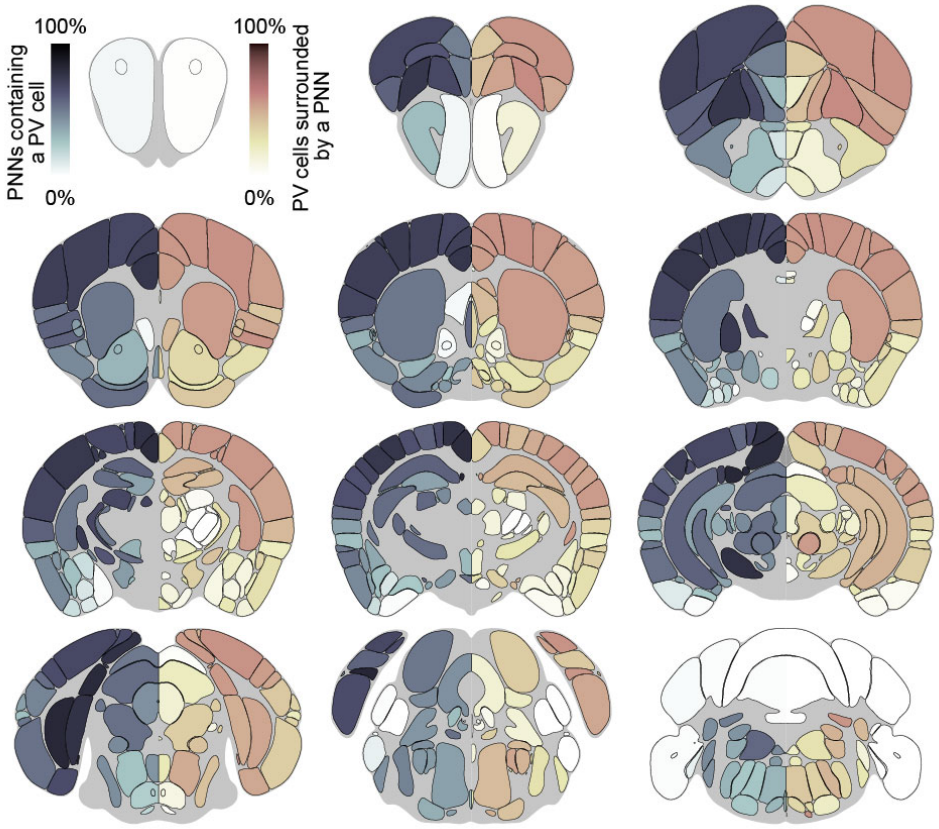

Figure 6.8: **PNN-PV colocalization heatmaps.** Heatmaps showing coronal sections of the brain, sliced at different anteroposterior locations. On the two hemispheres are represented the percentage of PNNs containing a PV cell (left side) and the percentage of PV cells surrounded by a PNN (right side).

Conversely, analyzing the percentage of PV cells surrounded by a PNN, we saw that in most brain areas, only between 20 and 30% of the PV cells are enwrapped by a WFA-positive PNN. A different pattern was present in the isocortex, hippocampal formation, and striatum, where colocalization was much higher (about 50% of PV cells, reaching for example 72.5±0.8% in VISp4 and 57.9±0.5% in the primary motor cortex (MOp)), while in the cerebellum, only very few PV-positive cells had a PNN, likely due to the high amount of Purkinje cells in the cerebellar cortex that all lack PNNs (Baimbridge

et al. 1982; Bastianelli 2003). As before, we also aggregated data in mid-ontology brain regions and measured colocalization metrics in individual areas to reveal patterns with finer resolution (Figure 6.8).

Given the high degree of colocalization, we next asked whether PNN and PV staining were correlated across brain regions. To this end, we plotted either WFA diffuse fluoresce (Figure 6.9A) or PNN energy (Figure 6.9B) as a function of PV energy. We found that, throughout all areas of the brain, WFA and PV staining metrics were significantly correlated. When performing the same analysis at a finer resolution, however, only a subset of brain subdivisions showed a high degree of correlation between WFA and PV (Figure 6.9C,D). The diffuse staining of CSPGs was positively correlated to PV energy in isocortex, thalamus, hypothalamus, and midbrain. Interestingly when we compared cellular metrics for both PNNs and PV (PNN energy vs PV energy) correlation coefficients generally increased with isocortex showing the most striking trend. Here, PV energy alone could explain 85% of the variance in PNN energy (r2=0.846).

To further explore the relationship between PNNs and PV cells, we analyzed staining intensity of single cells. First, we looked at the intensity distribution of PNNs (Figure 6.10A) and PV cells (Figure 6.10B) across our entire dataset. Both PNNs and PV cells had a bimodal intensity distribution, suggesting that each could be composed of two subpopulations. For PV cells, it has been previously reported that two distinct network configurations might exist, one more permissive towards plasticity and characterized by weak expression of parvalbumin (low-PV), and another that limits plasticity and with strong parvalbumin expression (high-PV) (Donato et al. 2013). These two subpopulations likely reflect distinct schedules of neurogenesis and connectivity (Donato et al. 2015). Since PNNs are known to inhibit plasticity, we asked if high-PV cells were more likely to have a PNN. This could potentially explain their plasticity-blocking effect. To do this, we grouped all PV cells in four intensity classes of equal width (1:low, 2:intermediate-low, 3:intermediate-high, and 4:high) and measured the probability of being surrounded by a PNN as a function of PV cell intensity.

Overall, we found that as PV intensity increased, the probability of having a PNN increased (Figure 6.10C). However, upon repeating the analysis for each brain subdivision, we noticed 3 different patterns (Figure 6.10D). In isocortex, hippocampal formation, and striatum, this effect was markedly stronger (first-degree coefficient of the linear fit) and more consistent (F statistic). The olfactory areas, cortical subplate, thalamus, and midbrain had a weaker, albeit significant effect, while in all the other areas, the intensity of a PV cell had no effect (or an opposite one in the cerebellum) on whether or not that cell had a perineuronal net. Interestingly, despite having the highest PNN energy in all the brain (Figure 6.3A,B), hindbrain structures like pons and medulla had PNNs which aggregated on PV cells irrespectively of their staining intensity. This suggests that the regulatory mechanisms that determine the aggregation of a PNN are either different across brain subdivisions or differentially depend on PV expression levels.

6.4 PNN distribution in the cerebral cortex

The precise functional role of PNNs in the cerebral cortex is still a matter of research. We reasoned that by analyzing their expression pattern throughout the cortex we could highlight principles of organization that might explain why only specific areas and cell

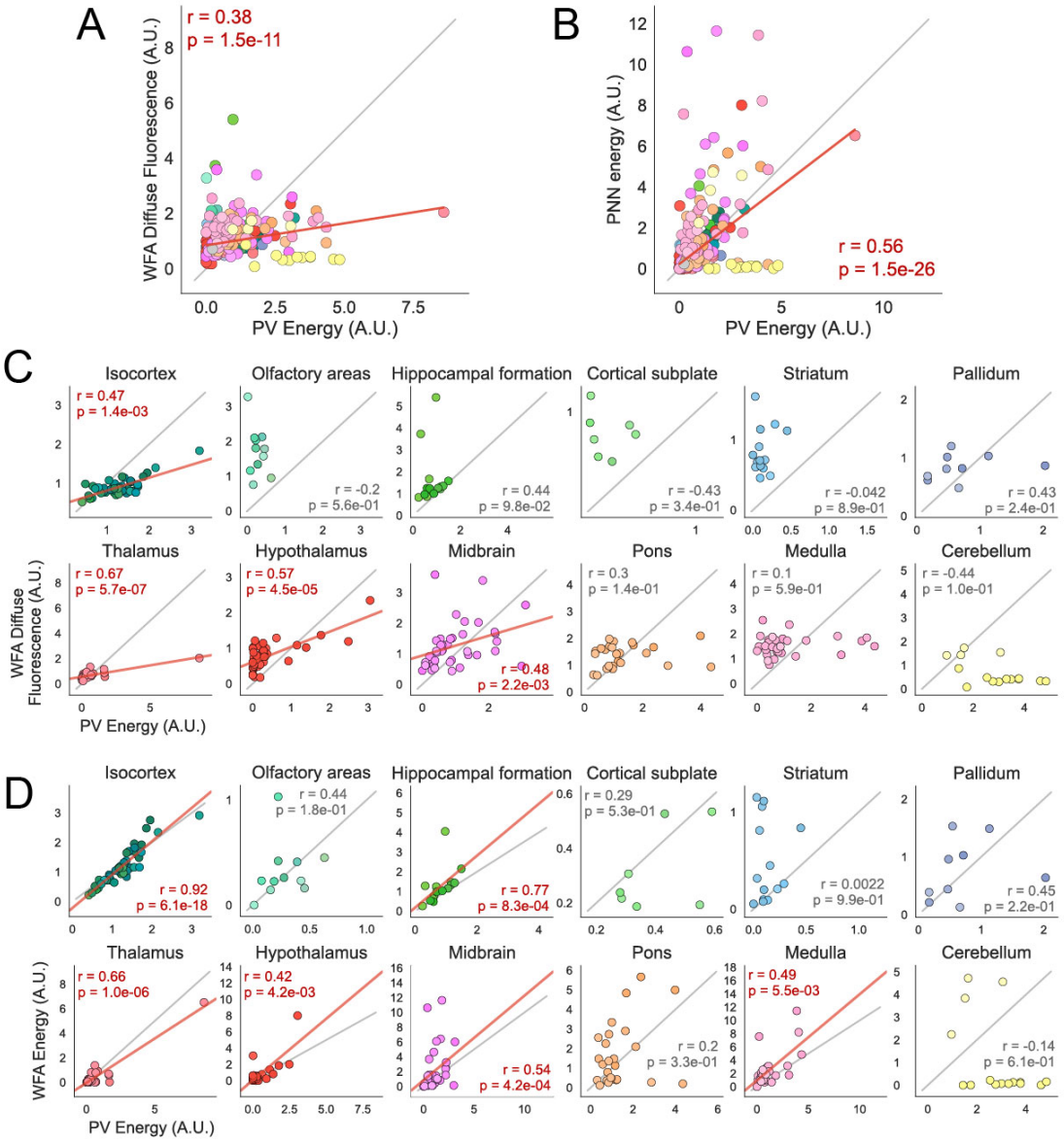

Figure 6.9: **Correlation between PNN and PV metrics.** **(A)** WFA diffuse fluorescence versus PV energy for brain areas at mid-ontology level. **(B)** WFA energy versus PV energy for brain areas at mid-ontology level. **(C)** Same as in A, but areas are split in each major brain subdivision. **(D)** Same as in B, but areas are split in each major brain subdivision. Text insets indicate the Spearman correlation coefficient and the corresponding p-value, the gray line indicates the X-Y bisector, and, for significant correlations highlighted in red, the red line shows the best linear fit.

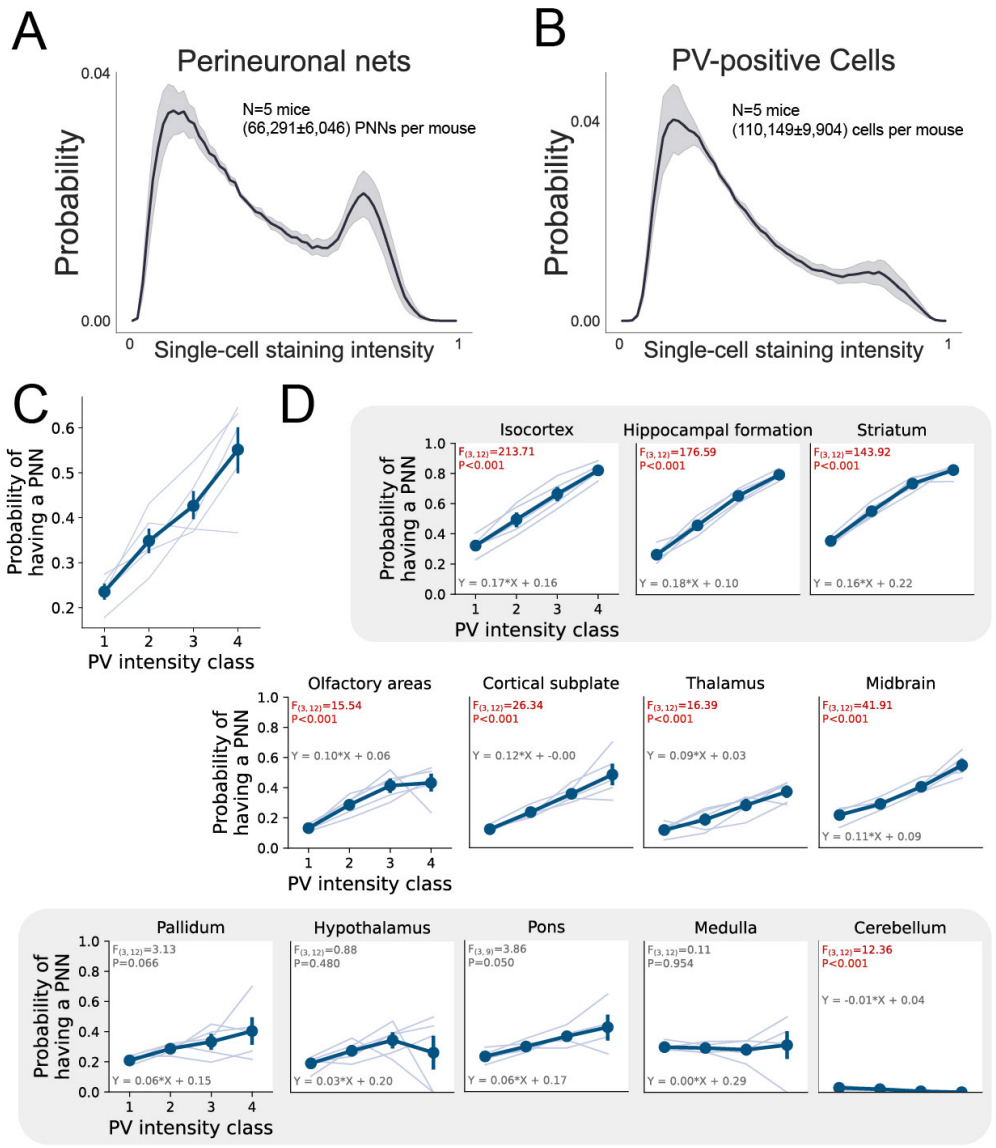

Figure 6.10: **PNNs aggregation depends on PV expression.** **(A)** Probability density function of the intensity of all PNNs. The thick line represents the average across mice. **(B)** Same as in A but for PV+ cells. **(C)** Probability that a PV cell is surrounded by a PNN as a function of PV intensity class (1: low, 2: intermediate-low, 3: intermediate-high, 4:high) calculated for the whole brain. **(D)** Same as in C, but split in each major brain subdivision and grouped in: strongly PV-dependent, weakly PV-dependent, and PV-independent areas. Text insets indicate the result of a one-way RM ANOVA (F statistics and p-value), and the estimated parameters of the best first degree linear fit. See Table 6.1 for statistical comparisons.

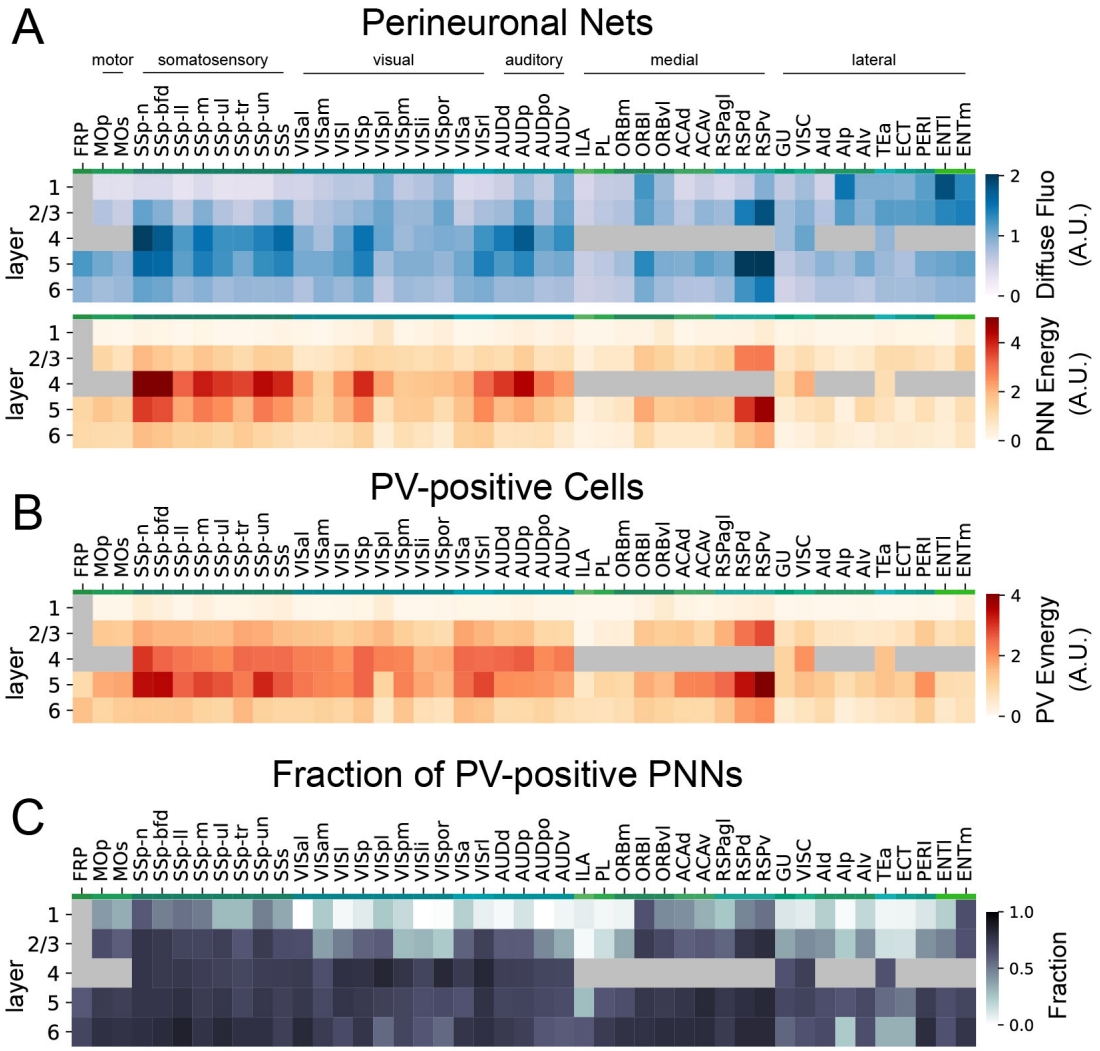

Figure 6.11: **PNN organization in the cerebral cortex. (A)** Heatmaps representing WFA diffuse fluorescence and PNN energy. Average metrics across mice are shown for each cortical area and layer (area acronyms available in table Table 2). **(B)** Same as in A but for PV energy. **(C)** Same as in A but for the fraction of PNNs colocalized with PV cells.

types necessitate being enwrapped in a PNN. Furthermore, the cerebral cortex is divided in layers with different functional properties and PNN expression. We thus focused on the cortex and plotted WFA diffuse fluorescence and PNN energy in all cortical regions divided by layer (Figure 6.11A).

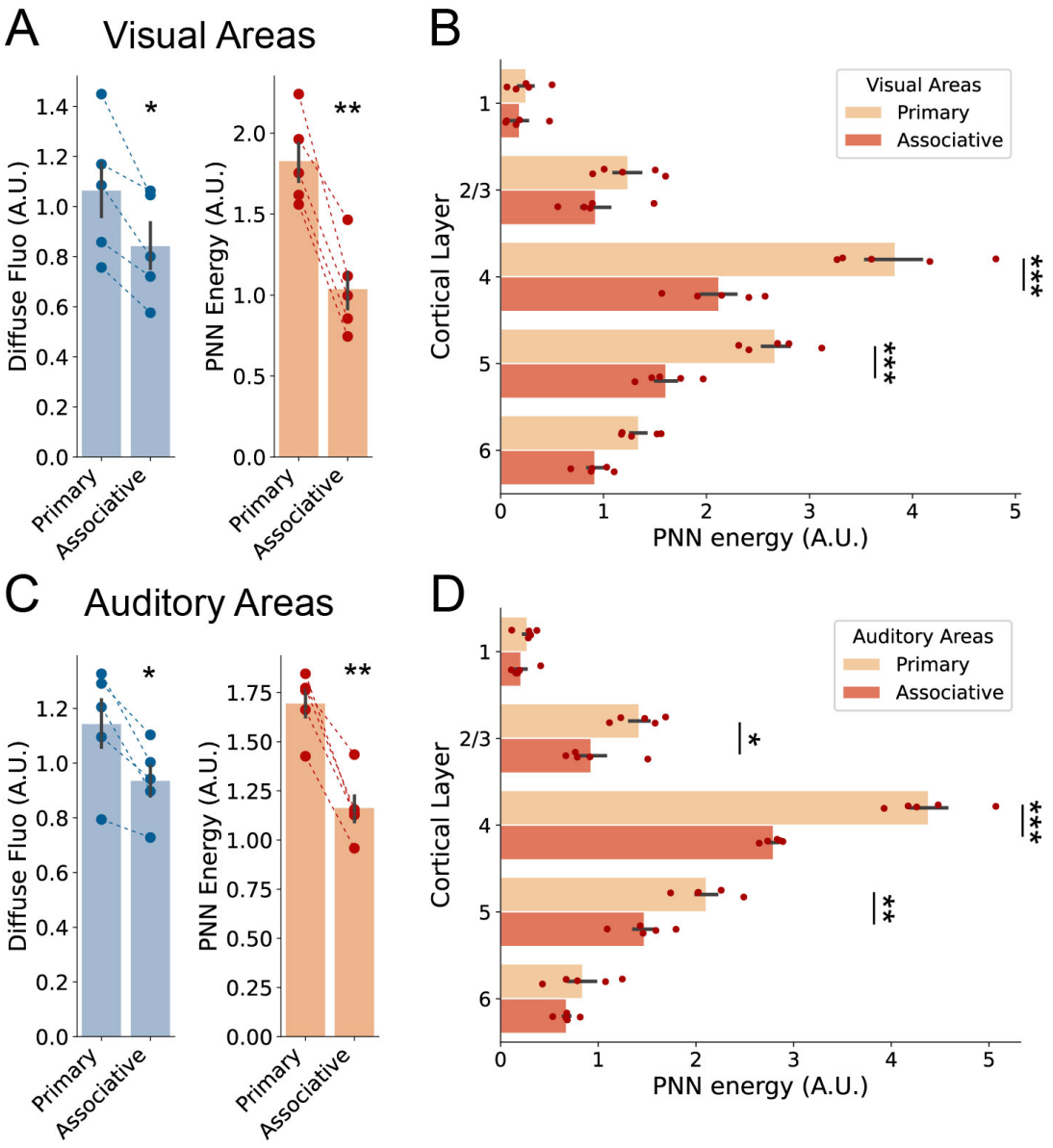

Figure 6.12: **PNNs in primary and secondary cortices. (A)** WFA diffuse fluorescence and PNN energy in the primary visual cortex versus higher-order associative visual areas. **(B)** PNN energy in primary versus associative visual cortical areas split by layer. **(C)** WFA diffuse fluorescence and PNN energy in the primary auditory cortex versus higher-order associative visual areas. **(D)** PNN energy in primary versus associative auditory cortical areas split by layer. cells. See Table 6.1 for statistical comparisons.

As previously described, WFA staining was generally more abundant in layers IV and

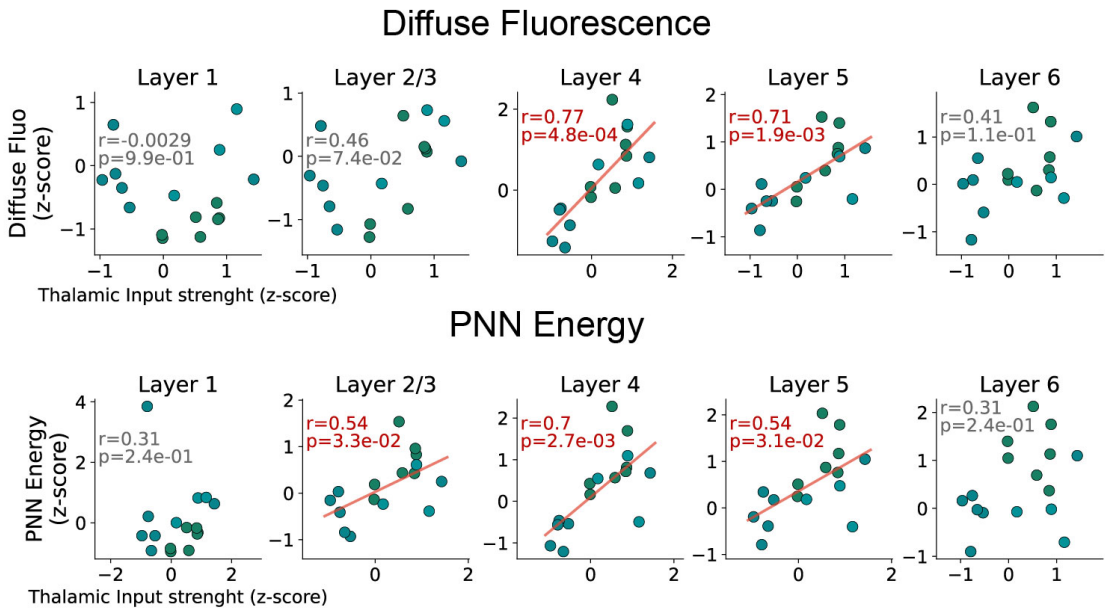

Figure 6.13: **PNN organization and thalamic inputs.** Correlation between standardized WFA diffuse fluorescence and standardized thalamic input strength in sensory-related areas of the cortex (all somatosensory, visual, and auditory cortices, see methods) split by layer. Text insets indicate the Spearman correlation coefficient and the corresponding p-value, and, for significant correlations highlighted in red, the red line shows the best linear fit.

V. We noticed that four main region groups were characterized by a stronger diffuse WFA staining: primary somatosensory, visual and auditory areas and the retrosplenial cortex. When analyzing aggregated PNNs (PNN energy), this pattern was much sharper and more localized in layer IV. Interestingly, in somatosensory, visual, and auditory regions, primary areas PNN energy was particularly high, while PV cells, despite sharing the same general organization throughout the cortex, did not show this enrichment in primary regions (Figure 6.11B). The proportion of PNNs that surrounded a PV cell was similarly uniform (Figure 6.11C). To further investigate this pattern, we aggregated data in primary (VISp) and associative (VISpor, VISli, VISl, VISpl, VISpm, VISal, VISam, VISrl, VISa) visual cortical regions. Both diffuse fluorescence and PNN energy were lower in associative visual areas (Figure 6.12A) and when we split data between layers, this effect was present only in layer IV and V (Figure 6.12B). An analogous effect was present between primary (AUDp) versus associative (AUDv, AUDd, AUDpo) auditory areas (Figure 6.12C), but here layer 2/3 also showed a smaller but significant effect (Figure 6.12D). A similar trend, however, was not present for somatosensory areas, where the supplementary somatosensory area SSs was also strongly labeled.

These data show that CSPGs are more distributed in layers IV-V of the cortex and that PNNs tend to aggregate preferentially in primary sensory regions, preferentially in layer IV. All these lines of evidence prompted us to speculate that a general organizational principle of PNN organization throughout the cortex might be related to the control of thalamic inputs that are mainly received in layer IV and are strongest in primary sensory

regions. Indeed, in the primary visual cortex, PNNs were found to control thalamic feed-forward connections (Faini et al. 2018). If this hypothesis is true, one should expect PNNs to co-vary with thalamic input strength across sensory areas. To test this, we used published data from the mouse brain connectivity atlas of the Allen Institute (Oh et al. 2014) to measure thalamic input strength for all somatosensory, visual and auditory areas (total inputs from the sensory-motor related portion of the thalamus, DORsm as indicated in the CCFv3 nomenclature, see methods). Strikingly, we found that both WFA diffuse fluorescence and PNN energy were highly correlated with thalamic input strength, and this effect was most prominent in layer IV where the amount of thalamic inputs could explain respectively 59% and 49% of the variance in the two PNN metrics (r=0.77 and 0.70) (Figure 6.13). This corroborates the thalamo-cortical hypothesis and may provide a basis to investigate the role of PNNs on feed-forward functional signaling in sensory cortices.

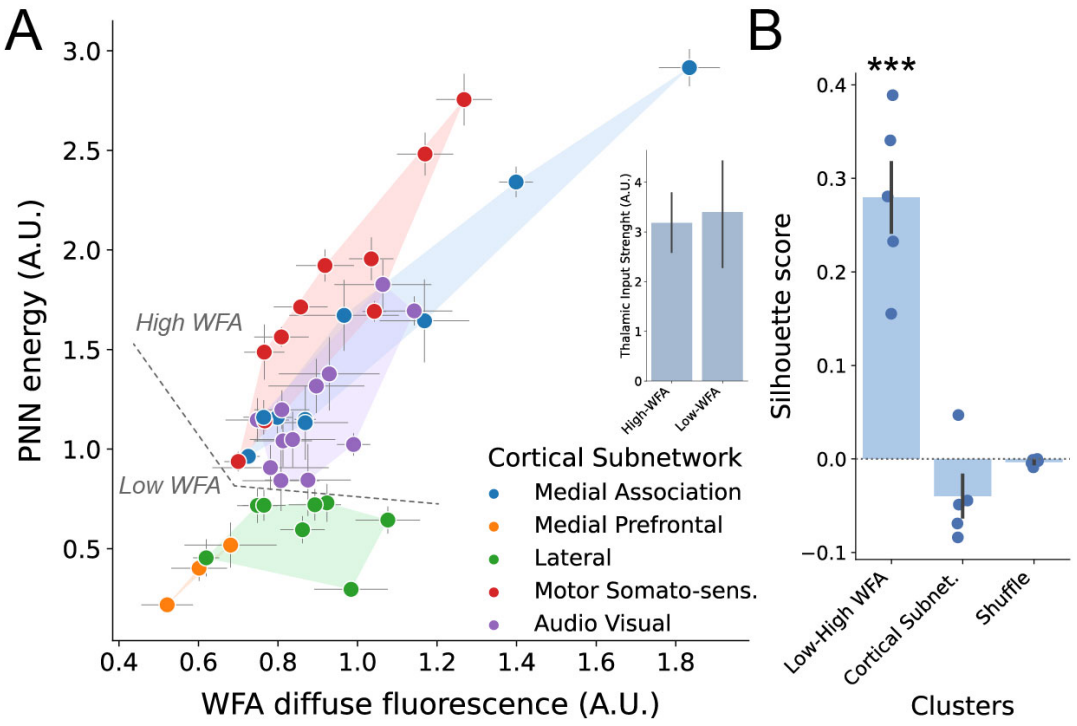

Figure 6.14: **PNN organization in cortical subnetworks. (A)** Scatterplot of all cortical areas colored by their cortical subnetwork in the 2D space of PNN energy and WFA diffuse fluorescence. The transparent shading represents the convex hull of all points in a subnetwork. Regions cluster into 2 groups: high-WFA and low-WFA. The inset shows average thalamic input strength of regions divided in high- and low-WFA groups. **(B)** Silhouette score, representing a metric for clustering quality, calculated for each mouse by grouping cortical areas in 2 groups (high- and low-WFA), 5 groups (cortical subnetworks), or 2 groups but randomly shuffled (shuffle). See Table 6.1 for statistical comparisons.

The different regions of the cerebral cortex can also be grouped in subnetworks based on their connectivity pattern within the cortex itself. Indeed, recent work clustered the

cerebral cortex in five distinct functional subnetworks (Kim et al. 2017; Zingg et al. 2014). To further explore potential principles of PNN organization, we asked whether PNNs were differentially expressed in some of these subnetworks. To do this, we plotted WFA diffuse fluorescence vs PNN energy for each cortical region. The position of each area in this space reflects the abundance of diffuse and aggregated CSPGs. We found that cortical subnetworks were clustered in two groups with no overlap. A "low-WFA" group comprising the lateral and medial prefrontal subnetworks and a "high-WFA" group comprising audio-visual, motor-somatosensory, and medial association networks (Figure 6.14A). To quantify this, we grouped brain regions with three strategies: the high/low WFA as described above, the original five cortical subnetworks, and high/low WFA regions randomly shuffled. For each grouping, we measured the silhouette score, a metric representing the separation and the quality of data clustering (Zhao et al. 2018). We found that grouping cortical regions in high- and low-WFA was the best grouping strategy (Figure 6.14B). Interestingly, the subdivision in high- and low-WFA region groups could not be explained simply by different thalamic input strength since we did not observe any significant difference in the overall thalamo-cortical connectivity between these two groups of regions in the Allen Institute dataset (Figure 6.14A, inset). Taken together, these results provide a layer-specific description of PNNs and their relationship with PV cells throughout the cortex and highlight two, potentially independent, principles that might regulate PNN organization throughout the cortex.

6.5 Gene expression correlates of PNN presence

We next asked whether there could be gene expression patterns that are correlated at brain area level with PNNs abundance in the entire brain. This might highlight molecular principles underlying PNN organization. To answer this question, we analyzed data published in the Anatomic Gene Expression Atlas (AGEA) by the Allen Institute (Lein et al. 2007). This dataset describes region-specific expression levels for about 18000 genes. For each gene, we could correlate its expression in all the brain areas with a metric for PNN staining to detect genes whose pattern of expression is predictive of PNN presence. We found about 5000 genes positively correlated, and 1000 negatively correlated with WFA (FDR<0.01, Benjamini-Hochberg, see also methods). It is important to note that this analysis reflects the average of both gene expression and PNNs at the level of brain areas and not single cells. To validate our approach, we selected a few genes known to be related to PNN structure and function: Hyaluronan and proteoglycan link protein 1 (Hapln1), coding for a link protein essential for PNNs structure (Carulli et al. 2010); hyaluronan synthase 3 (Has3), a necessary component for PNN aggregation (Kwok et al. 2010); Matrix metallopeptidase 9 (Mmp9), an enzyme known to regulate PNN and PV development (Pirbhoy et al. 2020); A disintegrin and metalloproteinase with thrombospondin motifs (Adamts5 also known as Adamts11), an aggrecan-degrading protease (Held-Feindt et al. 2006) that is expressed by PV interneurons with a PNN (Rossier et al. 2015), and parvalbumin (Pvalb). All these genes were significantly correlated with both PNN energy and WFA diffuse fluorescence (Figure 6.15A,B). Strikingly, out of 17631 genes, the gene coding for aggrecan (Acan), the major proteoglycan core protein present in PNNs (Dauth et al. 2016; Fawcett et al. 2019; Oohashi et al. 2015), was respectively the second and fifth most correlated gene with WFA diffuse fluorescence (r=0.56) and PNN energy (r=0.56).

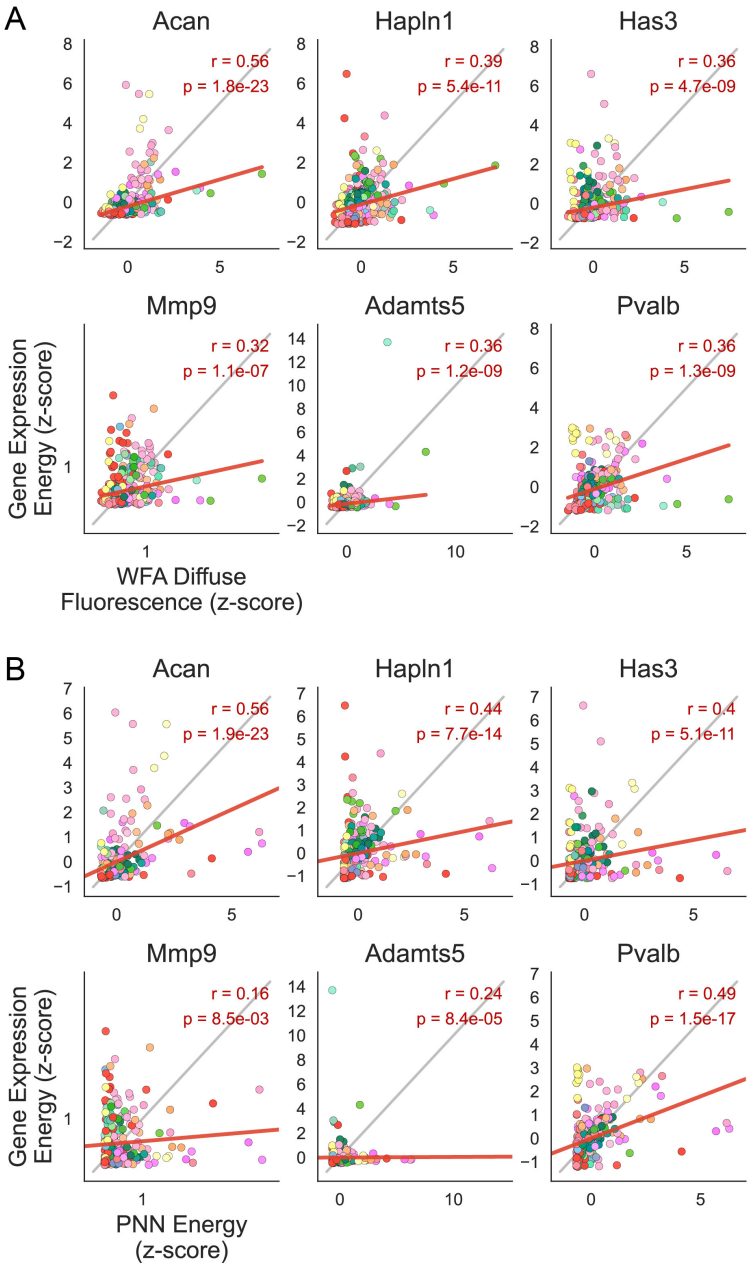

Figure 6.15: **Marker genes for PNNs. (A)** Correlation between WFA diffuse fluorescence and gene expression for six marker genes. *Acan* (aggrecan), *Hapln1* (link protein), *Has3* (Hyaluronan synthase 3), *Mmp9* (Matrix metalloprotease 9), *Adamts5* (an aggrecan-degrading protease), and *Pvalb* (parvalbumin). **(B)** Same as in A but for PNN energy.

Consistently, when we repeated this analysis for PV energy we found that the top most correlated gene was Pvalb itself (r=0.80). Other markers associated with PV neurons were also positively correlated (Figure 6.16). These included the genes encoding the fast voltage-gated potassium channels Kv3.1 and KV1.1 (Kcnc1 and Knca1) (Chow et

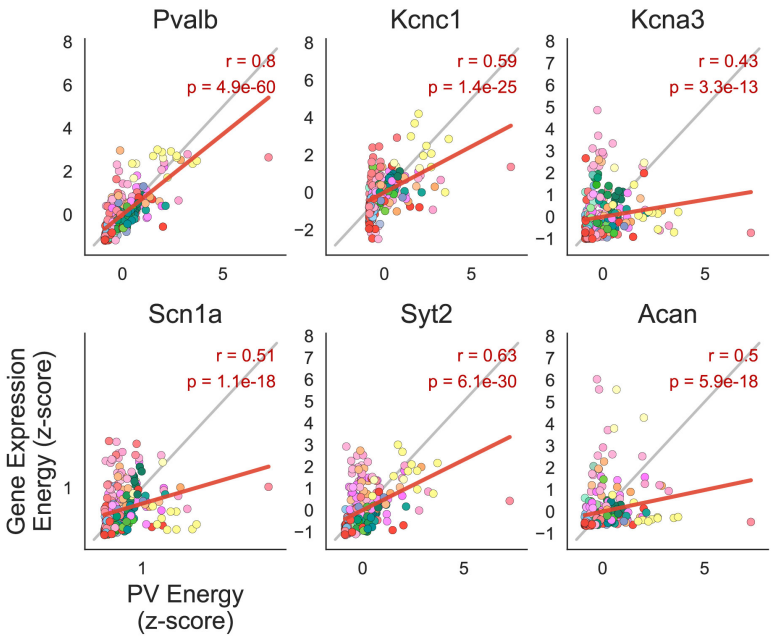

Figure 6.16: **Marker genes for PV cells.** Correlation between PV energy and gene expression for six marker genes. *Pvalb* (parvalbumin), *Kcnc1* (potassium chanel Kv3.1), *Knca1* (potassium chanel Kv1.1), *Scn1A* (sodium channel Nav1.1), *Syt2* (synaptotagmin 2), and *Acan* (aggrecan).

al. 1999; Lorincz et al. 2008), and the sodium channel Nav1.1 (Scn1A) (Ogiwara et al. 2007)); synaptotagmin 2 (Syt2), a protein that ensures fast calcium sensing and vesicle release (Bouhours et al. 2017), and aggrecan (Acan). These results validated our approach, allowing us to provide lists for positive and negatively correlated genes that might highlight molecular regulators of PNNs and may guide future studies, for example by investigating their causal relationship with PNNs in knock-out models.

To get an insight into the biological processes related to these genes we performed a gene ontology analysis on the list of the top most correlated and anticorrelated genes with PNN energy (Figure 6.17A,B). Genes related to processes of axon ensheathment, myelination, mitochondrial function, and respiration were enriched in the pool of the positively correlated. Conversely, we found that anticorrelated genes were related to processes related to synaptic plasticity involving, among the others, synaptic and dendritic spine organization. This is consistent with the known inhibitory role of PNNs toward synaptic plasticity. Finally, we performed a similar overrepresentation analysis on a smaller gene set, the matrisome (Naba et al. 2016), containing about 1000 genes related to different categories of ECM structure and function. Only the category proteoglycans was overrepresented in the set of positively correlated genes (Figure 6.17C).

Taken together, these data show that with this approach we can reliably identify gene expression correlates of PNN abundance. Such an approach, as well as the resulting gene lists, could prove useful for designing experiments to investigate the molecular biology underlying PNN development and regulation.

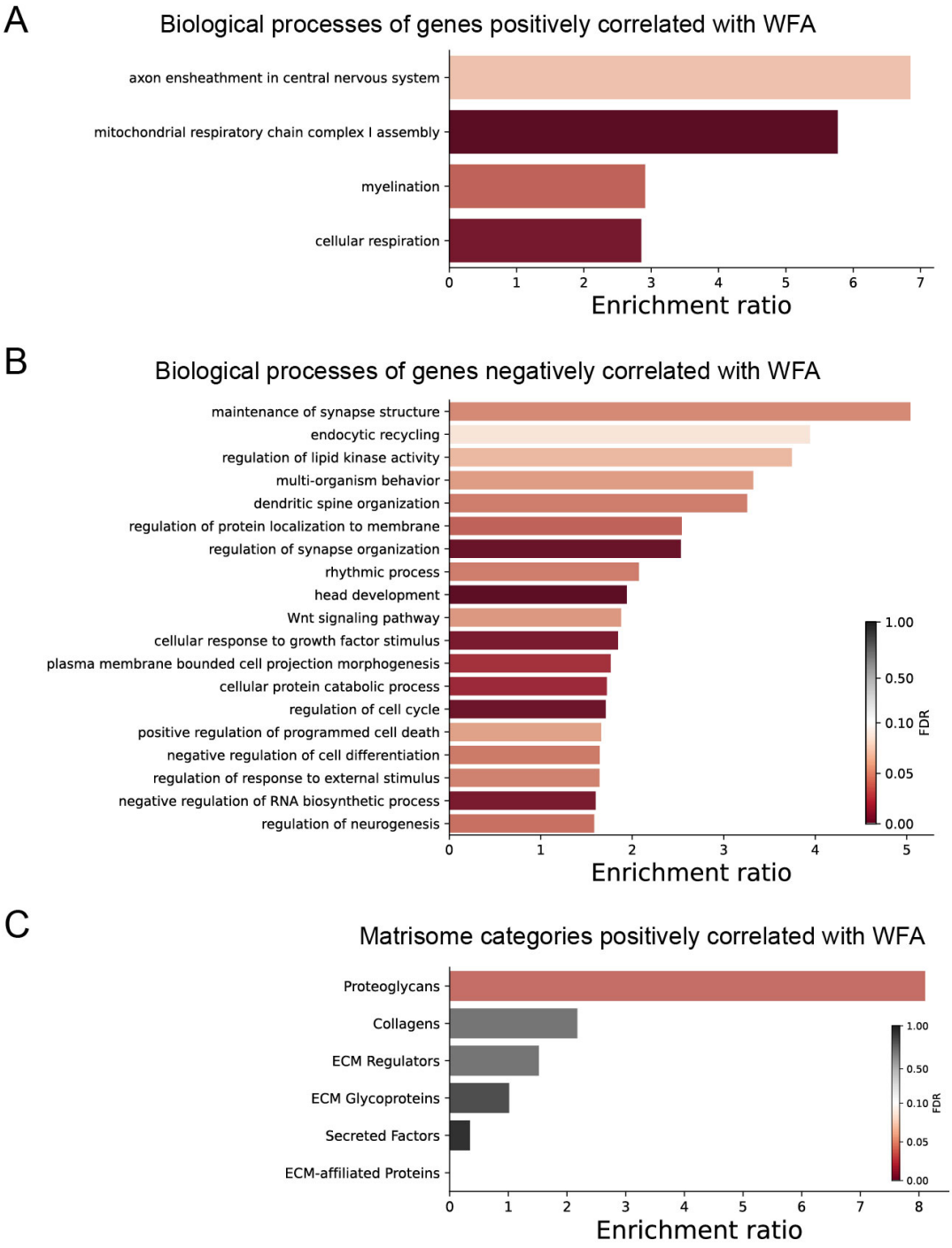

Figure 6.17: **(A)** Biological process categories enriched in genes positively correlated with PNN energy. **(B)** Biological process categories enriched in genes negatively correlated with PNN energy. **(C)** Matrisome categories of genes positively correlated with PNN energy. Bars are in descending order of enrichment ratio and colored based on the adjusted p-value with darker red shades corresponding to more significant values (threshold: FDR<0.1).

Table 6.1: **Statistical comparisons**

Fig	Description	Test	N (units)	Results
6.3A	Diffuse fluorescence differences between major brain subdivision	one-way RM ANOVA	5 mice per brain region	F(11,4)=37.69, P<0.0001
6.3A	PNN energy differences between major brain subdivision	one-way RM ANOVA	5 mice per brain region	F(11,4)=99.88, P<0.0001
6.3A	Diffuse fluorescence significantly different from 1			
	Isocortex	one sample t-test	5 (mice)	t(4)=1.32, P=0.26
	Olfactory areas	one sample t-test	5 (mice)	t(4)=13.02, P<0.001
	Hippocampal formation	one sample t-test	5 (mice)	t(4)=1.70, P=0.16
	Cortical subplate	one sample t-test	5 (mice)	t(4)=2.60, P=0.06
	Striatum	one sample t-test	5 (mice)	t(4)=9.30, P<0.001
	Pallidum	one sample t-test	5 (mice)	t(4)=3.90, P=0.018
	Thalamus	one sample t-test	5 (mice)	t(4)=6.72, P=0.003
	Hypothalamus	one sample t-test	5 (mice)	t(4)=1.57, P=0.19
	Midbrain	one sample t-test	5 (mice)	t(4)=5.19, P=0.007
	Pons	one sample t-test	5 (mice)	t(4)=3.38, P=0.028
	Medulla	one sample t-test	5 (mice)	t(4)=3.29, P=0.030
	Cerebellum	one sample t-test	5 (mice)	t(4)=22.77, P<0.001
6.3A	PNN energy significantly different from 1			
	Isocortex	one sample t-test	5 (mice)	t(4)=14.99, P=0.0001
	Olfactory areas	one sample t-test	5 (mice)	t(4)=13.19, P=0.0002
	Hippocampal formation	one sample t-test	5 (mice)	t(4)=6.337, P=0.0032
	Cortical subplate	one sample t-test	5 (mice)	t(4)=30.46, P<0.0001
	Striatum	one sample t-test	5 (mice)	t(4)=56.71, P<0.0001
	Pallidum	one sample t-test	5 (mice)	t(4)=6.194, P=0.0035
	Thalamus	one sample t-test	5 (mice)	t(4)=4.237, P=0.0133
	Hypothalamus	one sample t-test	5 (mice)	t(4)=10.87, P=0.0004
	Midbrain	one sample t-test	5 (mice)	t(4)=7.285, P=0.0019
	Pons	one sample t-test	5 (mice)	t(4)=7.291, P=0.0019
	Medulla	one sample t-test	5 (mice)	t(4)=13.21, P=0.0002
	Cerebellum	one sample t-test	5 (mice)	t(4)=23.77, P<0.0001
6.10C	Probability of having a PNN (whole brain)	one way RM ANOVA	5 per class (mice)	see figure inset
6.10D	Probability of having a PNN (major brain subdivisions)	one way RM ANOVA	5 per class (mice)	see figure inset
6.12A	Visual areas. Diffuse fluorescence comparison	two sample paired t-test	5 (mice) per group	t(8)=4.13, P=0.015

Table 6.1: **Statistical comparisons**

Fig	Description	Test	N (units)	Results
	Visual areas. PNN energy comparison	two sample paired t-test	5 (mice) per group	t(8)=7.52, P=0.0017
6.12B	Visual areas. Comparison by layer	two-way RM ANOVA	5 (mice) per group	Interaction layer * areaHierarchy F(4,32)=24.52, P<0.0001
	L1 - Primary vs Associative	Holm-Sidak	5 (mice) per group	t(8)=0.30, P=0.76
	L2/3 - Primary vs Associative	Holm-Sidak	5 (mice) per group	t(8)=1.51, P=0.26
	L4 - Primary vs Associative	Holm-Sidak	5 (mice) per group	t(8)=8.23, P<0.001
	L5 - Primary vs Associative	Holm-Sidak	5 (mice) per group	t(8)=5.09, P<0.001
	L6 - Primary vs Associative	Holm-Sidak	5 (mice) per group	t(8)=2.04, P=0.14
6.12C	Auditory areas. Diffuse fluorescence comparison	two sample paired t-test	5 (mice) per group	t(8)=4.29, P=0.013
	Auditory areas. PNN energy comparison	two sample paired t-test	5 (mice) per group	t(8)=8.01, P=0.0013
6.12D	Auditory areas. Comparison by layer	two-way RM ANOVA	5 (mice) per group	Interaction layer*areaHierarchy F(4,32)=18.09, P<0.0001
	L1 - Primary vs Associative	Holm-Sidak	5 (mice) per group	t(8)=0.40, P=0.69
	L2/3 - Primary vs Associative	Holm-Sidak	5 (mice) per group	t(8)=3.04, P=0.013
	L4 - Primary vs Associative	Holm-Sidak	5 (mice) per group	t(8)=9.84, P<0.001
	L5 - Primary vs Associative	Holm-Sidak	5 (mice) per group	t(8)=3.92, P=0.0013
	L6 - Primary vs Associative	Holm-Sidak	5 (mice) per group	t(8)=1.03, P=0.53
6.14A	(Inset) - Thalamic input strength different between high- and low-WFA cortical regions	two sample t-test	25 vs 11 (regions)	t(34)=-0.19, P=0.85
6.14B	Silhouette score comparison			
	Low-high-WFA vs Cortical Subnetworks	Holm-Sidak	5 vs 5 (mice)	t(8)=6.83, P<0.001
	Low-high-WFA vs Shuffle	Holm-Sidak	5 vs 5 (mice)	t(8)=6.93, P<0.001
	Cortical Subnetworks vs Shuffle	Holm-Sidak	5 vs 5 (mice)	t(8)=-1.59, P=0.15

7 Discussion

Here, we created and analyzed a whole brain dataset of PNNs and PV cells in the adult mouse brain. We provided several quantitative measurements for the abundance of PNNs and PV cells and their colocalization. We assembled our dataset in the common coordinate space of the Allen Institute CCFv3 in order to facilitate and encourage replication studies, and integration with other datasets. As a consequence, we could analyze our PNN data together with publicly available connectomics (Oh et al. 2014; Zingg et al. 2014) and gene expression (Lein et al. 2007) datasets. This allowed us to highlight potential principles of PNN organization that may explain their biological function, and to identify gene expression profiles that are correlated or anti-correlated with PNN abundance. These resources will help to generate novel hypotheses, highlight interesting questions, and design experiments to better understand the function of PNNs and their implication in pathological conditions.

In the interpretation of our results it is important to note that we used WFA as a marker for PNNs. Despite it being a widely used method for PNN visualization in the literature (Fawcett et al. 2019), some structures of aggregated CSPGs are not bound by WFA, and are instead revealed by antibodies against different proteoglycans (Ariza et al. 2018; Galtrey et al. 2008; Matthews et al. 2002; Ueno et al. 2018). It is thus possible that WFA-negative nets might have a different distribution, regulation, and relationship with PV cells. Whether ECM aggregations with different CSPGs composition share the same spatial distribution or are selectively enriched in different areas is an intriguing question that may be addressed by future works. Furthermore, PV-positive neurons comprise two morphologically and functionally distinct cellular subtypes: basket cells and chandelier cells (Tremblay et al. 2016). Since both express parvalbumin, another limitation of our approach is that we could not disambiguate between the two. Finally, it should be noted that values for cell density (cells per mm2) in our dataset can be influenced by tissue shrinkage during the staining procedure. For this reason, caution should be used if comparing absolute, not normalized, numbers with other staining techniques like two-photon serial tomography in transgenic animals or light-sheet microscopy in cleared tissue. Nevertheless, assuming the possible tissue shrinkage is uniform in the entire brain, the relative distribution of cell densities between areas is expected to maintain the same profile across different methods.

7.1 Brain distribution of PNNs and PV cells

Most of the mouse brain contains cells with PNNs. In this work, we generated quantitative measurements of PNNs and WFA diffuse fluorescence for more than 600 different brain regions. While most PNN research involves telencephalic and diencephalic structures, a surprising result of our analysis is that PNNs are massively upregulated in the midbrain and hindbrain (pons and medulla) compared to the rest of the brain. These areas are essential for key vital processes like heartbeat and breathing control, basic reflexes, and

sleep, however, the role of PNNs in the neuronal circuits underlying these functions is almost unexplored. Another interesting finding is that CSPGs aggregation in PNNs might be a process that is differentially regulated across areas. Indeed, although in most of the brain the total amount of CSPGs (diffuse fluorescence) was a great predictor of the presence of aggregated PNNs (PNN energy), some areas showed no relationship between the two metrics. In particular, all areas related to olfaction had very intense diffuse staining but contained very few and thin PNNs as previously reported (Hunyadi et al. 2020), indicating that the high amount of CSPGs present in these areas did not aggregate in PNNs. An analogous, but weaker trend was also present in the cortical subplate. What are the regulatory mechanisms and the functional implications of this pattern remains to be investigated. A commonly observed property of PNNs is that they preferentially aggregate around GABAergic PV-positive interneurons (Fawcett et al. 2019). We measured this relationship across the entire brain and found that, on average, this was the case for 50% of PNNs in the entire brain, a much higher percentage than expected from chance. Moreover, across the whole brain, both PNN metrics were correlated with PV energy. Despite this clear association, our study unveils that half of the perineuronal nets in the brain do not surround PV neurons, leaving the still unanswered question of whether they might serve to regulate different circuit properties. The link between PNNs and PV cells also varied between brain subdivisions with the most striking pattern in the isocortex. Here, 70% of all PNNs were around PV cells and half of all PV cells had a net. This intimate association was also evident in the relation between staining metrics. Indeed, cortical areas had an extremely tight (r=0.92) correlation between PNN and PV energy. Given that parvalbumin neurons differentiate before birth (Fishell 2008) and PNNs aggregate much later during postnatal development (Reichelt et al. 2019), this association tells us that expressing parvalbumin drastically increases the probability to develop a net. In addition, we also found that in the isocortex, hippocampal formation, and striatum, higher PV expression levels strongly increased this probability. Intriguingly, in all three of these brain regions, PV cells have been divided, based on their intensity, in two distinct subpopulations of early-born high-PV cells and late-born low-PV cells with different roles in plasticity and learning (Donato et al. 2013; Donato et al. 2015). Our data are consistent with the interpretation that PNNs might aggregate more onto early-born high-PV neurons and that their presence could contribute to the inhibitory role of this subpopulation toward plasticity. Finally, we discovered that PNNs also show a clearly bimodal distribution of intensity raising the possibility that high- and low-WFA PNNs could represent two kinds of PNNs with potentially different functions.

7.2 Connectivity patterns predict PNN distribution in the cerebral cortex

During postnatal development, only specific regions and cell types are enwrapped in a perineuronal net. What is the functional role of PNNs in such structures, however, is still poorly understood. By analyzing their distribution in the cortex, we saw that PNNs are particularly enriched in layer IV of the primary somatosensory, visual, and auditory cortices and that their abundance correlates with the amount of thalamic input strength across all sensory areas. This specific enrichment in primary cortices was also revealed by comparing the labeling of primary versus associative cortices for each sensory

modality with the exception of the primary versus supplementary somatosensory (SSs) cortex where the associative area SSs was also strongly expressing PNNs. Recent findings show that layer IV of secondary somatosensory areas receives strong inputs from the posterior medial thalamus carrying whisker-selective sensory information (El-Boustani et al. 2020). Therefore, this observation confirms the correlation between strong thalamic input and high PNN levels. A functional relevance of this correlation is suggested by studies performed in the mouse primary visual cortex showing that PNNs can selectively control thalamic excitation onto PV cells (Faini et al. 2018). Our data raise the hypothesis that the control of feed-forward thalamo-cortical inputs on PV neurons might be one of the main functional principles that guide PNN organization throughout the entire cortex.

Another peculiar finding, is that the retrosplenial cortex (RSP), a highly associative area (Vann et al. 2009), showed overall the highest expression of PNNs among all regions of the isocortex. This particularly stands out, as the connectivity pattern of the RSP is that of a major information hub, having bidirectional connections with cingulate and visual cortices as well as with the hippocampal formation and the anterior nuclei of the thalamus (Van Groen et al. 2003). Indeed, RSP has been implicated in spatial navigation and episodic memory also in humans (Vann et al. 2009). Intriguingly, RSP is part of the "medial association" cortical subnetwork that is characterized by a very high PNN energy and WFA diffuse fluorescence raising the possibility that a second principle of organization of PNN expression, and possibly a different function, underlies this pattern of expression. Despite these intriguing features, PNN function in this region has not been investigated yet. Recently, it has been reported that PNNs in the RSP are downregulated in a mouse model of schizophrenia (Klimczak et al. 2021), raising the possibility that this line of research might have clinical implications for neuropsychiatric disorders (Browne et al. 2022).

7.3 Gene expression correlates of PNNs

Although the molecular components of PNNs are at least in part understood, the mechanisms by which they are regulated and the biological processes that they affect are still a very active area of research. Indications about the gene expression profiles are often of great help in dissecting regulation and function of cell types. However the search for a gene expression signature of PNN enwrapped cells is hampered by the facts that PNNs are extracellular multimolecular structures, and that there are currently no means to tag the PNN positive neurons. To try to overcome this problem, we performed a correlational analysis between the AGEA dataset by the Allen Institute (Lein et al. 2007) and PNN expression. This approach was validated by the overrepresentation analysis on the matrisome gene set, which showed that PNN-correlated genes are remarkably enriched in the proteoglycan category, and by finding key constituents of the PNN ranking in the top positions of the list of the genes positively correlated with PNN energy. However, this approach also revealed many other genes with positive and negative correlations with PNNs. In particular, gene ontology analysis showed that categories related to synaptic function and synaptic plasticity were significantly downregulated in brain areas enriched with PNNs. Furthermore, PNNs are correlated with myelin genes, another set of plasticity brakes (Bonetto et al. 2021; Faria et al. 2021; Monje 2018). These results are in agreement with previous studies suggesting that PNNs represent plasticity brakes appearing at the

end of brain critical periods.

It must be noted that both the gene expression and PNN/PV abundance data are expressed as region averages and not single cell measurements. Moreover, such correlations are causally-neutral. For each gene, a correlation could imply that it participates in the formation of PNNs, that it is expressed as a result of PNN abundance, or that its expression and PNNs are simply regulated by a common factor. Nevertheless, mining these lists could reveal potential candidate genes for gain- or loss-of-function studies to probe causal relationships.

Our work also represents a unique approach based on comparing very large scale, (preferentially brain-wide) datasets of cellular structures with public datasets to extrapolate gene expression correlates, validated by well-known markers. This approach has the advantage, typical of -omics techniques, of being unbiased and data-driven, and it could also be employed in the study of many other extracellular matrix components. We envision that the advent of spatial transcriptomics will boost this type of approach.

8 Methods

8.1 Mice handling

A total of 5 adult C57BL/6J male and female mice, at approximately postnatal day (P)120 were used in this study. Weaning was performed at P21–23. Animals were maintained in rooms at 22°C with a standard 12-h light-dark cycle. During the light phase, a constant illumination below 40 lux from fluorescent lamps was provided. Mice were housed in conventional cages (365 x 207 x 140 mm, 2-3 animals per cage) with nesting material, and had access to food and water ad libitum. Mice were fed a standard diet (standard diet Mucedola 4RF25).

8.2 Immunofluorescence staining

Mice were anesthetized with chloral hydrate (20 ml/Kg BW) and perfused via intracardiac infusion with cold PBS and then 4% paraformaldehyde (PFA, w/vol, dissolved in 0.1 M phosphate buffer, pH 7.4). Brains were extracted and post-fixed overnight in PFA 4% at 4°C, then transferred to a 30% (w/vol) sucrose solution for 48 hours. For each brain, 50 µm coronal sections, spanning from the anteriormost part of the cerebral cortex to the cerebellum, were cut on a freezing microtome (Leica). One out of every 3 sections was collected for further processing, leading to a sampling of one slice every 150µm. For a small subset of sections that did not match our quality standards due to deformations during the cutting process (on average 3.7±0.5 slices per animal), an adjacent section was collected instead. For each animal, slices were assigned a unique ID and pooled in 9-10 wells of a 24-well plate for free-floating staining. Each well contained 5-6 sections that sampled the brain at equally spaced points in the anterior-posterior axis.

Slices were blocked for 2h at room temperature (RT) in a solution containing 3% bovine serum albumin (BSA, A7906 Sigma-Aldrich) in PBS. Then, slices were incubated overnight at 4°C with a solution containing biotinylated Wisteria floribunda Lectin (WFA, B-1355-2, Vector Laboratories, 1:200) and 3% BSA in PBS. On the following day, sections were rinsed 3 times in PBS (10 min each) at RT, incubated with a solution of red fluorescent streptavidin (Streptavidin, Alexa Fluor™ 555 conjugate, S21381, Thermo Fisher) and 3% BSA in PBS for 2h at RT, and rinsed again 3 times in PBS. On the same day, slices were incubated with a blocking solution for parvalbumin staining containing 10% BSA and 0.3% Triton in PBS for 30 minutes, then washed 3 times (10min each) and finally incubated overnight at 4°C with primary antibody solution containing anti-parvalbumin (Parvalbumin antibody, 195004, Synaptic System 1:1000) 1% BSA and 0.1% Triton in PBS. Then, sections were rinsed 3 times (10 min each) in PBS; incubated with a secondary antibody solution containing secondary antibody (anti-Guinea Pig IgG Alexa Fluor™ 488, A11073, Invitrogen, 1:500), 1% BSA. plus 0.1% Triton for 2h at RT, and washed again 3 times in PBS. Finally, sections were mounted on microscopy slides with a mounting

medium (VECTASHIELD® antifade mounting medium, H-100, Vector Laboratories), and stored at 4°C. All sections in each staining well were mounted on the same slide.

8.3 Image acquisition

All images were acquired using the acquisition software ZEN blue with a Zeiss Apotome.2 microscope and a 10x objective and digitized by an AxioCam MR R3 12-bit camera, resulting in a pixel size of 0.645µm. For the WFA channel, excitation light passed through a 538-562nm bandpass filter and a 570nm dichroic mirror, while emitted light was filtered with a 570-640nm bandpass filter. For the PV channel, filters were a 450-490nm bandpass for excitation, a 495nm dichroic mirror, and a 500-550nm bandpass for emission. All images were acquired with the same intensity of excitation light and with an exposure time of 80ms for the WFA channel and 850ms for the PV channel. For all sections, we acquired 3 apotome images for optical sectioning. Each brain slice was acquired as a tiled multi-image experiment on a single z-plane. Coronal sections of the entire mouse brain span a relatively large area and even small irregularities in the microscope slide can lead to artifacts in image intensity due to the tissue section not sitting exactly perpendicular to the optical path. To account for this, we acquired each slice with a tilted z-plane linearly interpolated between 4 manually selected focus points at the edges of each section. After the acquisition, multi-image tiles were stitched in ZEN and exported as 8-bit TIFF files for further processing. The resulting dataset consisted of 582 2-channel, 8-bit, TIFF images ranging from 15 to 250MB in size and from 2646 to 17631px (width) in resolution.

8.4 Image registration to the Allen Brain Atlas CCFv3

8.4.1 Image Preprocessing

For each mouse, all the images were ordered along the anterior-posterior axis according to their unique ID. Images were manually inspected and, based on irregularities in the fixed brain and anatomical landmarks, a minority of them were mirrored vertically to make sure matching hemispheres were always on the same side for the whole image sequence.

All the following steps of preprocessing and image registration were carried out on a downsampled (20% of the original size) TIFF dataset. For each downsampled experimental image, we created a matching binary mask of the same size, encoding whether each pixel belongs to brain tissue or not. Masks were automatically generated for the entire subsampled dataset by using a machine learning model (random decision forest) interactively trained with Ilastik (Berg et al., 2019) on a subset of 57 image crops (width ranging from 344px to 526px). Masks were used in the quantification steps to restrict fluorescence analysis only to portions of the images that contained biological tissue. All the masks were visually inspected through a custom MATLAB graphical user interface (GUI) and, if necessary, manually adjusted to correct for misclassification of small areas or to exclude parts of the tissue containing experimental artifacts from further analysis.

8.4.2 Image Registration

We aligned our dataset to the Allen Mouse Brain Common Coordinate Framework (CCFv3) (Q. Wang et al. 2020) with a multi-step workflow: first, we used the software QuickNII

v2.2 (Puchades et al. 2019) to interactively assign each experimental image to a specific plane in the reference atlas based on anatomical landmarks. The software allows the selection of an arbitrary 2D plane out of the CCFv3 volume, thus improving accuracy for samples where sections were not cut on a perfectly coronal plane, but with a slight angle. In the same software, we also performed rigid transformations (i.e., rotations and translations) and uniform horizontal or vertical stretch in order to match the reference plane to each experimental image. In a second step, we used the software VisuAlign v0.9 (RRID: SCR_017978, https://www.nitrc.org/projects/visualign/) to manually apply local, non-rigid transformations to the planes selected in QuickNII in order to match the experimental images. We then used a custom set of MATLAB functions to load the output file from VisuAlign and to generate a displacement field for each experimental image. Each displacement field defines the local non-rigid transformation as a couple of values (Dx, Dy) for each pixel, defining the displacement in the image on the X and Y axes. By using the coordinates of the 2D plane defined in QuickNII and the local transformations defined in the displacement field it is possible to match each pixel position in our experimental images (Xe, Ye) to a voxel position in the reference atlas (Xa, Ya, Za).

8.5 Deep learning models for cell counting

The deep learning models used in this work are based on a novel counting strategy described in (Ciampi et al. 2022) specifically designed to account for the variability between experimenters when counting non-trivial, overlapping, or low-contrast objects like PNNs in histological preparations. Briefly, cell counting for both PNNs and PV cells was done through a two-step pipeline. In the first step, we performed cell detection by using the Faster-RCNN network (Ren et al. 2015) with a Feature Pyramid Network module and a ResNet-50 backbone. The goal of this stage is to produce a collection of putative object locations. The training dataset of this network is large but labeled by a single rater, thus it is assumed to be "weakly labeled", i.e., it may contain spurious (false positives) and missing annotations (false negatives). In the second step, we scored each detected object to assign it an "objectness" value designed to maximize its correlation with the raters' agreement. To do this, we trained a small convolutional network to perform ordinal regression, i.e., producing increasing scores for objects with increasing raters' agreement.

As a result of this strategy, we employed four different models: a localization model for PNNs and PV cells, and a scoring model for PNNs and PV cells. From now on, we will refer to these models respectively as PNN_{loc}, PV_{loc}, PNN_{score}, and PV_{score}.

8.5.1 Training datasets

Here we describe the training dataset used for each model. The dataset used for the PNNloc model consists of 580 8-bit grayscale TIFF images (width ranging from 2646 to 17631px) dot-annotated with the (x,y) position of each PNN for a total of 678556 PNNs. The dataset used for the PVloc model consists of 53 8-bit grayscale TIFF images (width ranging from 5157 to 16389px) dot-annotated with the (x,y) position of each cell for a total of 101348 PV cells. PNNs were annotated by looking for distinctive circular patterns of WFA staining around cell somata and proximal dendrites. Finer PNN-like structures exclusively present in the neuropil, like those found in the olfactory bulbs (Hunyadi et al.

2020), were not annotated in our training dataset due to the magnification factor in our images not allowing for consistent detection of such structures.

The datasets used for the two scoring models both consist of a collection of 25 8-bit grayscale TIFF images (2000 x 2000 px). Seven expert experimenters independently dot-annotated each image for a total of 4727 PNNs and 5833 PV cells that vary in agreement between raters from 1/7 to 7/7.

8.6 Measurement of single-cell staining intensity

Quantification of the staining intensity of individual cells (PNNs or PV cells) was performed on 80x80 pixels image tiles centered on the (x,y) center positions of each PNN/cell. Within each tile, we segmented pixels belonging to the cell or the background, and the intensity of each PNN/cell was defined as the average value of the pixels belonging to that cell. The segmentation was performed by using a random forest pixel classifier implemented with the MATLAB Treebagger class with the support of additional custom MATLAB functions (Cicconet et al. 2019). This approach allows the classification of single pixels as background or foreground, based on a collection of features of that pixel. Classifying all the pixels in an image tile results in a binary segmentation mask. The features considered for pixel classification were the contrast-adjusted pixel intensity (using the imadjust MATLAB function), the position of the pixel relative to the center of the tile in the horizontal and vertical axes, and the pixel intensity in 16 versions of the image tile filtered with 16 Gabor filters. The wavelength and orientation of each Gabor represented one of the possible combinations of four different wavelength values (2.8, 5.6, 11.3, 22.6 pixels/cycle) and four different orientations (0°, 45°, 90°, 135°). Wavelengths were sampled in increasing powers of 2 starting from 4/sqrt(2) up to the hypotenuse length of the input image tile, while orientations were sampled from 0° to 135° with a step of 45° (Jaini et al. 1991). Each random forest model for segmentation of PNNs and PV cells was trained on 69600 pixels from 1160 tiles (60 pixels randomly chosen for each tile).

8.7 Data analysis

All data analysis was done using custom software written in MATLAB 2021b and Python (3.7 and 3.8). We used the following additional Python libraries for data analysis: NumPy (1.19.2) (Harris et al. 2020), Pandas (1.3.5) (McKinney 2010), Scikit-learn (0.24.1) (Pedregosa et al. 2011) and SciPy (1.7.3) (Virtanen et al. 2020).

8.7.1 Staining metrics definition

We defined four metrics to quantitatively analyze the staining for PNNs and PV cells. First, *diffuse fluorescence* represents the amount of average fluorescence signal in a brain region. It is defined as the average intensity of all the pixels belonging to that region across all the slices of each mouse. These values are then normalized within each mouse by dividing them by the mean pixel intensity of all the regions. This normalization removes global differences in intensity between mice (due to for example perfusion quality and post-fixation) while highlighting how staining intensity is differentially distributed across brain regions. As a result, a region with diffuse fluorescence of 1 would have a staining

intensity equal to the brain average. Second, *density* represents the number of cells or PNNs per unit of area in a brain region. It is defined as the total number of cells or PNNs belonging to that region across all the slices of each mouse, divided by the total area belonging to that region in mm2. Third, *cell intensity* represents the staining intensity of cells or PNNs in a brain region. Each cell is assigned a value of staining intensity (see section "Measurement of single-cell staining intensity"). For each region, cell intensity is defined as the average intensity of all the cells belonging to that region. These values are then normalized to the range 0-1 by dividing by 255 (maximum intensity value for 8-bit images). Last, we define a combined, more abstract metric, that takes into account both the number and the intensity of cells/PNNs, called *energy*. Cell energy can be thought of as a measure of cell density, weighted on intensity. For each region, energy is defined as the sum of the cell intensity of all the cells in that region, divided by the total surface area. For a region of area A containing c cells each with intensity Int:

$$Energy = \frac{\sum_{i=1}^{c} Int_i}{A} \tag{8.1}$$

These values are then normalized within each mouse by dividing them by energy calculated on the entire brain. As a result, a region with an energy value of 1 would be equal to the brain's average energy. This definition of energy is analogous to the one used in (Lein et al. 2007) for the analysis of in-situ hybridization data (see the technical paper on the informatics data processing here help.brain-map.org/display/mousebrain/Documentation). It is important to note that the brain of each mouse in this study has been sampled in its entire anterior-posterior axis with the same sampling rate (1 every 3 slices) thus ensuring that the normalization step for diffuse fluorescence and energy measurements does not introduce biases due to differential sampling of areas with extreme staining intensity values.

8.7.2 Brain structure sets

Throughout the paper we aggregated data in three sets of brain structures differing by their level of spatial resolution. The first structure set ($structure_set_id$: 687527670) has a low level of resolution and is composed of 12 coarse-ontology major brain divisions (see Table 1). The second structure set ($structure_set_id$: 167587189) has a medium level of resolution (e.g., it comprises distinct cortical areas) and is composed of 316 mid-ontology brain regions (see Table 3). These two structure sets were defined by the Allen Institute in their API (https://allensdk.readthedocs.io/en/latest/install.html) and can be accessed using the StructureTree object. Lastly, for the analysis of cortical layers, we maintained the finest level of resolution present in the CCFv3, where individual cortical layers are segmented. Please note that, for the visualizations in Figure 6.11, we included the lateral and medial parts of the entorhinal cortex (ENTl and ENTm, belonging to the hippocampal formation) given their layered structure. For all the analyses in the paper, we dropped data of any structure belonging to or descending from the fiber tracts (areaID:1009) and the ventricular system (areaID:73).

8.7.3 Colocalization PNN-PV

PV cells and PNNs were counted with two distinct neural networks on separate channels. We defined a PNN and a PV cell to be colocalized based on their (x,y) position in the

original image using the following criteria. We selected one cell/PNN at a time as a reference object. For each reference object, we selected only objects in the other channel with a distance equal to or smaller than 15 pixels (9.675 µm). If multiple objects satisfied this criterion, we picked the closest one as a colocalized object. Otherwise, if no objects were close enough to the reference one, we defined the reference object as non-colocalized (either a PV-negative PNN or a WFA-negative PV cell). We computed two metrics to describe PNNs and PV colocalization: first, the percentage of PV+ PNNs, that is the fraction of PNNs that are around a PV-positive cell; second, the percentage of WFA+ PV cells, that is the fraction of PV-positive cells that are surrounded by a net.

Colocalization metrics at the coarse level of resolution (see Brain structure sets for definition) were calculated independently for each mouse and the results averaged across mice. For the same analysis at higher levels of resolution (mid-ontology in Figure 6.8, or cortical layers in Figure 6.11), we adopted a different strategy. At higher resolutions, brain subdivisions are much smaller and some areas contain a limited, if any, number of PNN/PV-cells (e.g., layer 1 of cortical areas). As a result, the % of colocalization can vary dramatically depending on a few, or even a single cell, thus not providing a robust measure for that area (e.g., an area with 3 PV+ cells can vary from 0% to 100% depending on the state of PNNs on only 3 neurons). To solve this issue, we calculated colocalization metrics on a dataset of cells pooled from all animals except one in a manner similar to the leave-one-out cross-validation approach used in machine learning (Wong 2015). We repeated this process for all mice and considered each repetition an experimental unit. We then averaged across experimental units. For the analysis of PV+ PNNs (Figure 6.8 left side and Figure 6.11 bottom), we included only brain regions in which there was at least 1 PNN in at least 2 mice. For the analysis of WFA+ PV cells (Figure 6.8 right side), we included only brain regions in which there was at least 1 PV cell in at least 2 mice.

8.7.4 PV intensity classes

PV cells were divided in four intensity classes of equal width based on their cell intensity levels. The classes were defined as 1: low PV [0, 0.25]; 2: intermediate-low PV [0.25, 0.5]; 3: intermediate-high PV [0.5, 0.75]; 4: high PV [0.75, 1]. The probability of being surrounded by a net was estimated by dividing the number of colocalized PV-PNN cells by the total number of PV cells in that class. This analysis was done independently for each mouse. We fit data to a first-degree linear equation by using the numpy function np.polyfit. The estimated first- and zero-order parameters are displayed in the text insets for each plot.

8.7.5 Correlation analysis

The analysis of correlations in all the figures was done by computing the Spearman's rank correlation coefficient using the SciPy function stats.spearmanr. In each graph, we reported the value of the correlation coefficient and the associated p-value. We highlighted in red significant ($p<0.05$) correlations.

8.7.6 Correlation with thalamic afferent connectivity

To measure thalamic input strength we used connectomics data from the Allen Institute (Oh et al., 2014). In that dataset, we selected the connections that originated from the

sensory-motor cortex related part of the thalamus (DORsm, area ID: 864, according to the CCFv3 nomenclature, https://atlas.brain-map.org/) and that terminated in sensory-related cortical regions (SSp-n, SSp-bfd, SSp-ll, SSp-m, SSp-ul, SSp-tr, SSp-un, SSs, VISal, VISam, VISl, VISp, VISpl, VISpm, VISli, VISpor, AUDd, AUDp, AUDpo, AUDv). Input strength for each cortical area was measured as the sum of connection strength from all brain regions belonging to the DORsm to the ipsilateral and contralateral parts of that cortex. To uniform the scale of PNN measurements and thalamic connectivity, we z-scored each set of data. For the correlation analysis (Figure 6.13), we computed Spearman's rank correlation coefficient and the associated p-values. To estimate connection strength in high-WFA and low-WFA region clusters, we averaged thalamic input strength values, obtained in the same way, of all the areas in each cluster.

8.7.7 Correlation with gene expression and gene set overrepresentation analysis

We correlated the distribution of PNN energy, WFA diffuse fluorescence and PV energy with the pattern of expression of approximately 18000 genes, published in the Anatomic Gene Expression Atlas (AGEA) by the Allen Institute (Lein et al. 2007). In this dataset, levels of expression of each gene are derived from the signal intensity of whole-brain in situ hybridization essays and quantified as expression energy, a metric defined in an analogous way to PNN and PV energy. For correlation analysis, both gene expression data and PNN/PV staining parameters were expressed at mid-ontology resolution (see Table 3). The five areas showing largest standard deviation in PNN/PV staining metrics were excluded from the analysis. We computed the Spearman's rank correlation coefficient between each of the 3 staining metrics and the pattern of expression of each of the AGEA genes. The associated p-values were then corrected for multiple testing with Benjamini-Hochberg method. For all the analyses we considered genes with an adjusted p-value <0.01 as significantly correlated (if Spearman's correlation coefficient was positive) or anticorrelated (if Spearman's correlation coefficient was negative) with the staining metric considered.

For the genes correlated and anticorrelated with PNN energy and WFA fluorescence, we performed gene ontology analysis using WebGestalt platform (B. Zhang et al. 2005). Overrepresentation of gene ontology terms (biological process domain) was tested separately for the 1000 genes most correlated (with largest correlation coefficient) and the 1000 genes most anticorrelated (with most negative correlation coefficient) with each of the two metrics. The list of all the genes present in the AGEA was used as the background for all the analyses. Overrepresented gene ontology terms were filtered to ensure a false discovery rate <0.1 (Benjamini-Hochberg method) and clustered via affinity propagation to reduce redundancy.

We then tested for overrepresentation of gene sets related to ECM biology, defined by (Naba et al. 2016) as matrisome categories, in the 200 genes most correlated with PNN energy. As for gene ontology, the entire list of genes of the AGEA was used as the background. To assess statistical significance, Fisher's exact test was performed as implemented in the SciPy function stats.fisher_exact and p-values were corrected for multiple testing using Benjamini-Hochberg method. For each matrisome category, the enrichment ratio was calculated as the number of genes observed in both the matrisome category and the 200-gene list divided by the number of genes expected assuming independence of the

matrisome set and the gene list.

8.8 Data visualization

Data visualization for all the figures was done in Python (3.7 and 3.8). Heatmaps, bar plots, and scatterplots were created using the libraries Seaborn (0.11.0) (Waskom 2021) and Matplotlib (Hunter 2007). Rendered heatmaps of coronal brain slices were done by using BrainRender (Claudi et al. 2021) and bg-heatmaps (Claudi et al. 2022).

Part III

Visual cortical function and plasticity in a mouse model of CDKL5 deficiency disorder

9 Introduction

This part represents three research projects. I co-first-authored two of them (Mazziotti et al. 2017) and (Lupori et al. 2019), while i was a co-author for the third one (Trazzi et al. 2018). All these data have been published in Human Molecular Genetics. The full articles are available at these links:

- Searching for biomarkers of CDKL5 disorder: early-onset visual impairment in CDKL5 mutant mice.
- Site-specific abnormalities in the visual system of a mouse model of CDKL5 deficiency disorder.
- CDKL5 protein substitution therapy rescues neurological phenotypes of a mouse model of CDKL5 disorder.

9.1 Summary

CDKL5 deficiency disorder (CDD) is a neurodevelopmental disorder still without a cure. Murine models of CDKL5 disorder have been recently generated raising the possibility of preclinical testing of treatments. However, unbiased, quantitative biomarkers of high translational value to monitor brain function are still missing. Moreover, the analysis of treatment is hindered by the challenge of repeatedly and non-invasively testing neuronal function.

We analyzed the development of visual responses in a mouse model of CDKL5 disorder to introduce visually evoked responses as a quantitative method to assess cortical circuit function. Cortical visual responses were assessed in CDKL5 null male mice, heterozygous females, and their respective control wild-type littermates by repeated transcranial optical imaging from P27 until P32. No difference between wild-type and mutant mice was present at P25-P26 whereas defective responses appeared from P27-P28 both in heterozygous and homozygous CDKL5 mutant mice. These results were confirmed by visually evoked potentials (VEPs) recorded from the visual cortex of a different cohort.

The previously imaged mice were also analyzed at P60–80 using VEPs, revealing a persistent reduction of response amplitude, reduced visual acuity and defective contrast function. The level of adult impairment was significantly correlated with the reduction in visual responses observed during development. Support vector machine showed that multi-dimensional visual assessment can be used to automatically classify mutant and wt mice with high reliability.

Using a conditional CDKL5 knockout model, we showed that selective cortical deletion of CDKL5 from excitatory cells is sufficient to produce abnormalities of visual cortical responses, demonstrating that the normal function of cortical circuits is dependent on CDKL5. Finally, we tested the usefulness of measuring visual cortical responses as a biomarker in a preclinical setting of drug testing. We found that cortical responses were

ameliorated by a protein substitution therapy in parallel with other hallmarks of the disease.

Thus, monitoring visual responses represents a promising biomarker for preclinical and clinical studies on CDKL5 disorder.

9.2 Introduction to the project

Cyclin-dependent kinase-like 5 (CDKL5) disorder, also known as early infantile epileptic encephalopathy type 2 (EIEE2, OMIM number: 300672) or CDKL5 deficiency disorder (CDD), is a severe neurological condition characterized by early-onset seizures in the first month of life, intellectual disability, motor and social impairment. This disease has recently been considered as an autonomous etiopathological entity (Fehr et al. 2013), with a clearly distinct genetic and clinical phenotype respect to other similar infantile encephalopathies such as Rett syndrome (RTT) and X-linked infantile spasm syndrome 1 (ISSX1). No effective treatment is currently available for this disease.

At a molecular level, CDKL5 is a serine/threonine kinase that is highly expressed in the central nervous system. Intracellular localization of CDKL5 appears to vary in different brain areas and during development with expression present both in the cytosolic and nuclear fractions (Rusconi et al. 2008). CDKL5 was also found to be localized in postsynaptic structures, where it can regulate dendritic spine maturation and density, and modulate excitatory synaptic function (Ricciardi et al. 2012; Della Sala et al. 2016). The synaptic localization of CDKL5 seems to be mediated by its interaction with the palmitoylated form of postsynaptic density protein 95 (PSD-95) (Zhu et al. 2013; Y. Zhang et al. 2014) or by the formation of a complex involving PSD-95 and NGL-1 (Ricciardi et al. 2012). In mice, CDKL5 is strongly upregulated postnatally with high levels of expression in the forebrain (Rusconi et al. 2008; Chen et al. 2010; Hector et al. 2016).

Recently, CDKL5 loss-of-function murine models that recapitulate some aspects of the human disease have become available (Amendola et al. 2014; I.-T. J. Wang et al. 2012), raising the possibility of preclinical testing of treatments. However, unbiased, quantitative biomarkers of high translational value to monitor brain function are still missing. Moreover, the analysis of treatment and washout effects are hindered by the challenge of repeatedly and non-invasively testing neuronal function over the course of the disorder.

Recent work introduced the use of visually evoked responses as a quantitative method to assess cortical circuit function in RTT patients carrying MeCP2 mutations (LeBlanc et al. 2015). The results obtained in humans revealed a good correlation with the results in the mouse model (LeBlanc et al. 2015; Durand et al. 2012) suggesting that the analysis of visual phenotype could also be extended to other diseases, including the CDKL5 disorder, in which abnormal function of cortical circuits can be hypothesized and animal models are available. Indeed, clinical studies indicated that several CDD patients show visual impairments (Moseley et al. 2012; Paine et al. 2012; Stalpers et al. 2012) and abnormal electroencephalographic (Melani et al. 2011) waveforms deriving from impaired activity of the cerebral cortex, in keeping with findings of morphofunctional alterations in sensory cortical circuits of CDKL5 mutant mice (Della Sala et al. 2016; Amendola et al. 2014; I.-T. J. Wang et al. 2012).

Thus, we investigated the developmental trajectory of cortical visual responses in male

mice totally missing CDKL5, and in heterozygous cdkl5 females, better recapitulating the mosaic distribution of mutant cells present in the majority of CDKL5 patients. Two independent techniques were used: longitudinal transcranial intrinsic optical signal (IOS) imaging and intracortical VEP recordings. The data showed the presence of an impairment of visual response both in male and in female mutants, first detectable at P27. This early alteration of visual responses was correlated with impairments of different parameters of cortical visual function in adulthood, and can be exploited as a classifying biomarker providing rational targets for treatment assessment.

Interestingly, such impairment in visual responses mirrors what in CDD patients is referred to as a distinctive visual impairment (Moseley et al. 2012; Stalpers et al. 2012) often clinically diagnosed as cortical visual impairment (CVI). In human patients, CVI, also designated as cerebral visual impairment, is generally due to alterations involving the retrochiasmal visual tracts in the brain with non-existent or minimal ocular morbidity (Lehman 2012). However, little is known about the neural structures involved in CVI in CDD patients.

To gain a deeper understanding of the circuits underlying visual deficits induced by CDKL5 deficiency, we characterized the specific contribution of excitatory cortical circuits to the impairment of visual responses. We used IOS imaging to record the amplitude of primary visual cortical activation in response to visual stimulation in conditional CDKL5 mutant mice with preserved CDKL5 expression in subcortical nuclei. We found that the selective deletion of CDKL5 from cortical excitatory and some glial cells is sufficient to produce abnormalities of visual cortical responses, demonstrating that CDKL5 plays an essential role in establishing or maintaining a normal function of cortical circuitry.

Finally we tested the visual impairment of IOS cortical responses as a biomarker in a preclinical setting by measuring the effect of a protein substitution therapy. We saw that this therapeutic strategy was able to ameliorate many behavioral and anatomical hallmark of the disease and notably, IOS imaging revealed that visual cortical responses were significantly improved as well. This data further corroborates the usefulness of objective measurements of cortical function as a highly quantitative and translatable biomarker of disease progression.

9.3 Personal contribution to the project

Here I summarize, for clarity, the details of my specific personal contribution to this project. All of the conceptual, experimental and analytical tasks are grouped according to the level of my involvement in three categories as follows:

- I was the only/main contributor
  - Intrinsic Signal Optical Imaging (IOS) experiments
  - Writing software for IOS analysis
  - Analysis of IOS imaging data
  - Figures layout and data visualizations
  - Development of Hardware for IOS imaging
  - Development of Software/Firmware for IOS imaging

- I collaborated in the tasks
  - Conceptualization of the project
  - Visually evoked potentials (VEPs) experiments
  - Analysis of VEPs
  - Machine-Learning (SVM) for genotype prediction
- Task performed by other people or institutions
  - Dendritic spine analysis in Golgi-stained sections
  - Development of a protein substitution therapy for CDKL5 mutant mice

10 Results

10.1 Longitudinal IOS imaging reveals decreased amplitude of cortical visual responses in developing cdkl5 mutants

To determine the impact of cdkl5 mutation on visual cortical development we examined cortical responses to visual stimulation using intact skull repeated IOS imaging in juvenile animals, and tracking response maturation in binocular visual cortex during visual development (P25–32) (Espinosa et al. 2012).

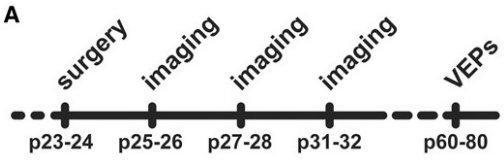

Figure 10.1: **(a)** Experimental timeline.

We examined IOS responses in the same subjects, both male cdkl5 null and female heterozygous mice compared with their age and sex matched wt littermates, at three different developmental stages Figure 10.1.

Figure 10.2A and E show typical examples of responses from the different experimental groups consisting in a decrease in reflectance (dark area) induced by visual stimulation in the visual cortex. Data quantitation showed that at the first age tested (P25–26), the amplitude of the responses to contralateral eye stimulation was comparable between cdkl5 null and control mice, however, at later ages (P27–28 and P31–32) cdkl5 null mice showed a significantly reduced response with respect to wt (Figure 10.2B, wt N=9, cdkl5 null N=7; two-way ANOVA genotype P=0.035, post hoc Holm–Sidak wt versus mutants P25–26 P=0.91, P27–28 P=0.0016, P31–32 P=0.0047).

The responses to the ipsilateral eye showed a similar pattern: no difference between genotypes at P25–26 and significantly reduced amplitude in cdkl5 null mice at P27–28 and at P31–32 (Figure 10.2C, wt N=9, cdkl5 null N=7; two-way ANOVA genotype P=0.0017, post hoc Holm–Sidak wt versus mutants P25–26 P=0.5, P27–28 P=0.024, P31–32 P=0.0028).

Interestingly, female heterozygous cdkl5 mice also showed a similar developmental impairment of contralateral evoked responses, but preserved ipsilateral response amplitude (Figure 10.2F and G, wt N=11, cdkl5 het N=7; Contralateral responses: two-way ANOVA time ×genotype P=0.017, post hoc Holm–Sidak wt versus mutants P25–26 P=0.53, P27–28 P=0.046, P31–32 P=0.049; Ipsilateral responses: two-way ANOVA time ×genotype P=0.17, genotype P=0.87).

This differential effect on ipsilateral and contralateral responses resulted in an abnormal ocular dominance index (ODI) biased toward ipsilateral eye in heterozygous mutants with

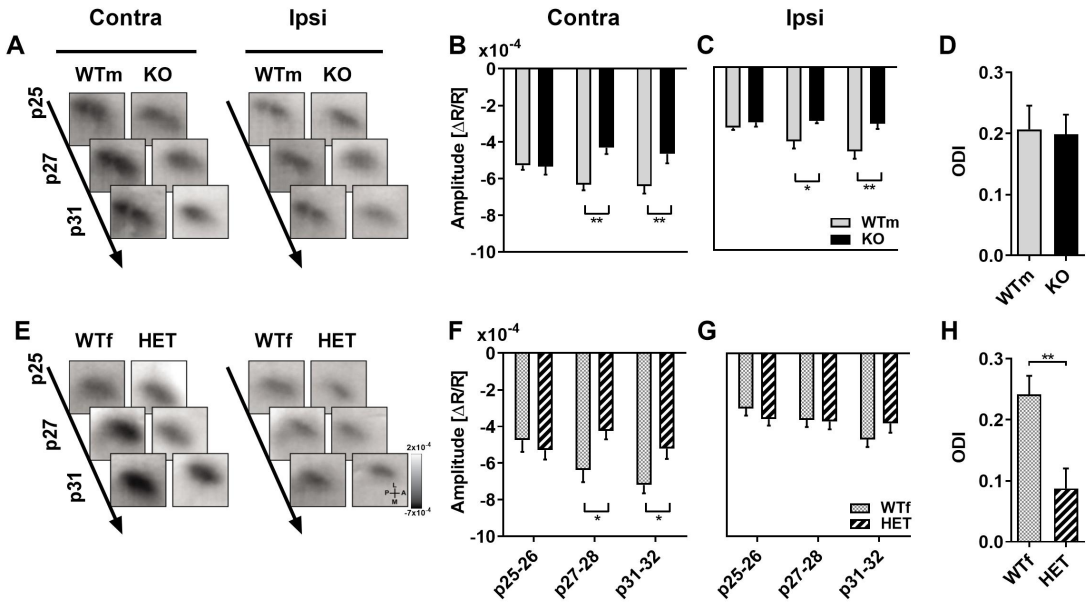

Figure 10.2: **Decreased amplitude of IOS visual responses in WT, HET and KO animals. (A)** Images collected at different ages in one male wild-type (WTm) and one cdkl5 null (KO) mice. Responses to contralateral (Contra) and ipsilateral eye (Ipsi) eye stimulation are reported. **(B)** IOS amplitude in response to contralateral eye stimulation at different ages in WTm and KO mice. **(C)** IOS amplitude in response to ipsilateral eye stimulation at different ages in WTm and KO mice. **(D)** Ocular dominance index (ODI) in WTm and KO mice. **(E)** Images collected at different ages in one female wt (WTf) and one cdkl5 heterozygous (HET) mice. Responses to contralateral (Contra) and ipsilateral eye (Ipsi) eye stimulation are reported. **(F)** IOS amplitude in response to contralateral eye stimulation at different ages in WTf and HET mice. **(G)** IOS amplitude in response to ipsilateral eye stimulation at different ages in WTf and HET mice. **(H)** Ocular dominance index in WTf and HET mice. In all panels, values are average±SEM. *p<0.05, **p<0.01. Frame size: 2×2mm.

respect to wt (Figure 10.2H, wt N=11, cdkl5 het N=7; t-test P=0.003). No change in ODI was present in null mice with respect to controls (Figure 10.2D, wt N=9, cdkl5 null N=7; t-test P=0.87).

Thus, defective development of visual responses is present after P27 both in null and heterozygous cdkl5 mutant mice.

10.2 Impaired VEP responses in juvenile and adult cdkl5 mutants

To assess cortical visual responses in cdkl5 mutants using a different technique, we recorded intracortical VEP responses to pattern reversal by means of a multielectrode inserted into the binocular visual cortex of p27–32 mice, a time point representing the onset of the visual response deficit previously observed by IOS imaging in heterozygous and null mice.

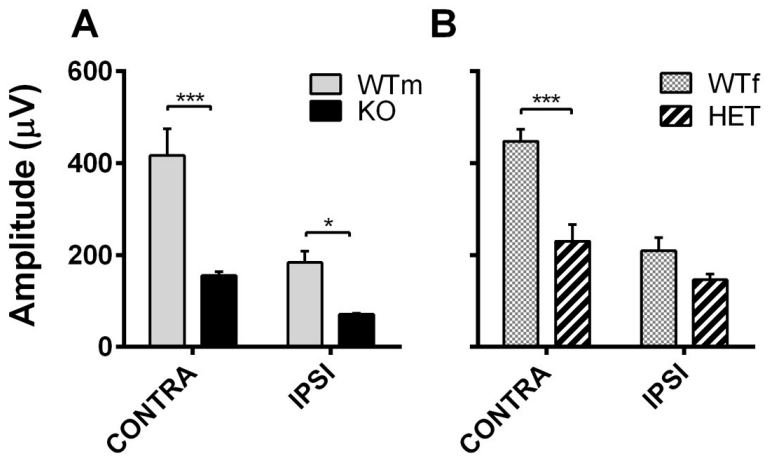

Figure 10.3: **Decreased amplitude of VEP visual responses in juvenile animals. (A)** Average VEP amplitude to 0.03 c/deg gratings for contralateral and ipsilateral eye stimulation in male wt (WTm) and CDKL5 null (KO) p27-32 mice. **(B)** Average VEP amplitude to 0.03 c/deg gratings for contralateral and ipsilateral eye stimulation in female wt (WTf) and heterozygous (HET) p27-32 mice.

VEP results reproduced IOS data showing a reduced VEP amplitude in male cdkl5 null mice for both contralateral and ipsilateral stimulation (Figure 10.3A, wt N=5, cdkl5 null N=4; two-way ANOVA genotype P<0.001, post hoc Holm–Sidak wt versus mutants Ipsilateral eye P=0.04, Contralateral eye P<0.001), and reduced VEP amplitude for contralateral eye stimulation in heterozygous cdkl5 mice (Figure 10.3, wt N=4, cdkl5 het N=5; two way ANOVA interaction eye ×genotype P=0.014, post hoc Holm–Sidak wt versus mutants Ipsilateral eye P=0.13, Contralateral eye P<0.001).

To investigate whether the developmental visual impairment persists into adulthood we recorded VEPs in P60–P80 mice. To establish whether the defect observed in juvenile mice was correlated with adult visual cortical responses, we analyzed the same mice that were studied during development by means of IOS imaging, a non-terminal procedure that allows recovery of the animal at the end of the procedure.

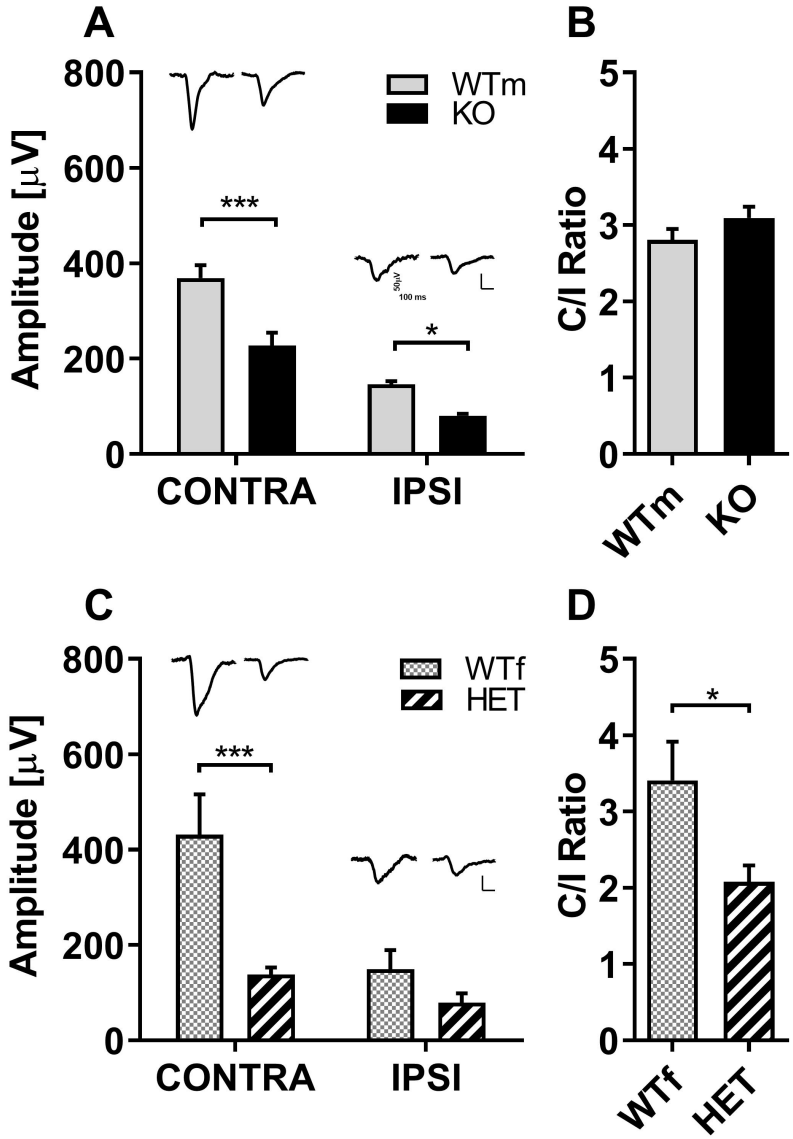

Figure 10.4: **Decreased amplitude of VEP visual responses in adult animals. (A)** Average VEP amplitude to 0.03 cyc/deg gratings for contralateral and ipsilateral eye stimulation in male wt (WTm) and cdkl5 null (KO) mice. Representative VEPs from single animals are reported above the corresponding histogram bar. **(B)** Ratio between contralateral and ipsilateral eye responses (C/I ratio) in WTm and KO mice. **(C)** Average VEP amplitude to 0.03 cyc/deg gratings for contralateral and ipsilateral eye stimulation in female wt (WTf) and cdkl5 heterozygous (HET) mice. Representative VEPs from single animals are reported above the corresponding histogram bar. **(D)** C/I ratio in WTf and HET mice. Horizontal scale bar in (A and C)=50 ms, vertical scale bar in (A and C)=100μV. In all panels, values are average±SEM. *P<0.05.

We found that VEP amplitude was reduced in adult cdkl5 null mice for both contralateral and ipsilateral eye stimulation (Figure 10.4A, wt N=6, cdkl5 null N=6; two way ANOVA genotype P<0.0001, post hoc Holm–Sidak wt versus mutants Ipsilateral eye P=0.028, Contralateral eye P=0.0001). Similarly, contralateral, but not ipsilateral, eye responses were significantly reduced in heterozygous cdkl5 females (Figure 10.4C, wt N=8, cdkl5 het N=8; two way ANOVA eye*genotype P=0.029, post hoc Holm–Sidak wt versus mutants Ipsilateral eye P=0.31, Contralateral eye P=0.0004) resulting in an abnormal ODI in cdkl5 heterozygous mice Figure 10.4D, wt N=8, cdkl5 het N=8; t-test P=0.03), but not in cdkl5 null males (Figure 10.4B, wt N=6, cdkl5 null N=6; t-test P=0.22). These data, obtained in adult mice, overlap with the results found during early development using IOS imaging.

10.3 Correlations between IOS, VEP amplitude, visual acuity and contrast response curve

The altered VEP responses found in adult cdkl5 null and heterozygous mice could result from an abnormal development of neural circuits. Since adult VEP recordings were performed in the same mice employed for IOS assessment, we investigated if there was a correlation between IOS responses during development and adult electrophysiological measurements. For this reason, we computed the correlation matrix between z-scored amplitudes of the contralaterally evoked IOS and VEPs, VEP visual acuity and the C50 parameter obtained from contrast curve fit (Figure 10.5A). Intriguingly, all these variables were significantly correlated indicating that IOS measures are in agreement with VEPs, and that altered developmental trajectories could be at the basis of the visual impairment found in adult cdkl5 mutants. These data also suggest that monitoring IOS responses during development could be a predictive tool of adult cortical visual processing.

10.4 Visual responses are a robust disease biomarker

To evaluate the reliability of the visual phenotype as a biomarker, we evaluated its accuracy, sensitivity, specificity and d' (Figure 10.6 and Figure 10.5C) using linear support vector machine (SVM), a supervised machine-learning algorithm for data classification. When trained with the entire dataset (All), the algorithm showed a remarkable discriminative capability (d'=1.32) between mutated and wild-type mice. We then performed a principal components analysis (PCA) and we selected the first two components accounting for 66.7% of the variance in the entire dataset. By using these variables, subjects were readily segregated between wt and mutants (Figure 10.5B) and the d' was significantly improved (d'=1.52; one-way ANOVA P<0.0001, post hoc Holm–Sidak All versus PCA P<0.0001). Since ease of testing is a key factor in the applicability of a disease biomarker, we also assessed whether smaller subsets of variables could reach a similar discriminative performance. The tested data subsets were composed of: visual acuity and C50 (Thresholds); contralateral and ipsilateral VEP amplitude (VEP); contralateral IOS amplitude at P27–28 and P31–32 (IOS-C); ipsilateral IOS amplitude at P27–28 and P31–32 (IOS-I). As a control we also repeated the procedure after bootstrapping the dataset of principal components (Bootstrap). Thresholds, VEP and IOS-C models showed significantly better performances than the bootstrap condition (Thresholds d': 1.21, VEP d': 0.97, IOSI-C d':

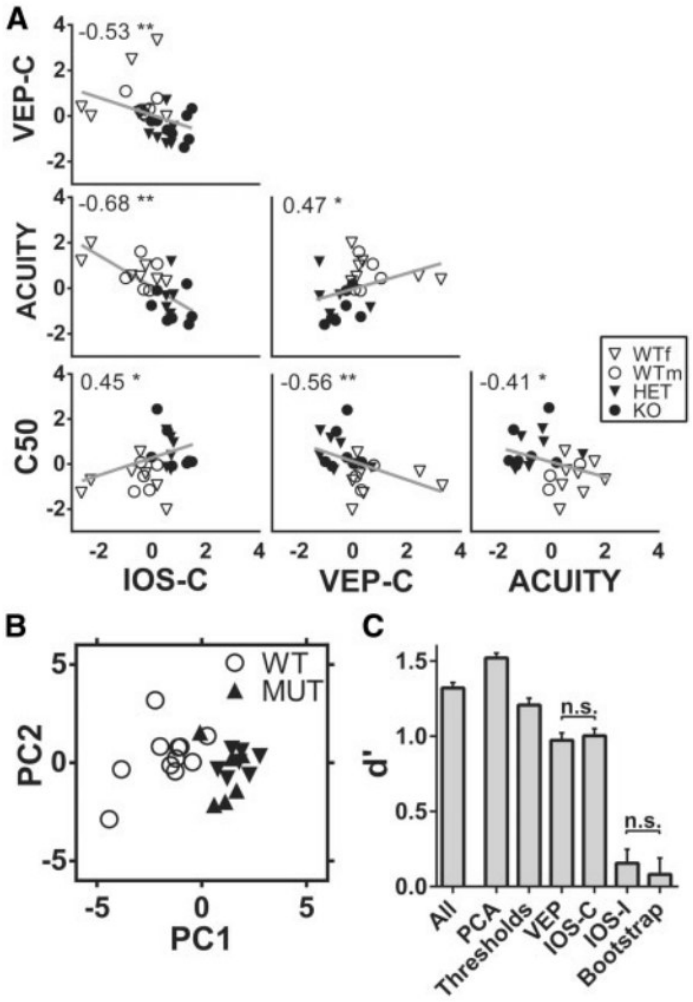

Figure 10.5: **Correlations between measurements in CDKL5 mutant animals. (A)** Correlation matrix between average contralaterally evoked IOS amplitude during development (IOS-C), contralaterally evoked VEP amplitude at P60–80 (VEP-C), VEP acuity at P60–80 (ACUITY), and the C50 parameter at P60–80 derived from Naka–Rushton fit of the contrast response curve (C50). Non-parametric Spearman correlation analysis revealed significant correlation (*P<0.05, **P<0.01, P-values corrected for multiple comparisons using BenjaminiHochberg false discovery rate) between all the variables. The correlation coefficient R is reported for each correlation in the corresponding plot. **(B)** Scatter plot of all the experimental subjects analyzed with VEP and IOS imaging plotted in the space of the first two principal components of PCA. **(C)** Comparison of d-prime for different SVM classifiers trained and tested, respectively, with: the entire dataset (All), the first two principal components (PCA), Visual acuity and C50 parameter from the contrast sensitivity curve (Thresholds), VEP amplitudes (VEP); contralateral IOS amplitudes (IOS-C); ipsilateral IOS amplitudes (IOS-I) and randomly permuted dataset (Bootstrap). n.s., not significative; all other comparisons have P<0.05. Values in C are presented as mean 95% CI.

Training dataset	Accuracy % (95% CI)	Sensitivity % (95% CI)	Specificity % (95% CI)	d' (95% CI)
All	89.96 (89.34–90.58)	89.50 (88.53–90.47)	91.50 (90.14–92.86)	1.32 (1.29 to 1.36)
PCA	93.10 (92.56–93.64)	92.21 (91.11–93.32)	97.08 (96.14–98.03)	1.52 (1.49 to 1.55)
Thresholds	87.63 (86.72–88.55)	83.79 (82.07–85.50)	92.83 (91.24–94.42)	1.21 (1.16 to 1.25)
VEP	82.58 (81.55–83.60)	82.79 (80.78–84.80)	82.50 (80.32–84.68)	0.97 (0.92 to 1.02)
IOS-C	82.94 (81.80–84.08)	85.14 (83.16–87.13)	80.58 (78.65–82.52)	1.00 (0.96 to 1.05)
IOS-I	64.88 (63.58–66.19)	73.43 (71.25–75.61)	53.17 (49.91–56.42)	0.16 (0.06 to 0.25)
Bootstrap	55.94 (54.83–57.06)	49.86 (46.32–53.40)	50.83 (47.22–54.45)	0.08 (−0.03 to 0.19)

IOS, intrinsic optical signal; VEP, visually evoked potentials; SVM, support vector machine; PCA, principal component analysis.

Figure 10.6: **Performance evaluation of SVM classifiers trained with different datasets.**

1.00; post hoc Holm–Sidak P<0.0001 for all comparisons versus Bootstrap), indicating that even simple sets of physiological parameters could be used as a tool for monitoring both disease progression and the effect of potential treatments. Interestingly, IOS-I model had a remarkably lower efficiency not significantly different from the Bootstrap model (d': 0.16; post hoc Holm–Sidak P=0.20).

10.5 Impaired visual responses in mice with deletion of CDKL5 in cortical excitatory neurons

In the previous sections, we showed that CDKL5 mutant mice present a deficit in the processing of visual stimuli that can be assessed with a remarkably high discrimination power by IOS imaging of visually evoked responses. These abnormal visual responses, however, could arise from defects in upstream visual areas with no intrinsic dysfunction present in visual cortical circuits. In order to assess the specific contribution of the visual cortex, we used a conditional KO mouse model in which the removal of the floxed CDKL5 allele in mutant mice ($CDKL5^{flox/y}$) was achieved by crossing these mice with mice expressing CRE-recombinase driven by the emx1 promoter (emx1-$CRE^{+/-}$). As a result, $CDKL5^{flox/y}$;emx1-$CRE^{+/-}$ animals (cKO) lack CDKL5 only in cortical excitatory neurons and in some glial cells (Gorski et al. 2002), thus sparing all the subcortical visual areas.

The expression of CRE-recombinase driven with the emx1 promoter is known to induce recombination as early as at embryonic day (E) 10.5 (Gorski et al. 2002), a time point in which the expression of all the most abundant isoforms of CDKL5 in the mouse brain is still very low (Hector et al. 2016). This ensures that the phenotypic effects observable in adult mice are the result of an altered development or maturation, closely resembling CDKL5 null mice and patients.

To explore the role of cortical CDKL5 in the pathogenesis of visual deficits in CDKL5 mutants, we first asked whether we could detect some functional alterations in the cerebral cortex of cKO mice. In these mice, CDKL5 is normally present in subcortical visual nuclei.

We asked whether cortical CDKL5 plays a necessary role in the normal physiology of cortical visual processing. To this purpose, we performed IOS imaging, recording visually evoked responses in male cKO animals (N=8) and, as a control, in parental mouse lines expressing CRE (N=5; emx1-$CRE^{+/-}$) or carrying a CDKL5 floxed allele (N=9; CDKL5flox/y; Figure 10.7C and D).

IOS response amplitude to visual stimulation was significantly different between groups

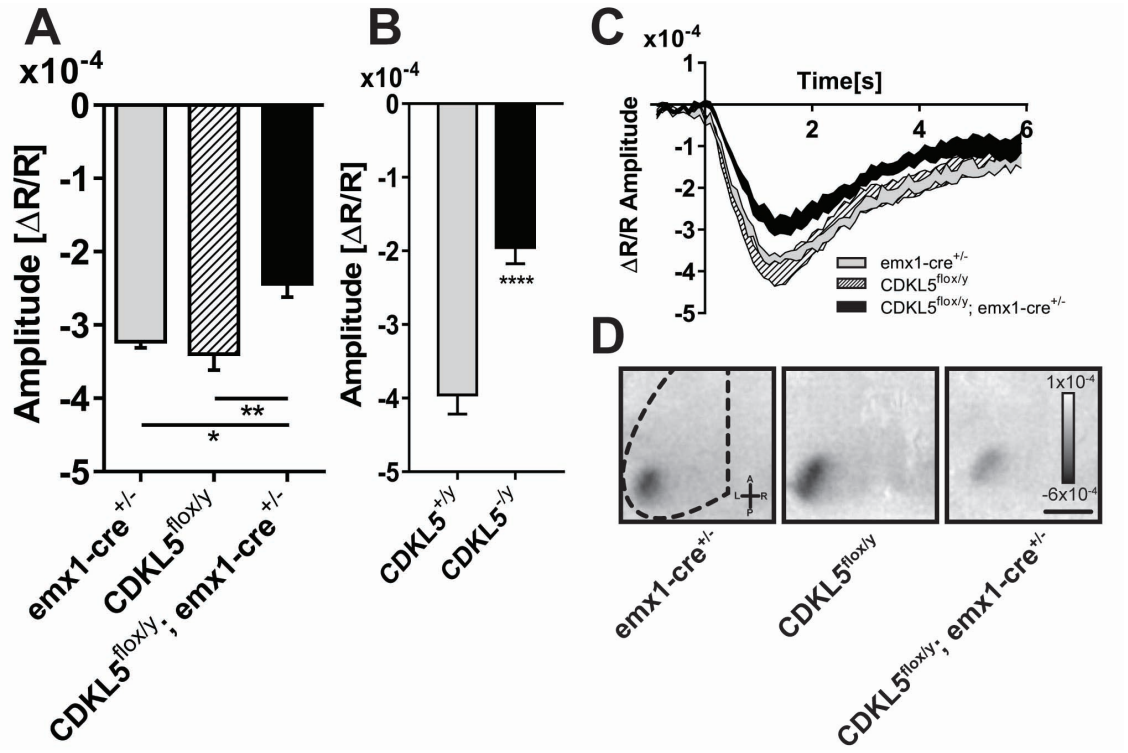

Figure 10.7: **Cortical visual responses are impaired in cKO mice with deletion of CDKL5 in cortical excitatory neurons. (A)** Quantitation of the average amplitude of the intrinsic signal between the experimental groups, cKO, floxed controls ($CDKL5^{flox/y}$) and emx1-CRE driver controls ($emx1\text{-}CRE^{+/-}$), showing a significant reduction of the evoked visual responses in cKO mice with respect to both control groups (one-way ANOVA P=0.004; post hoc Holm–Sidak's multiple comparisons test, $emx1\text{-}CRE^{+/-}$ versus cKO, P=0.0342; $CDKL5^{flox/y}$ versus cKO, P=0.0043). **(B)** Quantitation of the average amplitude of the intrinsic signal in CDKL5 null animals showing a significant reduction with respect to controls (two-tailed Student's t-test P<0.001). **(C)** Average time course of the intrinsic signal in the V1 after visual stimulation for the experimental groups in (A). Each area represents mean±SEM for all the mice in the group. **(D)** Representative images of a typical intrinsic signal response to visual stimulation localized in the V1. Dark areas represent active portions of brain tissue. *P<0.05; **P<0.01; ***P<0.001. Scale bar (C) is equal to 1.8 mm. Error bars represent SEM.

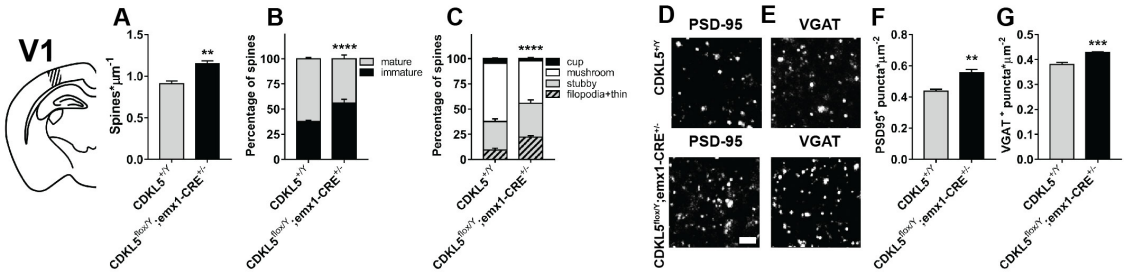

Figure 10.8: **Spine density in Golgi-stained V1 slices. (A)** Quantitation of spine density in Golgi-stained V1 slices from cKO ($CDKL5^{flox/y}$;emx1-$CRE^{+/-}$) and CDKL5+/y mice showing an increase in cKO mice (twotailed Student's t-test P = 0.0014). **(B)** Quantitation of the relative proportion of mature and immature spines in Golgi-stained V1 slices showing an increased fraction of immature spines in cKO mice compared to WT controls ($\chi 2$ test P <0.001). **(C)** Quantitation of spine morphology in Golgi-stained V1 slices showing a pattern of decreased morphological maturity in cKO mice ($\chi 2$ test P <0.001). **(D)** Representative images of PSD95 punctate staining from cKO and $CDKL5^{+/y}$ V1. **(E)** Representative images of VGAT punctate staining from cKO and $CDKL5^{+/y}$ V1. **(F)** Quantitation of PSD95+ puncta density showing an increase in cKO mice (two-tailed Student's t-test P = 0.0085). **(G)** Quantitation of VGAT+ puncta density showing an increase in cKO mice (two-tailed Student's t-test P <0.001). *P <0.05; **P <0.01; ***P <0.001. Calibration bar is equal to 2 µm. Error bars represent SEM.

(Figure 10.7A; one-way analysis of variance (ANOVA) p=0.004). cKO animals showed a decreased response amplitude with respect to both CRE expressing mice (post hoc Holm–Sidak's multiple comparisons test; emx1-$CRE^{+/-}$ versus cKO; P=0.0342) and CDKL5 floxed mice (post hoc Holm–Sidak's multiple comparisons test; $CDKL5^{flox/y}$ versus cKO; P=0.004). Such a reduced response is also evident in the average time course of the cortical reflectance for each group (Figure 10.7C).

In order to further characterize the precise impact of cortical CDKL5 onto the visual deficit, we also recorded IOS responses from germline mutant mice. As expected from previously published data (Mazziotti et al. 2017), this cohort recapitulated the impairment in the amplitude of visual responses (Figure 10.7B; two-tailed Student's t-test P<0.001). Interestingly, by quantitatively measuring the magnitude of the impairment using Cohen's d as an effect size estimator (Cohen 1988), we noticed that the effect produced by the germline deletion of CDKL5 was bigger (Cohen's d=2.78) than the one produced by conditional deletion from excitatory cortical cells (Cohen's d=1.73), although the effect size can be regarded as very large for both CDKL5 null mice and cKO (Sawilowsky 2009). Thus, the effect size analysis suggests a major role for the cortex in generating the visual phenotype although it cannot be excluded an enhancement of the deficit by defects in other brain areas or cell types.

cKO animals lack CDKL5 from only excitatory cortical neurons and some glial cells. To characterize the structural abnormalities underlying such functional deficit, we performed a series of anatomical analysis in the V1 of cKO animals. Surprisingly, dendritic protrusion density in Golgi-stained dendrites of layer 2/3 (Figure 10.8) cortical cells was increased in cKO animals compared to controls (Figure 10.8A; two-tailed Student's t-test P=0.0014).

This increase, however, was accompanied by a marked shift in dendritic spine morphology

toward a more immature state (Figure 10.8B, $\chi 2$ test $P<0.001$; Figure 10.8C, $\chi 2$ test $P<0.001$). In accordance with the increase in spine density, also the density of PDS95+ puncta, assessed in layer 2/3, was increased (Figure 10.8D and F; two-tailed Student's t-test $P=0.0085$) in the cKO animals.

Intriguingly, despite the fact that CDKL5 deletion happened only in excitatory cells, we also found an increase in the density of layer 2/3 VGAT+ puncta (Figure 10.8E and G; two-tailed Student's t-test $P<0.001$) suggesting that a complex interaction between excitatory and inhibitory cells, possibly involving non-cell-autonomous effects, might be induced by CDKL5 mutations.

10.6 IOS imaging as a biomarker in preclinical testing of potential therapies

Since the impairment of visual responses represents a promising biomarker for preclinical and clinical studies on CDKL5 disorder, we evaluated the effect of the treatment with a protein substitution therapy, consisting of a modified version of the wild-type CDKL5 protein, fused to the HIV-1 transactivator of transcription (TAT) protein. We decided to test in-vivo the effect of TAT_{κ}-GFP-$CDKL5_1$, one of the isoforms of CDKL5, because it is the most expressed isoform in the central nervous system (22). As a control, we used a TAT_{κ}-GFP fusion protein, since it has been shown that GFP does not influence cellular functions.

Here, we evaluated the effect of a subchromic treatment with TAT_{κ}-GFP-$CDKL5_1$ or TAT_{κ}-GFP proteins on visual cortical responses in Cdkl5 KO mice. We used an infusion method which is based on a programmable pump (IPRECIO, Primetech, Japan) implanted under the skin with a refillable reservoir. The pump was connected to a catheter implanted in the carotid artery. In view of the turnover of the TAT_{κ}-GFP-$CDKL5_1$, we decided to use a twice-a-day infusion protocol (bolus delivered at 9 am and 9 pm; see Materials and Methods for details) for the duration of 10 day. In order to assess the long-lasting effect of the treatment, $Cdkl5^{-/Y}$ mice were also tested on the 10th day of treatment and after 5 and 10 days after the end of treatment (Figure 10.9B).

We found that, while TAT_{κ}-GFP-treated $Cdkl5^{-/Y}$ mice showed no improvement in visual responses compared with the baseline condition (Figure 10.9B), $Cdkl5^{-/Y}$ mice treated with the TAT_{κ}-GFP-$CDKL5_1$ protein underwent a progressive restoration of visual responses that fell within the 95% confidence interval of wild-type mice (Figure 10.9A,B). The positive effect of the TAT_{κ}-GFP-$CDKL5_1$ protein treatment on visual response was retained 5–10 days after treatment cessation (washout), indicating a long-lasting effect of the protein replacement treatment.

This amelioration of visual cortical responses, was paralleled by benefic effects on behavioral (reduced number of REM sleep apneas) or anatomical, (density of dendritic spines and PDS-95 puncta) aspects of the disease (data shown in (Trazzi et al. 2018)), thus indicating that the measurement of visual responses with IOS imaging can be used as a biomarker even in preclinical testing of potential therapies.

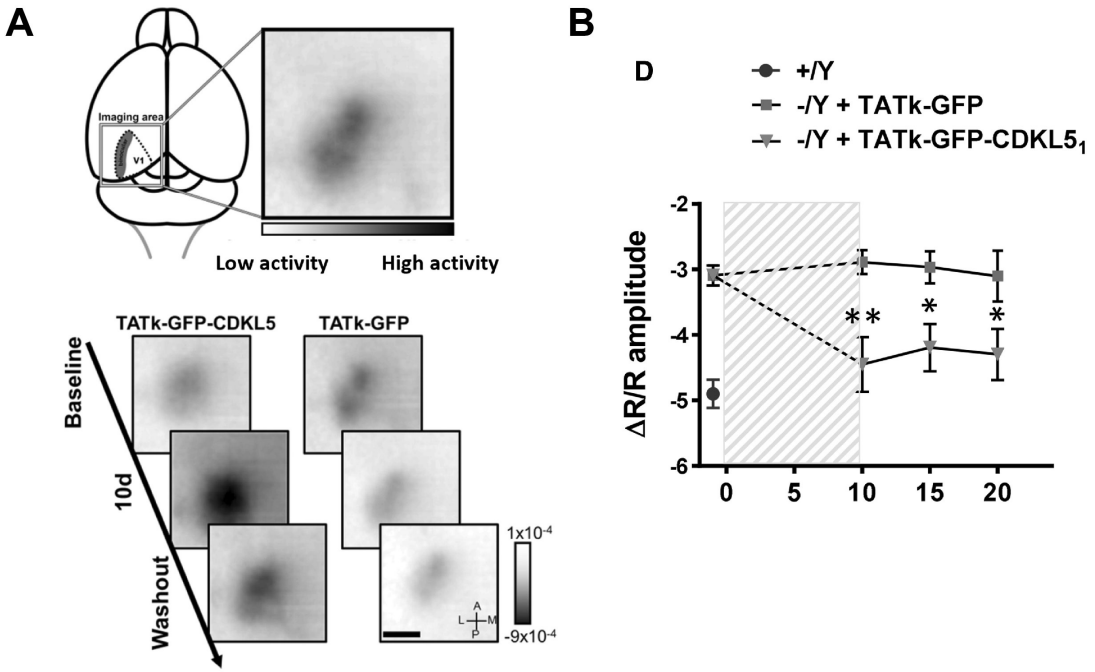

Figure 10.9: **Effect of systemically-administered TAT$_\kappa$-CDKL5 on visual cortex. (A)** Upper panel: diagram of the field of view for IOS imaging experiments. Darker areas in the figure represent the active parts of the primary visual cortex (V1) following visual stimulation corresponding to the binocular visual cortex. Lower panel: representative IOS response images collected at different time points in two Cdkl5$^{-/Y}$ mice treated with TAT$_\kappa$-GFP and TAT$_\kappa$-GFP-CDKL$_1$, respectively. Scale bar: 1 mm. **(B)** Mean amplitude of visually evoked IOS responses measured before and after 10 days of treatment in Cdkl5$^{-/Y}$ mice treated with TAT$_\kappa$-GFP (n = 8) and TAT$_\kappa$-GFP-CDKL$_1$ (n = 9). The persistence of the effect was evaluated with additional measurements 5 and 10 days after treatment cessation (washout). Values are represented as means ± SE Two-way RM ANOVA (repeated measures for the factor time) revealed a time * treatment interaction $P<0.05$; post-hoc Holm–Sidak's multiple comparisons test: * $P<0.05$.

11 Discussion

The availability of animal models has greatly benefited the efforts to individuate molecular and cellular underpinnings of cdkl5 syndrome (Amendola et al. 2014; I.-T. J. Wang et al. 2012). Moreover, behavioral assessment has outlined significant impairments in different domains (Amendola et al. 2014; I.-T. J. Wang et al. 2012; Fuchs et al. 2015; Trazzi et al. 2016). However, there remains a pressing need for biomarkers of high translational value to non-invasively and quantitatively monitor brain function throughout progression of the disorder and during treatment.

In recent years, the visual cortex has become an important model to assess cortical processing in mouse model of neurodevelopmental disorders (Durand et al. 2012; Begenisic et al. 2015; E. M. Boggio et al. 2016). For instance, the use of visually evoked responses has been suggested as a relatively common quantitative method to directly compare cortical function in RTT patients and mouse models carrying mecp2 mutations (LeBlanc et al. 2015; Durand et al. 2012). VEPs have also been used to reveal alterations in West Syndrome patients, EIEE1 (OMIM ref: 308350), and in EIEE3 (OMIM ref: 609304), supporting the translational and clinical applicability of this technique even in presence of seizures or hyperexcitability (Freitas Dotto et al. 2014; Molinari et al. 2005).

Here, we used transcranial IOS and intracortical VEPs to investigate visual cortical function in cdkl5 mutant mice. The results showed that cortical responses are dramatically reduced in amplitude already at P27-P28, as assessed both with IOS and VEPs, and that this reduction is significantly correlated with decreased response amplitude, abnormal contrast response function, and impaired visual acuity in adult mutants. Importantly, these alterations were detected both in male mice with no expression of cdkl5 and in heterozygous female mutants with mosaic expression of the remaining cdkl5 allele. Sensitivity analysis revealed that visual responses were able to correctly classify mice in mutant or wild-type with more than 93% accuracy and 92% sensitivity proving the robustness of this technique in phenotype assessment.

Our results suggest that monitoring deficits in cortical visual function can be applied to cdkl5 syndrome. This possibility is in agreement with clinical studies indicating that cdkl5 patients show visual impairments (Moseley et al. 2012; Paine et al. 2012; Stalpers et al. 2012). Moreover, previous studies showed that adult cdkl5 mutant mice have altered neural responses in sensory cortices (Amendola et al. 2014; I.-T. J. Wang et al. 2012) and impaired visual optokinetic reflex (Amendola et al. 2014). A fundamental issue in analyzing phenotypes in mouse models of neurodevelopmental disorders is to understand whether the defective phenotype is a primary deficit occurring at the disease onset or a late secondary manifestation of the disease. Knowledge about the onset of the symptoms is useful to optimize treatment schedule and to formulate hypotheses on the underlying neurobiological defects generating the deficit. Our results indicate that, both in cdkl5 null males and in heterozygous females, an impairment in visual responses begins to be present during development, in correlation with the increase of cdkl5 expression occurring during forebrain postnatal development (Rusconi et al. 2008; Chen et al. 2010; Hector

et al. 2016). Furthermore, the degree of impairment of cortical visual responses present in juvenile mutants was correlated with the deficits observed in the same animals when they became adult, suggesting that the alteration of developmental maturation mechanisms by cdkl5 mutation is responsible for the impaired visual cortical function during adulthood.

Both the onset of visual response impairment in mice and the appearance of symptoms in humans take place during a period of intense synaptogenesis and synaptic plasticity, in agreement with the proposed role of cdkl5 in synaptic organization (Ricciardi et al. 2012; Della Sala et al. 2016; Zhu et al. 2013).

In the last part of this work, we investigated which part of the visual the circuitry gives rise to the abnormalities in VEP and IOS cortical responses. Indeed, damage anywhere along the visual path may affect the signal in the cortex. Our study provides evidence supporting a cortical origin of such visual response deficit. Indeed, deletion of CDKL5 only from excitatory cells of the visual cortex was sufficient to elicit a significant impairment of visual responses.

The use of the emx1 promoter to drive Cre recombinase expression and CDKL5 deletion also preserves CDKL5 expression in inhibitory neurons. Global CDKL5 KO cortex has altered inhibitory synaptic labeling and increase in parvalbumin positive cells (Pizzo et al. 2016). CDKL5 deletion from inhibitory cells has been previously shown to result in a partial phenotype (Amendola et al. 2014; E. Schroeder et al. 2019); however, visual function was not tested in these models. Our data suggest that CDKL5 deficiency in inhibitory cells is not strictly necessary for the reduction of visual responses, although we cannot exclude that visual deficits could be induced by CKDL5 deletion from inhibitory cells. An indirect involvement of inhibitory cells in the visual impairment of CDKL5 cKO could be hypothesized considering the results of our morphological analysis showing dramatic rearrangements occurring both in excitatory and inhibitory synaptic contacts in the cKO mouse. This non-cell-autonomous phenotype is reminiscent of the one observed in the hippocampus of CDKL5 mutants with deletion restricted to excitatory neurons (Tang et al. 2017) where an increase in the frequency of miniature inhibitory synaptic currents was observed. These indirect effects of CDKL5 mutation could be relevant for the understanding of the circuit deficits present in patients that are often a mosaic of normal and mutant cells.

Studies performed in cdkl5 mice reported abnormal turnover and density of dendritic spines, and reduced expression of proteins involved in excitatory synaptic structure in different brain areas, including sensory cortices (Della Sala et al. 2016; Amendola et al. 2014; Trazzi et al. 2016). In particular, a recent morphological analysis focused on the developing visual cortex showed reduced staining for the activity-dependent protein c-fos and for key components of the excitatory postsynaptic protein assembly together with increased numbers and connectivity of parvalbumin-positive inhibitory interneurons (Pizzo et al. 2016). The possibility that cdkl5 acts both on excitatory and inhibitory neurons is strengthened by previous work showing distinct but overlapping phenotypes in mice with cdkl5 deletion selectively from excitatory or inhibitory neurons (Amendola et al. 2014). Therefore, a defective maturation of excitatory and inhibitory circuits could contribute to the impaired visual cortical responses observed here.

Intriguingly, our data suggest that the contralateral and the ipsilateral responses could be differentially sensitive to cdkl5 mutation. Indeed, ipsilateral responses of mutant heterozygous females, albeit consistently reduced, were not statistically affected. Whether this is due to differential effects of cdkl5 on the crossed and uncrossed pathways, or to

the low statistical power due to the combination of low signal-to-noise ratio of mouse ipsilateral responses and the variability intrinsic to cdkl5 mosaicism, is still to be clarified.

Finally, we showed that visual cortical responses can be used as a highly quantitative and objective biomarker also in testing preclinical drugs in mouse models of the disease. A subchronic treatment with $TAT_{\kappa}GFP\text{-}CDKL5_1$ was in fact able to ameliorate behavioral and anatomical hallmark of the disease in CDKL5 null mice. Such amelioration was also present in IOS visual cortical responses thus showing a high degree of correlation with other indicators of the disease.

In summary, we found that the developmental trajectory of visual cortical development is altered in cdkl5 mutants. Our data were obtained with two different techniques that provided highly correlated data increasing the robustness of the results. Moreover, we showed that visual assessment can be used to automatically classify subjects with high reliability.

Importantly, VEP and IOS reduction of contralateral responses in both null and het cdkl5 mice exhibited a large effect size (>1.3) that was obtained with approximately the same number of animals for both sexes, suggesting that contralateral visual response deficit is not linearly dependent on the percentage of cells carrying the mutation. VEP recordings can be readily applied to humans and other species, increasing the translational value of the visual biomarker.

A reduction of visual responses persisted in a conditional KO mouse model in which a functional copy of CDKL5 was removed only in excitatory cortical cells. Thus suggesting that the origin of the abnormalities in cortical function are, at least in part, to be searched in the development of cortical circuits.

Transcranial IOS imaging, a minimally invasive and longitudinal technique, is also comparable to techniques used in humans: indeed, it detects the same blood-oxygenation level dependent signal measured by other widely used methods to assess responsiveness in newborns and infants like functional magnetic resonance imaging or functional near infrared spectroscopy or tomography. We expect that these techniques will be extremely valuable to monitor longitudinally the effectiveness of treatments and washout effects in preclinical, and possibly clinical, studies of novel treatments for cdkl5 disorder.

12 Methods

12.1 Animals

Animals were maintained in rooms at 22°C with a standard 12-h light-dark cycle. During the light phase a constant illumination below 40 lux from fluorescent lamps was maintained. Food (standard diet, 4RF25 GLP Certificate, Mucedola) and water were available ad libitum and changed weekly.

Open-top cages (36.5×20.7×14 cm; 26.7×20.7×14 cm for up to 5 adult mice or 42.5×26.6×15.5 cm for up to 8 adult mice) with wooden dust-free bedding were used. All the experiments were carried out in accordance with the directives the European Community Council (2011/63/EU) and approved by the Italian Ministry of Health. All necessary efforts were made to minimize both stress and the number of animals used.

The mice used in this work derive from the cdkl5 null strain in C57BL/6N background developed in (Amendola et al. 2014) and backcrossed in C57BL/6J for three generations. Male wt mice were bred with female hets to obtain mutant and wt littermates.

To generate conditional knock-out mice lacking CDKL5 only from pallial structures, sparing most of the subcortical regions, we crossed homozygous mice bearing a floxed version of CDKL5, described in (Amendola et al. 2014), with mice expressing CRE recombinase under the control of emx1 promoter (The Jackson Laboratory; B6.129S2-Emx1tm1(cre)Krj/J, stock no. 005628) (Gorski et al. 2002).

Weaning was performed at P21–23. Genotyping (P10–12) was performed on tail tissue as described in (Amendola et al. 2014). Colony founders were selected for the absence of the rd8 retinal degeneration allele spontaneously present in C57BL/6N mice (Mattapallil et al. 2012). The experimental groups were divided by sex: male cdkl5 null and female heterozygous mice were compared with male wt and female wt littermates, respectively.

12.2 Intrinsic optical signal imaging (IOS)

12.2.1 Surgery

For chronic IOS preparations, mice (P23–24) were deeply box-anesthetized and maintained with isoflurane (respectively, 3 and 1%), placed on a stereotaxic frame and head fixed using ear bars. Body temperature was controlled using a heating pad and a rectal probe to maintain the animals' body at 37°C. Local anesthesia was provided using subcutaneous lidocaine (2%) injection and eyes were protected with dexamethasone-based ointment (Tobradex, Alcon Novartis).

The scalp was removed and the skull carefully cleaned with saline. Skin was secured to the skull using cyanoacrylate. Then a thin layer of cyanoacrylate is poured over the exposed skull to attach a custom made metal ring (9 mm internal diameter) centered over the binocular visual cortex. When the glue dried off, a drop of transparent nail polish was spread over the area to ameliorate optical access.

After surgery the animals were placed in a heated box and monitored to ensure the absence of any sign of discomfort. Before any other experimental procedure, mice were left to recover for 24/48 h. During this period, paracetamol (5 mg/ml) was administered in the water as antalgic therapy.

12.2.2 Visual stimulation, data acquisition and analysis

IOS recordings were performed under avertin anesthesia (20 µl/g, i.p.) at P25–26, P27–28 and P31–32. Images were visualized using an Olympus microscope (BX50WI). Red light illumination was provided by 8 red LEDs (625 nm, Knight Lites KSB1385-1P) attached to the objective (Zeiss Plan-NEOFLUAR 5x, NA: 0.16) using a custom made metal LED holder (Harrison et al. 2009). The animal was secured under the objective using a ring-shaped neodynium magnet (supermagnete, R-12-09-1.5-N) mounted on an arduino-based 3D printed imaging chamber that also controls eye shutters and a thermostated heating pad (Lab rigger link).

Visual stimuli were generated using Matlab Psychtoolbox and presented on a gamma corrected 9.7 in. monitor, placed 10 cm away from the eyes of the mouse. Square wave gratings were presented in the binocular portion of the visual field (-10°to +10°relative to the horizontal midline and -5°to +50°relative to the vertical midline) with a spatial frequency of 0.03 cyc/deg, mean luminance 20 cd/m^2 and a contrast of 90%. The stimulus consisted in the abrupt contrast reversal of a grating with a temporal frequency of 4 Hz for 1 s, time locked with a 16-bit depth acquisition camera (Hamamatsu digital camera C11440) using a parallel port trigger. Interstimulus time was 14 s.

Frames were acquired at 30 fps with a resolution of 512×512 pixels. A total of 210 frames were captured for each trial: 30 before the stimulus as a baseline condition and 180 as post-stimulus. The signal was averaged for at least 30 trials and downsampled to 10 fps. Fluctuations of reflectance (R) for each pixel were computed as the normalized difference from the average baseline (ΔR/R). For each recording, an image representing the mean evoked response was computed by averaging frames between 0.5 and 2.5 seconds after stimulation. The mean image was then low-pass filtered with a 2D average spatial filter (30 pixels, 117 µm2 square kernel).

To select the binocular portion of the primary visual cortex for further analysis, a region of interest (ROI) was automatically calculated on the mean image of the response to ipsilateral stimulation by selecting the pixels in the lowest 30% ΔR/R of the range between the maximal and minimal intensity pixel (Cang et al. 2005). The same ROI was used for the analysis of contralateral eye responses.

The data processing is as follows. Mean evoked responses were quantitatively estimated as the average intensity inside the ROI. ODI was calculated as $(C - I)/(C + I)$ for each pixel, where C and I indicate the amplitude of contralateral and ipsilateral responses, respectively (Cang et al. 2005). To weaken background fluctuations a manually selected polygonal region of reference (ROR) was subtracted. The ROR was placed where no stimulus response, blood vessel artifact or irregularities of the skull were observed (Heimel et al. 2007).

12.3 Visually evoked potentials

12.3.1 Surgery

General anesthesia was induced in mice with 3% isoflurane, subsequently deeply anesthetized with an intraperitoneal injection of urethane (0.7 ml/h g; 20% solution in lactated ringer solution) and head-fixed in a stereotaxic frame. After the removal of the ring implant, the skull was exposed and a small craniotomy (2× 2 mm) overlying the visual cortex was performed, leaving the dura mater intact. Then, a multichannel neural probe (Q-trode tetrode configuration, Neuronexus) was slowly inserted at a depth of 150-200 µm, in the binocular visual cortex (lambda: +3.2 mm lateral, +0.2 mm rostral and following IOS derived coordinates), where a high amplitude positive VEP is detectable. Signal was acquired using Cheetah 32 (Neuralynx) recording system at 30.3 kHz of sampling rate with a band pass filter of 0.1-250 Hz. Signal from each channel was averaged to obtain VEPs.

12.3.2 Visual stimulation and data acquisition

Both stimuli and analysis for VEP recordings were performed using custom software written in Matlab Psychtoolbox and displayed onto a gamma corrected 21 inch CRT monitor placed 20 cm in front of the animal. Stimuli consisted in contrast reversal square wave gratings with a spatial frequency of 0.03 cyc/deg, mean luminance of 25 cd/m2 and a contrast of 90%. Monitor was centered on animal head and stimuli covered ±55°relative to vertical and -5°+30°relative to vertical midline.

Stimulus temporal frequency was 2 Hz. VEP responses were averaged for at least 100 trials per eye. Each condition was repeated for at least eight times. The amplitude quantification of the response was calculated as the peak to baseline difference of the first positive component (at approx. 100 ms).

Visual acuity is calculated presenting contrast reversal sinewave gratings with different spatial frequencies (0.03, 0.06, 0.012, 0.024, 0.048, 0.96 and 0 cyc/deg) and calculating the maximal spatial frequency resolved by linear fit estimation of parameters and extrapolation of amplitude at 0 µV in a semi-logarithmic space.

Contrast sensitivity was calculated using 0.03 cyc/deg contrast reversal sine wave gratings with different contrasts (90, 50, 25, 12, 6, 3 and 0%). Normalized amplitude data was fitted to a sigmoid curve using Naka–Rushton function, $Resp(c) = Cn/(C_{50}n + Cn)$, to extract contrast sensitivity parameters (Naka et al. 1966; Sarnaik et al. 2014; Albrecht et al. 1982). C_{50} is the contrast evoking half the maximum response and n describes the shape of the curve.

12.4 SVM classifier

Z-scored values of each physiological parameter were used for linear support vector machine (SVM) classification. SVM is a supervised machine learning method for data classification that can be trained to find the best hyperplane that separates all data points in two user-defined classes and can subsequently be exploited to blind-predict the class to which a new observation belongs (Pereira et al. 2009; Orrù et al. 2012; Cortes et al. 1995).

We defined two classes: mutated (heterozygous and null) and wild-type (males and females) mice. By using the Matlab function svmtrain, we trained the SVM with a subset of data consisting of 50% of the dataset and we than used the remaining 50% for testing, using the svmclassify function. Accuracy, sensitivity, specificity and D-prime (d') were then computed for the categorical classification in order to evaluate its performance. This procedure was repeated 200 times, each one with a randomly divided training and testing subsets.

Values for accuracy, sensitivity (or true positive rate), specificity (or true negative rate) and d' were averaged across iterations. Accuracy, sensitivity and specificity were defined as $(TP + TN)/total$, TP/P and TN/N, respectively, where TP: True positive, TN: True Negative, P: total positives, N: total negatives. D-prime, which measures the distance between the signal and the noise means in standard deviation units (Stanislaw et al. 1999), was calculated using matlab function dprime simple.

12.5 dLGN and V1 morphological analysis

12.5.1 Tissue preparation and histology

Male mice (2–3 months old) were euthanized with isoflurane (2% in pure oxygen) and sacrificed by cervical dislocation. Brains were quickly removed and cut along the midline. Right hemispheres were processed for IHC, while left hemispheres were Golgi stained as described below. All steps of sectioning, imaging and data analysis were conducted blindly to genotype.

For PSD95 and VGAT IHC, right hemispheres were fixed by immersion in 4% PFA in 0.1 M PB pH 7.4, stored in fixative for 48 h, kept in 20% sucrose w/w dissolved in 0.1 PB for an additional 24 h and then frozen with cold ice. Right hemispheres were cut with a freezing microtome into 30 µm thick coronal sections that were serially collected. One out of four free-floating sections from the LGN and from the V1 were incubated for 24 h at 4°C with the following primary antibodies: a rabbit polyclonal anti-PSD95 antibody (1:1000; Abcam Ltd Cambridge UK; ab 18258) or rabbit polyclonal anti-VGAT antibody (1:600; Synaptic System, Göttingen, Germany). Sections were then incubated at room temperature for 2 h with a CY3-conjugated goat anti-rabbit IgG (1:200; Jackson Immuno Research Laboratories, Inc. PA, USA).

For Golgi staining, left hemispheres were Golgi-stained using the FD Rapid Golgi Stain TM Kit (FD NeuroTechnologies, MD, USA). Briefly, hemispheres were immersed in the impregnation solution containing mercuric chloride, potassium dichromate and potassium chromate and stored at room temperature in darkness for 2–3 weeks. Hemispheres were cut with a microtome in 100 µm thick coronal sections that were directly mounted on gelatin-coated slides and were air dried at room temperature in the dark for an additional 2–3 days. After drying, sections were rinsed with distilled water and subsequently stained in the developing solution of the kit.

12.5.2 Imaging and data analysis

All analyses were carried out in cortical layers 2/3 and 5 from the V1 and in the LGN identified according to the Paxinos mouse brain atlas (Paxinos et al. 2020). For quantification of PSD95 and VGAT immunoreactive puncta, images were acquired using a

LEICA TCS SL confocal microscope (Leica Microsystems; 63× oil immersion objective, NA 1.32; zoom factor, 8).

Three to four sections per animal were analyzed and puncta counts were performed on a single plan, 1024 × 1024 pixel images. Counting was carried out using Image Pro Plus software (Media Cybernetics, Silver Spring, MD, USA) and the number of PSD95 and VGAT immunoreactive puncta was expressed per µm2. For the quantification of dendritic spines, images were acquired using a Leica light microscope (Leica Microsystems; 100× oil immersion objective, NA 1.4).

Dendritic spine density was measured by manually counting the number of dendritic spines on dendritic segments in the LGN and on secondary dendrites of pyramidal neurons of layer 2/3 and layer 5 of the V1. In each mice, 15 dendritic segments (segment length, 10–30 µm) from each zone were analyzed and the linear spine density was calculated by dividing the total number of counted spines by the length of the sampled dendritic segment.

Based on their morphology, dendritic spines can be divided into five different classes (immature spines: filopodium-like, thin- and stubby-shaped; mature spines: mushroom- and cup-shaped), which also reflect their state of maturation. The total number of spines was expressed per µm and the number of spines belonging to each class was counted and expressed as a percentage.

12.6 CDKL5 proteic therapy

12.6.1 CDKL5 vectors

Human CDKL5$_1$ cDNA was kindly provided by Nicoletta Landsberger (University of Milan) (23). The secretable vector pPTKGFP, containing Ig-chain V-J2-C signal peptide and codifying for the TAT$_\kappa$-GFP-myc-6xHis protein was kindly provided by Mahvash Tavassoli (King's College, London) (Williamson et al. 2012) . The TAT$_\kappa$-GFP-CDKL5$_1$ construct was produced as follows: human CDKL5$_1$ cDNAs was amplified using the following primers:

- 5-CCGCTCGAGCGAAGATTCCTAACATTGG-3 (forward),
- 5-CCGCTCGAGCGGACAAGGCTG TCTCTTTTAAATC-3 (reverse for CDKL5$_1$)

and cloned into pPTKGFP XhoI site in frame with upstream GFP sequence and downstream myc sequence.

12.6.2 protein purification and concentration

HEK293T cell lines expressing TAT$_\kappa$-GFP, and TAT$_\kappa$-GFP-CDKL5$_1$ were grown for 48 h in serum-free culture medium (Dulbecco's modified Eagle's medium supplemented with 2 mM of glutamine and antibiotics: penicillin, 100 U/ml; streptomycin, 100 lg/ml). The culture medium containing the secreted proteins was collected, centrifuged to pellet cell debris and filtered through 0,2 mm syringe filters. The culture medium was then transferred to Amicon Ultra Centrifugal Filters (Millipore) with 50 kDa molecular weight cut-off, and proteins underwent diafiltration according to the manufacturer's instructions.

12.6.3 IPRECIO pump implantation and infusions

Catheters for mouse carotid artery (INSTECH Laboratory, USA) were treated with tridodecylmethylammonium chloride (TDMAC, Sigma Aldrich, Italy) and heparin (Vister, 5000 UI/ml, Pfizer) solutions following the manufacturer's instructions to prevent blood clots and then connected to micro infusion refillable pumps (IPRECIO SMP300, Primetech Corporation, Japan). Adult Cdkl5$^{-/Y}$ mice (4–6 months old) were anesthetized with isoflurane (2% in pure oxygen), the tip of the catheter was inserted into the internal carotid artery (cranial direction) and the IPRECIO pump was placed subcutaneously on the back of the mouse. Analgesic (Carprofen 5 mg/kg) and antibiotic (12 500 U.I./kg benzylpenicillinbenzathine 5mg/kg dihydrostreptomycinsulphate) were given subcutaneously to each mouse.

A long postoperative recovery period (2 weeks) was allowed between the IPRECIO pump implantation and the beginning of drug administration. During this period, each IPRECIO reservoir was filled with saline and just 1 daily bolus (at 10 ml/h for 1 h) was administered with a low constant release (0.6 ml/h) during the rest of the day.

The IPRECIO reservoir (130 ml) was filled either with TAT$_\kappa$GFP-CDKL5$_1$ or TAT$_\kappa$-GFP, and a 10-day infusion protocol was programmed as followed: 2 daily (1 in the morning and 1 in the evening) boluses (20 ml each corresponding to 50 ng of protein) were administered at 10 ml/h with a low constant release(0.4ml/h) during the rest of the day to prevent catheter occlusion.

Every 2 or 3 days, mice were briefly anesthetized to refill the IPRECIO reservoir (transdermal injection) with fresh solutions. Saline infusions lasted for 10 more days following the same administration protocol (washout period) during which saline was continuously administered (at 0.4 ml/h).

Acknowledgements

The research presented in this document was possible thanks to the contributions (direct and indirect, academic and non academic) of a great number of generous and talented people. Here, I would like to acknowledge them.
I deeply cherish the piece of life that we shared.

Thanks to my mother and father, for being the very reason I am in this world, and for never failing to make me feel like someone was on my side throughout the years.

Thanks to my mentor and supervisor Tommaso, for allowing me to work at your side and fall in love with neuroscience. You have been a huge inspiration and taught me so many lessons. Thanks to all the people in the lab, teachers, collaborators, colleagues and students. In particular, thanks to Andrea, Alexia, Aurelia, Edda, Elena, Elsa, Fabio, Francesca D., Francesco, Giulia, Laura, Luca, Manuella, Paola, Raffaele, Sara and Valentino.

Thanks to my entire family for their precious and unconditional support. A special thanks to Lisa, Remo, Alberto, Vittoria, Teo, Medoro, Luciano and Graziella.

Finally, thanks to Francesca. You, more than anyone else, shared with me joy and sorrow, worry and solace, and made this path worth walking.

Ringraziamenti

Le ricerche presentate in questo documento sono state rese possibili grazie al contributo (diretto e indiretto, accademico e non accademico) di un grande numero di persone di grande talento e generosità. In questo paragrafo vorrei riconoscerne il contributo.
Ho profondamente apprezzato la parte di vita che abbiamo condiviso assieme.

Grazie a mia madre e a mio padre per essere la principale ragione per cui esisto in questo mondo e per non aver mai mancato di farmi sentire che, attraverso gli anni, c'era sempre qualcuno dalla mia parte.

Grazie al mio mentore e supervisore Tommaso, per avermi permesso di lavorare al tuo fianco e d'innamorarmi delle neuroscienze. Sei stato una fonte di grande ispirazione e mi hai insegnato così tante lezioni. Grazie a tutte le persone in laboratorio, insegnanti, collaboratori, colleghi e studenti. In particolare grazie ad Andrea, Alexia, Aurelia, Edda, Elena, Elsa, Fabio, Francesca D., Francesco, Giulia, Laura, Luca, Manuella, Matteo, Paola, Raffaele, Sara e Valentino.

Grazie a tutta la mia famiglia per il loro supporto prezioso e incondizionato. Un grazie in particolare a Lisa, Remo, Alberto, Vittoria, Teo, Medoro, Luciano e Graziella.

Infine, grazie a Francesca. Tu, più di chiunque altro, hai condiviso con me le gioie e i dispiaceri, le preoccupazioni e i sollievi, e hai reso questo sentiero degno di essere percorso.

List of Figures

List of Tables

References

Albrecht, D G and D B Hamilton (July 1982). "Striate cortex of monkey and cat: contrast response function." In: *Journal of Neurophysiology* 48.1. Publisher: American Physiological Society, pp. 217–237. ISSN: 0022-3077. DOI: 10.1152/jn.1982.48.1.217 (cit. on p. 87).

Alexander, Celeste, Kelly S Swanson, George C Fahey Jr, and Keith A Garleb (July 1, 2019). "Perspective: Physiologic Importance of Short-Chain Fatty Acids from Nondigestible Carbohydrate Fermentation". In: *Advances in Nutrition* 10.4, pp. 576–589. ISSN: 2161-8313. DOI: 10.1093/advances/nmz004 (cit. on p. 22).

Amendola, Elena, Yang Zhan, Camilla Mattucci, Enrico Castroflorio, Eleonora Calcagno, Claudia Fuchs, Giuseppina Lonetti, Davide Silingardi, Alexei L. Vyssotski, Dominika Farley, Elisabetta Ciani, Tommaso Pizzorusso, Maurizio Giustetto, and Cornelius T. Gross (May 16, 2014). "Mapping Pathological Phenotypes in a Mouse Model of CDKL5 Disorder". In: *PLOS ONE* 9.5, e91613. ISSN: 1932-6203. DOI: 10.1371/journal.pone.0091613 (cit. on pp. 68, 82, 83, 85).

Ariza, Jeanelle, Haille Rogers, Ezzat Hashemi, Stephen C Noctor, and Verónica Martínez-Cerdeño (Feb. 1, 2018). "The Number of Chandelier and Basket Cells Are Differentially Decreased in Prefrontal Cortex in Autism". In: *Cerebral Cortex* 28.2, pp. 411–420. ISSN: 1047-3211. DOI: 10.1093/cercor/bhw349 (cit. on p. 54).

Baimbridge, K. G. and J. J. Miller (Aug. 12, 1982). "Immunohistochemical localization of calcium-binding protein in the cerebellum, hippocampal formation and olfactory bulb of the rat". In: *Brain Research* 245.2, pp. 223–229. ISSN: 0006-8993. DOI: 10.1016/0006-8993(82)90804-6 (cit. on p. 40).

Baroncelli, L., C. Braschi, M. Spolidoro, T. Begenisic, A. Sale, and L. Maffei (July 2010). "Nurturing brain plasticity: impact of environmental enrichment". In: *Cell Death & Differentiation* 17.7. Number: 7 Publisher: Nature Publishing Group, pp. 1092–1103. ISSN: 1476-5403. DOI: 10.1038/cdd.2009.193 (cit. on pp. 4, 5).

Baroncelli, Laura, Joyce Bonaccorsi, Marco Milanese, Tiziana Bonifacino, Francesco Giribaldi, Ilaria Manno, Maria Cristina Cenni, Nicoletta Berardi, Giambattista Bonanno, Lamberto Maffei, and Alessandro Sale (June 1, 2012). "Enriched experience and recovery from amblyopia in adult rats: Impact of motor, social and sensory components". In: *Neuropharmacology* 62.7, pp. 2388–2397. ISSN: 0028-3908. DOI: 10.1016/j.neuropharm.2012.02.010 (cit. on p. 21).

Bartoletti, Alessandro, Paolo Medini, Nicoletta Berardi, and Lamberto Maffei (Mar. 2004). "Environmental enrichment prevents effects of dark-rearing in the rat visual cortex". In: *Nature Neuroscience* 7.3. Number: 3 Publisher: Nature Publishing Group, pp. 215–216. ISSN: 1546-1726. DOI: 10.1038/nn1201 (cit. on p. 32).

Bastianelli, Enrico (Dec. 1, 2003). "Distribution of calcium-binding proteins in the cerebellum". In: *The Cerebellum* 2.4, pp. 242–262. ISSN: 1473-4230. DOI: 10.1080/14734220310022289 (cit. on p. 41).

Begenisic, Tatjana, Gabriele Sansevero, Laura Baroncelli, Giovanni Cioni, and Alessandro Sale (Oct. 1, 2015). "Early environmental therapy rescues brain development in a mouse model of Down syndrome". In: *Neurobiology of Disease* 82, pp. 409–419. ISSN: 0969-9961. DOI: 10.1016/j.nbd.2015.07.014 (cit. on p. 82).

Bochner, David N., Richard W. Sapp, Jaimie D. Adelson, Siyu Zhang, Hanmi Lee, Maja Djurisic, Josh Syken, Yang Dan, and Carla J. Shatz (Oct. 15, 2014). "Blocking PirB up-regulates spines and functional synapses to unlock visual cortical plasticity and facilitate recovery from amblyopia". In: *Science Translational Medicine* 6.258. Publisher: American Association for the Advancement of Science, 258ra140–258ra140. DOI: 10.1126/scitranslmed.3010157 (cit. on p. 22).

Boehme, Marcus et al. (Aug. 2021). "Microbiota from young mice counteracts selective age-associated behavioral deficits". In: *Nature Aging* 1.8. Number: 8 Publisher: Nature Publishing Group, pp. 666–676. ISSN: 2662-8465. DOI: 10.1038/s43587-021-00093-9 (cit. on p. 5).

Boggio, E. M., L. Pancrazi, M. Gennaro, C. Lo Rizzo, F. Mari, I. Meloni, F. Ariani, A. Panighini, E. Novelli, M. Biagioni, E. Strettoi, J. Hayek, A. Rufa, T. Pizzorusso, A. Renieri, and M. Costa (June 2, 2016). "Visual impairment in FOXG1-mutated individuals and mice". In: *Neuroscience* 324, pp. 496–508. ISSN: 0306-4522. DOI: 10.1016/j.neuroscience.2016.03.027 (cit. on p. 82).

Boggio, Elena Maria, Erich M. Ehlert, Leonardo Lupori, Elizabeth B. Moloney, Fred De Winter, Craig W. Vander Kooi, Laura Baroncelli, Vasilis Mecollari, Bas Blits, James W. Fawcett, Joost Verhaagen, and Tommaso Pizzorusso (Sept. 2019). "Inhibition of Semaphorin3A Promotes Ocular Dominance Plasticity in the Adult Rat Visual Cortex". In: *Molecular Neurobiology* 56.9, pp. 5987–5997. ISSN: 0893-7648, 1559-1182. DOI: 10.1007/s12035-019-1499-0 (cit. on p. 31).

Bonetto, Giulia, David Belin, and Ragnhildur Thóra Káradóttir (Oct. 7, 2021). "Myelin: A gatekeeper of activity-dependent circuit plasticity?" In: *Science* 374.6569. Publisher: American Association for the Advancement of Science, eaba6905. DOI: 10.1126/science.aba6905 (cit. on p. 56).

Bouhours, Brice, Enida Gjoni, Olexiy Kochubey, and Ralf Schneggenburger (Apr. 26, 2017). "Synaptotagmin2 (Syt2) Drives Fast Release Redundantly with Syt1 at the Output Synapses of Parvalbumin-Expressing Inhibitory Neurons". In: *The Journal of Neuroscience: The Official Journal of the Society for Neuroscience* 37.17, pp. 4604–4617. ISSN: 1529-2401. DOI: 10.1523/JNEUROSCI.3736-16.2017 (cit. on p. 50).

El-Boustani, Sami, Jacque P. K. Ip, Vincent Breton-Provencher, Graham W. Knott, Hiroyuki Okuno, Haruhiko Bito, and Mriganka Sur (June 22, 2018). "Locally coordinated synaptic plasticity of visual cortex neurons in vivo". In: *Science* 360.6395. Publisher: American Association for the Advancement of Science, pp. 1349–1354. DOI: 10.1126/science.aao0862 (cit. on p. 22).

El-Boustani, Sami, B. Semihcan Sermet, Georgios Foustoukos, Tess B. Oram, Ofer Yizhar, and Carl C. H. Petersen (July 3, 2020). "Anatomically and functionally distinct thalamocortical inputs to primary and secondary mouse whisker somatosensory cortices". In: *Nature Communications* 11.1, p. 3342. ISSN: 2041-1723. DOI: 10.1038/s41467-020-17087-7 (cit. on p. 56).

Bradbury, Elizabeth J., Lawrence D. F. Moon, Reena J. Popat, Von R. King, Gavin S. Bennett, Preena N. Patel, James W. Fawcett, and Stephen B. McMahon (Apr. 2002). "Chondroitinase ABC promotes functional recovery after spinal cord injury".

In: *Nature* 416.6881. Number: 6881 Publisher: Nature Publishing Group, pp. 636–640. ISSN: 1476-4687. DOI: 10.1038/416636a (cit. on p. 31).

Braniste, Viorica, Maha Al-Asmakh, Czeslawa Kowal, Farhana Anuar, Afrouz Abbaspour, Miklós Tóth, Agata Korecka, Nadja Bakocevic, Lai Guan Ng, Parag Kundu, Balázs Gulyás, Christer Halldin, Kjell Hultenby, Harriet Nilsson, Hans Hebert, Bruce T. Volpe, Betty Diamond, and Sven Pettersson (Nov. 19, 2014). "The gut microbiota influences blood-brain barrier permeability in mice". In: *Science Translational Medicine* 6.263. Publisher: American Association for the Advancement of Science, 263ra158–263ra158. DOI: 10.1126/scitranslmed.3009759 (cit. on pp. 5, 22).

Browne, Caroline A., Katherine Conant, Amy W. Lasek, and Juan Nacher (2022). "Editorial: Perineuronal Nets as Therapeutic Targets for the Treatment of Neuropsychiatric Disorders". In: *Frontiers in Synaptic Neuroscience* 14. ISSN: 1663-3563 (cit. on p. 56).

Buffington, Shelly A., Gonzalo Viana Di Prisco, Thomas A. Auchtung, Nadim J. Ajami, Joseph F. Petrosino, and Mauro Costa-Mattioli (June 16, 2016). "Microbial Reconstitution Reverses Maternal Diet-Induced Social and Synaptic Deficits in Offspring". In: *Cell* 165.7, pp. 1762–1775. ISSN: 0092-8674. DOI: 10.1016/j.cell.2016.06.001 (cit. on p. 5).

Buffington, Shelly A., Sean W. Dooling, Martina Sgritta, Cecilia Noecker, Oscar D. Murillo, Daniela F. Felice, Peter J. Turnbaugh, and Mauro Costa-Mattioli (Apr. 1, 2021). "Dissecting the contribution of host genetics and the microbiome in complex behaviors". In: *Cell* 184.7, 1740–1756.e16. ISSN: 0092-8674. DOI: 10.1016/j.cell.2021.02.009 (cit. on p. 5).

Bukalo, O., M. Schachner, and A. Dityatev (May 30, 2007). "Hippocampal Metaplasticity Induced by Deficiency in the Extracellular Matrix Glycoprotein Tenascin-R". In: *Journal of Neuroscience* 27.22, pp. 6019–6028. ISSN: 0270-6474, 1529-2401. DOI: 10.1523/JNEUROSCI.1022-07.2007 (cit. on p. 32).

Cabungcal, Jan-Harry, Pascal Steullet, Hirofumi Morishita, Rudolf Kraftsik, Michel Cuenod, Takao K. Hensch, and Kim Q. Do (May 28, 2013). "Perineuronal nets protect fast-spiking interneurons against oxidative stress". In: *Proceedings of the National Academy of Sciences* 110.22. Publisher: Proceedings of the National Academy of Sciences, pp. 9130–9135. DOI: 10.1073/pnas.1300454110 (cit. on p. 31).

Callahan, Benjamin J., Paul J. McMurdie, Michael J. Rosen, Andrew W. Han, Amy Jo A. Johnson, and Susan P. Holmes (July 2016). "DADA2: High-resolution sample inference from Illumina amplicon data". In: *Nature Methods* 13.7. Number: 7 Publisher: Nature Publishing Group, pp. 581–583. ISSN: 1548-7105. DOI: 10.1038/nmeth.3869 (cit. on p. 25).

Cancedda, Laura, Elena Putignano, Alessandro Sale, Alessandro Viegi, Nicoletta Berardi, and Lamberto Maffei (May 19, 2004). "Acceleration of Visual System Development by Environmental Enrichment". In: *Journal of Neuroscience* 24.20. Publisher: Society for Neuroscience Section: Behavioral/Systems/Cognitive, pp. 4840–4848. ISSN: 0270-6474, 1529-2401. DOI: 10.1523/JNEUROSCI.0845-04.2004 (cit. on p. 5).

Cang, Jianhua, Valery A. Kalatsky, Siegrid Löwel, and Michael P. Stryker (Sept. 2005). "Optical imaging of the intrinsic signal as a measure of cortical plasticity in the mouse". In: *Visual Neuroscience* 22.5. Publisher: Cambridge University Press, pp. 685–691. ISSN: 1469-8714, 0952-5238. DOI: 10.1017/S0952523805225178 (cit. on pp. 27, 86).

Caporaso, J. Gregory et al. (May 2010). "QIIME allows analysis of high-throughput community sequencing data". In: *Nature Methods* 7.5. Number: 5 Publisher: Nature

Publishing Group, pp. 335–336. ISSN: 1548-7105. DOI: 10.1038/nmeth.f.303 (cit. on p. 26).

Carstens, Kelly E., Mary L. Phillips, Lucas Pozzo-Miller, Richard J. Weinberg, and Serena M. Dudek (June 8, 2016). "Perineuronal Nets Suppress Plasticity of Excitatory Synapses on CA2 Pyramidal Neurons". In: *Journal of Neuroscience* 36.23. Publisher: Society for Neuroscience Section: Articles, pp. 6312–6320. ISSN: 0270-6474, 1529-2401. DOI: 10.1523/JNEUROSCI.0245-16.2016 (cit. on pp. 31, 39).

Carulli, Daniela, Robin Broersen, Fred de Winter, Elizabeth M. Muir, Maja Mešković, Matthijs de Waal, Sharon de Vries, Henk-Jan Boele, Cathrin B. Canto, Chris I. De Zeeuw, and Joost Verhaagen (Mar. 24, 2020). "Cerebellar plasticity and associative memories are controlled by perineuronal nets". In: *Proceedings of the National Academy of Sciences of the United States of America* 117.12, pp. 6855–6865. ISSN: 1091-6490. DOI: 10.1073/pnas.1916163117 (cit. on p. 31).

Carulli, Daniela, Tommaso Pizzorusso, Jessica C. F. Kwok, Elena Putignano, Andrea Poli, Serhiy Forostyak, Melissa R. Andrews, Sathyaseelan S. Deepa, Tibor T. Glant, and James W. Fawcett (Aug. 1, 2010). "Animals lacking link protein have attenuated perineuronal nets and persistent plasticity". In: *Brain* 133.8, pp. 2331–2347. ISSN: 0006-8950. DOI: 10.1093/brain/awq145 (cit. on pp. 31, 48).

Chakravarthy, Sridhara, M. Hadi Saiepour, Matthew Bence, Sean Perry, Robin Hartman, Jonathan J. Couey, Huibert D. Mansvelder, and Christiaan N. Levelt (Jan. 24, 2006). "Postsynaptic TrkB signaling has distinct roles in spine maintenance in adult visual cortex and hippocampus". In: *Proceedings of the National Academy of Sciences* 103.4. Publisher: Proceedings of the National Academy of Sciences, pp. 1071–1076. DOI: 10.1073/pnas.0506305103 (cit. on p. 22).

Champagne-Jorgensen, Kevin, Wolfgang A. Kunze, Paul Forsythe, John Bienenstock, and Karen-Anne McVey Neufeld (Mar. 1, 2019). "Antibiotics and the nervous system: More than just the microbes?" In: *Brain, Behavior, and Immunity* 77, pp. 7–15. ISSN: 0889-1591. DOI: 10.1016/j.bbi.2018.12.014 (cit. on p. 9).

Cheadle, Lucas, Samuel A. Rivera, Jasper S. Phelps, Katelin A. Ennis, Beth Stevens, Linda C. Burkly, Wei-Chung Allen Lee, and Michael E. Greenberg (Nov. 11, 2020). "Sensory Experience Engages Microglia to Shape Neural Connectivity through a Non-Phagocytic Mechanism". In: *Neuron* 108.3, 451–468.e9. ISSN: 0896-6273. DOI: 10.1016/j.neuron.2020.08.002 (cit. on p. 22).

Chen, Qian, Yong-Chuan Zhu, Jing Yu, Sheng Miao, Jing Zheng, Li Xu, Yang Zhou, Dan Li, Chi Zhang, Jiong Tao, and Zhi-Qi Xiong (Sept. 22, 2010). "CDKL5, a Protein Associated with Rett Syndrome, Regulates Neuronal Morphogenesis via Rac1 Signaling". In: *Journal of Neuroscience* 30.38. Publisher: Society for Neuroscience Section: Articles, pp. 12777–12786. ISSN: 0270-6474, 1529-2401. DOI: 10.1523/JNEUROSCI.1102-10.2010 (cit. on pp. 68, 82).

Chow, A., A. Erisir, C. Farb, M. S. Nadal, A. Ozaita, D. Lau, E. Welker, and B. Rudy (Nov. 1, 1999). "K+ Channel Expression Distinguishes Subpopulations of Parvalbumin- and Somatostatin-Containing Neocortical Interneurons". In: *The Journal of Neuroscience* 19.21, pp. 9332–9345. ISSN: 0270-6474. DOI: 10.1523/JNEUROSCI.19-21-09332.1999 (cit. on p. 49).

Christensen, Ane Charlotte, Kristian Kinden Lensjø, Mikkel Elle Lepperød, Svenn-Arne Dragly, Halvard Sutterud, Jan Sigurd Blackstad, Marianne Fyhn, and Torkel Hafting (Jan. 11, 2021). "Perineuronal nets stabilize the grid cell network". In: *Nature*

Communications 12.1, p. 253. ISSN: 2041-1723. DOI: 10.1038/s41467-020-20241-w (cit. on p. 31).

Chu, Coco et al. (Oct. 2019). "The microbiota regulate neuronal function and fear extinction learning". In: *Nature* 574.7779. Number: 7779 Publisher: Nature Publishing Group, pp. 543–548. ISSN: 1476-4687. DOI: 10.1038/s41586-019-1644-y (cit. on p. 21).

Ciampi, Luca, Fabio Carrara, Valentino Totaro, Raffaele Mazziotti, Leonardo Lupori, Carlos Santiago, Giuseppe Amato, Tommaso Pizzorusso, and Claudio Gennaro (Aug. 1, 2022). "Learning to count biological structures with raters' uncertainty". In: *Medical Image Analysis* 80, p. 102500. ISSN: 1361-8415. DOI: 10.1016/j.media.2022.102500 (cit. on pp. 34, 60).

Cicconet, Marcelo and Daniel R. Hochbaum (Sept. 25, 2019). *A Supervised, Symmetry-Driven, GUI Toolkit for Mouse Brain Stack Registration and Plane Assignment*. preprint. Bioinformatics. DOI: 10.1101/781880 (cit. on p. 61).

Claudi, Federico and Luigi Petrucco (Jan. 22, 2022). *brainglobe/bg-heatmaps:* DOI: 10.5281/zenodo.5891814 (cit. on p. 65).

Claudi, Federico, Adam L Tyson, Luigi Petrucco, Troy W Margrie, Ruben Portugues, and Tiago Branco (Mar. 19, 2021). "Visualizing anatomically registered data with brainrender". In: *eLife* 10. Ed. by Mackenzie W Mathis, Kate M Wassum, and Juan Nunez-Iglesias. Publisher: eLife Sciences Publications, Ltd, e65751. ISSN: 2050-084X. DOI: 10.7554/eLife.65751 (cit. on p. 65).

Cohen, Jacob (July 1, 1988). *Statistical Power Analysis for the Behavioral Sciences*. 2nd ed. New York: Routledge. 567 pp. ISBN: 978-0-203-77158-7. DOI: 10.4324/9780203771587 (cit. on p. 79).

Cope, Elise C., Anna D. Zych, Nicole J. Katchur, Renée C. Waters, Blake J. Laham, Emma J. Diethorn, Christin Y. Park, William R. Meara, and Elizabeth Gould (June 28, 2021). "Atypical perineuronal nets in the CA2 region interfere with social memory in a mouse model of social dysfunction". In: *Molecular Psychiatry*. Publisher: Nature Publishing Group, pp. 1–12. ISSN: 1476-5578. DOI: 10.1038/s41380-021-01174-2 (cit. on p. 31).

Cortes, Corinna and Vladimir Vapnik (Sept. 1, 1995). "Support-vector networks". In: *Machine Learning* 20.3, pp. 273–297. ISSN: 1573-0565. DOI: 10.1007/BF00994018 (cit. on p. 87).

Cowan, Caitlin S. M., Timothy G. Dinan, and John F. Cryan (2020). "Annual Research Review: Critical windows – the microbiota–gut–brain axis in neurocognitive development". In: *Journal of Child Psychology and Psychiatry* 61.3, pp. 353–371. ISSN: 1469-7610. DOI: 10.1111/jcpp.13156 (cit. on p. 5).

Dalile, Boushra, Lukas Van Oudenhove, Bram Vervliet, and Kristin Verbeke (Aug. 2019). "The role of short-chain fatty acids in microbiota–gut–brain communication". In: *Nature Reviews Gastroenterology & Hepatology* 16.8. Number: 8 Publisher: Nature Publishing Group, pp. 461–478. ISSN: 1759-5053. DOI: 10.1038/s41575-019-0157-3 (cit. on pp. 17, 23).

Darch, Henry T., Michael K. Collins, Kenneth J. O'Riordan, and John F. Cryan (2021). "Microbial memories: Sex-dependent impact of the gut microbiome on hippocampal plasticity". In: *European Journal of Neuroscience* 54.4, pp. 5235–5244. ISSN: 1460-9568. DOI: 10.1111/ejn.15119 (cit. on p. 5).

Dauth, Stephanie, Thomas Grevesse, Harry Pantazopoulos, Patrick H. Campbell, Ben M. Maoz, Sabina Berretta, and Kevin Kit Parker (2016). "Extracellular matrix protein expression is brain region dependent". In: *Journal of Comparative Neurology* 524.7, pp. 1309–1336. ISSN: 1096-9861. DOI: 10.1002/cne.23965 (cit. on pp. 31, 32, 48).

Deepa, Sarama Sathyaseelan, Daniela Carulli, Clare Galtrey, Kate Rhodes, Junko Fukuda, Tadahisa Mikami, Kazuyuki Sugahara, and James W. Fawcett (June 30, 2006). "Composition of Perineuronal Net Extracellular Matrix in Rat Brain: A DIFFERENT DISACCHARIDE COMPOSITION FOR THE NET-ASSOCIATED PROTEOGLYCANS *". In: *Journal of Biological Chemistry* 281.26. Publisher: Elsevier, pp. 17789–17800. ISSN: 0021-9258, 1083-351X. DOI: 10.1074/jbc.M600544200 (cit. on p. 32).

Della Sala, Grazia, Elena Putignano, Gabriele Chelini, Riccardo Melani, Eleonora Calcagno, Gian Michele Ratto, Elena Amendola, Cornelius T. Gross, Maurizio Giustetto, and Tommaso Pizzorusso (Aug. 15, 2016). "Dendritic Spine Instability in a Mouse Model of CDKL5 Disorder Is Rescued by Insulin-like Growth Factor 1". In: *Biological Psychiatry*. Molecular Mechanisms of Microcircuit Dysfunction in Schizophrenia 80.4, pp. 302–311. ISSN: 0006-3223. DOI: 10.1016/j.biopsych.2015.08.028 (cit. on pp. 68, 83).

Desbonnet, Lieve, Gerard Clarke, Alexander Traplin, Orla O'Sullivan, Fiona Crispie, Rachel D. Moloney, Paul D. Cotter, Timothy G. Dinan, and John F. Cryan (Aug. 1, 2015). "Gut microbiota depletion from early adolescence in mice: Implications for brain and behaviour". In: *Brain, Behavior, and Immunity* 48, pp. 165–173. ISSN: 0889-1591. DOI: 10.1016/j.bbi.2015.04.004 (cit. on p. 21).

Donato, Flavio, Ananya Chowdhury, Maria Lahr, and Pico Caroni (Feb. 18, 2015). "Early- and Late-Born Parvalbumin Basket Cell Subpopulations Exhibiting Distinct Regulation and Roles in Learning". In: *Neuron* 85.4, pp. 770–786. ISSN: 0896-6273. DOI: 10.1016/j.neuron.2015.01.011 (cit. on pp. 41, 55).

Donato, Flavio, Santiago Belluco Rompani, and Pico Caroni (Dec. 2013). "Parvalbumin-expressing basket-cell network plasticity induced by experience regulates adult learning". In: *Nature* 504.7479. Number: 7479 Publisher: Nature Publishing Group, pp. 272–276. ISSN: 1476-4687. DOI: 10.1038/nature12866 (cit. on pp. 32, 41, 55).

Durand, Severine, Annarita Patrizi, Kathleen B. Quast, Lea Hachigian, Roman Pavlyuk, Alka Saxena, Piero Carninci, Takao K. Hensch, and Michela Fagiolini (Dec. 20, 2012). "NMDA Receptor Regulation Prevents Regression of Visual Cortical Function in the Absence of Mecp2". In: *Neuron* 76.6, pp. 1078–1090. ISSN: 0896-6273. DOI: 10.1016/j.neuron.2012.12.004 (cit. on pp. 68, 82).

Erny, Daniel, Anna Lena Hrabě de Angelis, Diego Jaitin, Peter Wieghofer, Ori Staszewski, Eyal David, Hadas Keren-Shaul, Tanel Mahlakoiv, Kristin Jakobshagen, Thorsten Buch, Vera Schwierzeck, Olaf Utermöhlen, Eunyoung Chun, Wendy S. Garrett, Kathy D. McCoy, Andreas Diefenbach, Peter Staeheli, Bärbel Stecher, Ido Amit, and Marco Prinz (July 2015). "Host microbiota constantly control maturation and function of microglia in the CNS". In: *Nature Neuroscience* 18.7. Number: 7 Publisher: Nature Publishing Group, pp. 965–977. ISSN: 1546-1726. DOI: 10.1038/nn.4030 (cit. on pp. 5, 22, 25).

Espinosa, J. Sebastian and Michael P. Stryker (July 26, 2012). "Development and Plasticity of the Primary Visual Cortex". In: *Neuron* 75.2, pp. 230–249. ISSN: 0896-6273. DOI: 10.1016/j.neuron.2012.06.009 (cit. on p. 71).

Evans, Christian C., Kathy J. LePard, Jeff W. Kwak, Mary C. Stancukas, Samantha Laskowski, Joseph Dougherty, Laura Moulton, Adam Glawe, Yunwei Wang, Vanessa

Leone, Dionysios A. Antonopoulos, Dan Smith, Eugene B. Chang, and Mae J. Ciancio (Mar. 26, 2014). "Exercise Prevents Weight Gain and Alters the Gut Microbiota in a Mouse Model of High Fat Diet-Induced Obesity". In: *PLOS ONE* 9.3. Publisher: Public Library of Science, e92193. ISSN: 1932-6203. DOI: 10.1371/journal.pone.0092193 (cit. on p. 21).

Faini, Giulia, Andrea Aguirre, Silvia Landi, Didi Lamers, Tommaso Pizzorusso, Gian Michele Ratto, Charlotte Deleuze, and Alberto Bacci (Dec. 18, 2018). "Perineuronal nets control visual input via thalamic recruitment of cortical PV interneurons". In: *eLife* 7. Ed. by Marlene Bartos and Gary L Westbrook. Publisher: eLife Sciences Publications, Ltd, e41520. ISSN: 2050-084X. DOI: 10.7554/eLife.41520 (cit. on pp. 47, 56).

Faria, Omar de, Helena Pivonkova, Balazs Varga, Sebastian Timmler, Kimberley Anne Evans, and Ragnhildur Thóra Káradóttir (Nov. 2021). "Periods of synchronized myelin changes shape brain function and plasticity". In: *Nature Neuroscience* 24.11, pp. 1508–1521. ISSN: 1546-1726. DOI: 10.1038/s41593-021-00917-2 (cit. on p. 56).

Fawcett, James W., Toshitaka Oohashi, and Tommaso Pizzorusso (Aug. 2019). "The roles of perineuronal nets and the perinodal extracellular matrix in neuronal function". In: *Nature Reviews. Neuroscience* 20.8, pp. 451–465. ISSN: 1471-0048. DOI: 10.1038/s41583-019-0196-3 (cit. on pp. 31, 32, 39, 48, 54, 55).

Fehr, Stephanie, Meredith Wilson, Jenny Downs, Simon Williams, Alessandra Murgia, Stefano Sartori, Marilena Vecchi, Gladys Ho, Roberta Polli, Stavroula Psoni, Xinhua Bao, Nick de Klerk, Helen Leonard, and John Christodoulou (Mar. 2013). "The CDKL5 disorder is an independent clinical entity associated with early-onset encephalopathy". In: *European Journal of Human Genetics* 21.3. Number: 3 Publisher: Nature Publishing Group, pp. 266–273. ISSN: 1476-5438. DOI: 10.1038/ejhg.2012.156 (cit. on p. 68).

Feng, Guoping, Rebecca H. Mellor, Michael Bernstein, Cynthia Keller-Peck, Quyen T. Nguyen, Mia Wallace, Jeanne M. Nerbonne, Jeff W. Lichtman, and Joshua R. Sanes (Oct. 1, 2000). "Imaging Neuronal Subsets in Transgenic Mice Expressing Multiple Spectral Variants of GFP". In: *Neuron* 28.1, pp. 41–51. ISSN: 0896-6273. DOI: 10.1016/S0896-6273(00)00084-2 (cit. on pp. 14, 24).

Fischer, Andre, Farahnaz Sananbenesi, Xinyu Wang, Matthew Dobbin, and Li-Huei Tsai (May 2007). "Recovery of learning and memory is associated with chromatin remodelling". In: *Nature* 447.7141. Number: 7141 Publisher: Nature Publishing Group, pp. 178–182. ISSN: 1476-4687. DOI: 10.1038/nature05772 (cit. on p. 20).

Fishell, Gordon (2008). "Perspectives on the Developmental Origins of Cortical Interneuron Diversity". In: *Cortical Development: Genes and Genetic Abnormalities*. _eprint: https://onlinelibrary.wiley.com/doi/pdf/10.1002/9780470994030.ch3. John Wiley & Sons, Ltd, pp. 21–44. ISBN: 978-0-470-99403-0. DOI: 10.1002/9780470994030.ch3 (cit. on p. 55).

Forsythe, Paul and John Bienenstock (Sept. 2016). "Microbiota and behaviour: visiting the sins of the mother". In: *Nature Reviews Gastroenterology & Hepatology* 13.9. Number: 9 Publisher: Nature Publishing Group, pp. 502–504. ISSN: 1759-5053. DOI: 10.1038/nrgastro.2016.122 (cit. on p. 5).

Freitas Dotto, Patrícia de, Nívea Nunes Cavascan, Adriana Berezovsky, Paula Yuri Sacai, Daniel Martins Rocha, Josenilson Martins Pereira, and Solange Rios Salomão (Mar. 1, 2014). "Sweep visually evoked potentials and visual findings in children with West

syndrome". In: *European Journal of Paediatric Neurology* 18.2, pp. 201–210. ISSN: 1090-3798. DOI: 10.1016/j.ejpn.2013.11.008 (cit. on p. 82).

Fuchs, Claudia, Roberto Rimondini, Rocchina Viggiano, Stefania Trazzi, Marianna De Franceschi, Renata Bartesaghi, and Elisabetta Ciani (Oct. 1, 2015). "Inhibition of GSK3β rescues hippocampal development and learning in a mouse model of CDKL5 disorder". In: *Neurobiology of Disease* 82, pp. 298–310. ISSN: 0969-9961. DOI: 10.1016/j.nbd.2015.06.018 (cit. on p. 82).

Gacias, Mar, Sevasti Gaspari, Patricia-Mae G Santos, Sabrina Tamburini, Monica Andrade, Fan Zhang, Nan Shen, Vladimir Tolstikov, Michael A Kiebish, Jeffrey L Dupree, Venetia Zachariou, Jose C Clemente, and Patrizia Casaccia (Apr. 20, 2016). "Microbiota-driven transcriptional changes in prefrontal cortex override genetic differences in social behavior". In: *eLife* 5. Ed. by Peggy Mason. Publisher: eLife Sciences Publications, Ltd, e13442. ISSN: 2050-084X. DOI: 10.7554/eLife.13442 (cit. on pp. 5, 21).

Galtrey, Clare M., Jessica C. F. Kwok, Daniela Carulli, Kate E. Rhodes, and James W. Fawcett (2008). "Distribution and synthesis of extracellular matrix proteoglycans, hyaluronan, link proteins and tenascin-R in the rat spinal cord". In: *European Journal of Neuroscience* 27.6. _eprint: https://onlinelibrary.wiley.com/doi/pdf/10.1111/j.1460-9568.2008.06108.x, pp. 1373–1390. ISSN: 1460-9568. DOI: 10.1111/j.1460-9568.2008.06108.x (cit. on pp. 31, 54).

Gogolla, Nadine, Pico Caroni, Andreas Lüthi, and Cyril Herry (Sept. 4, 2009). "Perineuronal Nets Protect Fear Memories from Erasure". In: *Science* 325.5945, pp. 1258–1261. ISSN: 0036-8075, 1095-9203. DOI: 10.1126/science.1174146 (cit. on p. 31).

Gorski, Jessica A., Tiffany Talley, Mengsheng Qiu, Luis Puelles, John L. R. Rubenstein, and Kevin R. Jones (Aug. 1, 2002). "Cortical Excitatory Neurons and Glia, But Not GABAergic Neurons, Are Produced in the Emx1-Expressing Lineage". In: *Journal of Neuroscience* 22.15. Publisher: Society for Neuroscience Section: BRIEF COMMUNICATION, pp. 6309–6314. ISSN: 0270-6474, 1529-2401. DOI: 10.1523/JNEUROSCI.22-15-06309.2002 (cit. on pp. 77, 85).

Greifzu, Franziska, Justyna Pielecka-Fortuna, Evgenia Kalogeraki, Katja Krempler, Plinio D. Favaro, Oliver M. Schlüter, and Siegrid Löwel (Jan. 21, 2014). "Environmental enrichment extends ocular dominance plasticity into adulthood and protects from stroke-induced impairments of plasticity". In: *Proceedings of the National Academy of Sciences* 111.3. Publisher: Proceedings of the National Academy of Sciences, pp. 1150–1155. DOI: 10.1073/pnas.1313385111 (cit. on pp. 4, 9).

Harris, Charles R. et al. (Sept. 2020). "Array programming with NumPy". In: *Nature* 585.7825. Number: 7825 Publisher: Nature Publishing Group, pp. 357–362. ISSN: 1476-4687. DOI: 10.1038/s41586-020-2649-2 (cit. on p. 61).

Harrison, Thomas C., Albrecht Sigler, and Timothy H. Murphy (Sept. 15, 2009). "Simple and cost-effective hardware and software for functional brain mapping using intrinsic optical signal imaging". In: *Journal of Neuroscience Methods* 182.2, pp. 211–218. ISSN: 0165-0270. DOI: 10.1016/j.jneumeth.2009.06.021 (cit. on p. 86).

Härtig, Wolfgang, Amin Derouiche, Klaus Welt, Kurt Brauer, Jens Grosche, Michael Mäder, Andreas Reichenbach, and Gert Brückner (Sept. 18, 1999). "Cortical neurons immunoreactive for the potassium channel Kv3.1b subunit are predominantly surrounded by perineuronal nets presumed as a buffering system for cations". In: *Brain*

Research 842.1, pp. 15–29. ISSN: 0006-8993. DOI: 10.1016/S0006-8993(99)01784-9 (cit. on p. 31).

Hector, Ralph D., Owen Dando, Nicoletta Landsberger, Charlotte Kilstrup-Nielsen, Peter C. Kind, Mark E. S. Bailey, and Stuart R. Cobb (June 17, 2016). "Characterisation of CDKL5 Transcript Isoforms in Human and Mouse". In: *PLOS ONE* 11.6. Publisher: Public Library of Science, e0157758. ISSN: 1932-6203. DOI: 10.1371/journal.pone.0157758 (cit. on pp. 68, 77, 82).

Heimel, J. Alexander, Robin J. Hartman, Josephine M. Hermans, and Christiaan N. Levelt (2007). "Screening mouse vision with intrinsic signal optical imaging". In: *European Journal of Neuroscience* 25.3, pp. 795–804. ISSN: 1460-9568. DOI: 10.1111/j.1460-9568.2007.05333.x (cit. on pp. 27, 86).

Held-Feindt, Janka, Elke Bernedo Paredes, Ulrike Blömer, Constanze Seidenbecher, Andreas M. Stark, H. Maximilian Mehdorn, and Rolf Mentlein (Jan. 1, 2006). "Matrix-degrading proteases ADAMTS4 and ADAMTS5 (disintegrins and metalloproteinases with thrombospondin motifs 4 and 5) are expressed in human glioblastomas". In: *International Journal of Cancer* 118.1, pp. 55–61. ISSN: 0020-7136. DOI: 10.1002/ijc.21258 (cit. on p. 48).

Hendry, S. H., E. G. Jones, S. Hockfield, and R. D. McKay (Feb. 1, 1988). "Neuronal populations stained with the monoclonal antibody Cat-301 in the mammalian cerebral cortex and thalamus". In: *Journal of Neuroscience* 8.2. Publisher: Society for Neuroscience Section: Articles, pp. 518–542. ISSN: 0270-6474, 1529-2401. DOI: 10.1523/JNEUROSCI.08-02-00518.1988 (cit. on p. 31).

Hensch, Takao K. (Nov. 2005). "Critical period plasticity in local cortical circuits". In: *Nature Reviews Neuroscience* 6.11. Number: 11 Publisher: Nature Publishing Group, pp. 877–888. ISSN: 1471-0048. DOI: 10.1038/nrn1787 (cit. on p. 4).

Higarza, Sara G., Silvia Arboleya, Jorge L. Arias, Miguel Gueimonde, and Natalia Arias (Jan. 1, 2021). "Akkermansia muciniphila and environmental enrichment reverse cognitive impairment associated with high-fat high-cholesterol consumption in rats". In: *Gut Microbes* 13.1, p. 1880240. ISSN: 1949-0976. DOI: 10.1080/19490976.2021.1880240 (cit. on p. 21).

Hoban, A. E., R. M. Stilling, F. J. Ryan, F. Shanahan, T. G. Dinan, M. J. Claesson, G. Clarke, and J. F. Cryan (Apr. 2016). "Regulation of prefrontal cortex myelination by the microbiota". In: *Translational Psychiatry* 6.4. Number: 4 Publisher: Nature Publishing Group, e774–e774. ISSN: 2158-3188. DOI: 10.1038/tp.2016.42 (cit. on p. 5).

Hofer, Sonja B., Thomas D. Mrsic-Flogel, Tobias Bonhoeffer, and Mark Hübener (Jan. 2009). "Experience leaves a lasting structural trace in cortical circuits". In: *Nature* 457.7227. Number: 7227 Publisher: Nature Publishing Group, pp. 313–317. ISSN: 1476-4687. DOI: 10.1038/nature07487 (cit. on p. 22).

Holtmaat, Anthony, Tobias Bonhoeffer, David K. Chow, Jyoti Chuckowree, Vincenzo De Paola, Sonja B. Hofer, Mark Hübener, Tara Keck, Graham Knott, Wei-Chung A. Lee, Ricardo Mostany, Tom D. Mrsic-Flogel, Elly Nedivi, Carlos Portera-Cailliau, Karel Svoboda, Joshua T. Trachtenberg, and Linda Wilbrecht (Aug. 2009). "Long-term, high-resolution imaging in the mouse neocortex through a chronic cranial window". In: *Nature Protocols* 4.8. Number: 8 Publisher: Nature Publishing Group, pp. 1128–1144. ISSN: 1750-2799. DOI: 10.1038/nprot.2009.89 (cit. on pp. 11, 22, 28).

Holtmaat, Anthony J. G. D., Joshua T. Trachtenberg, Linda Wilbrecht, Gordon M. Shepherd, Xiaoqun Zhang, Graham W. Knott, and Karel Svoboda (Jan. 20, 2005). "Transient and Persistent Dendritic Spines in the Neocortex In Vivo". In: *Neuron* 45.2, pp. 279–291. ISSN: 0896-6273. DOI: 10.1016/j.neuron.2005.01.003 (cit. on p. 29).

Hong, Soyon, Lasse Dissing-Olesen, and Beth Stevens (Feb. 1, 2016). "New insights on the role of microglia in synaptic pruning in health and disease". In: *Current Opinion in Neurobiology*. Neurobiology of disease 36, pp. 128–134. ISSN: 0959-4388. DOI: 10.1016/j.conb.2015.12.004 (cit. on p. 22).

Hsiao, Elaine Y., Sara W. McBride, Sophia Hsien, Gil Sharon, Embriette R. Hyde, Tyler McCue, Julian A. Codelli, Janet Chow, Sarah E. Reisman, Joseph F. Petrosino, Paul H. Patterson, and Sarkis K. Mazmanian (Dec. 19, 2013). "Microbiota Modulate Behavioral and Physiological Abnormalities Associated with Neurodevelopmental Disorders". In: *Cell* 155.7, pp. 1451–1463. ISSN: 0092-8674. DOI: 10.1016/j.cell.2013.11.024 (cit. on p. 5).

Hübener, Mark and Tobias Bonhoeffer (Nov. 6, 2014). "Neuronal Plasticity: Beyond the Critical Period". In: *Cell* 159.4, pp. 727–737. ISSN: 0092-8674. DOI: 10.1016/j.cell.2014.10.035 (cit. on p. 4).

Hunter, John D. (May 2007). "Matplotlib: A 2D Graphics Environment". In: *Computing in Science & Engineering* 9.3. Conference Name: Computing in Science & Engineering, pp. 90–95. ISSN: 1558-366X. DOI: 10.1109/MCSE.2007.55 (cit. on p. 65).

Hunyadi, Andrea, Botond Gaál, Clara Matesz, Zoltan Meszar, Markus Morawski, Katja Reimann, David Lendvai, Alan Alpar, Ildikó Wéber, and Éva Rácz (Jan. 2020). "Distribution and classification of the extracellular matrix in the olfactory bulb". In: *Brain Structure and Function* 225.1, pp. 321–344. ISSN: 1863-2653, 1863-2661. DOI: 10.1007/s00429-019-02010-8 (cit. on pp. 55, 60).

Jaini, K. Anil and Farshid Farrokhnia (1991). "Unsupervised texture segmentation using Gabor filters". In: 24.12, pp. 1167–1186. ISSN: 0031-3203. DOI: https://doi.org/10.1016/0031-3203(91)90143-S (cit. on p. 61).

Jung, Christian K.E. and Jochen Herms (Feb. 2014). "Structural Dynamics of Dendritic Spines are Influenced by an Environmental Enrichment: An In Vivo Imaging Study". In: *Cerebral Cortex* 24.2, pp. 377–384. ISSN: 1460-2199, 1047-3211. DOI: 10.1093/cercor/bhs317 (cit. on pp. 14, 22).

Kang, Silvia S., Patricio R. Jeraldo, Aishe Kurti, Margret E. Berg Miller, Marc D. Cook, Keith Whitlock, Nigel Goldenfeld, Jeffrey A. Woods, Bryan A. White, Nicholas Chia, and John D. Fryer (Sept. 13, 2014). "Diet and exercise orthogonally alter the gut microbiome and reveal independent associations with anxiety and cognition". In: *Molecular Neurodegeneration* 9.1, p. 36. ISSN: 1750-1326. DOI: 10.1186/1750-1326-9-36 (cit. on p. 21).

Kempermann, Gerd (Apr. 2019). "Environmental enrichment, new neurons and the neurobiology of individuality". In: *Nature Reviews Neuroscience* 20.4. Number: 4 Publisher: Nature Publishing Group, pp. 235–245. ISSN: 1471-0048. DOI: 10.1038/s41583-019-0120-x (cit. on pp. 4, 5).

Kim, Yongsoo, Guangyu Robert Yang, Kith Pradhan, Kannan Umadevi Venkataraju, Mihail Bota, Luis Carlos García del Molino, Greg Fitzgerald, Keerthi Ram, Miao He, Jesse Maurica Levine, Partha Mitra, Z. Josh Huang, Xiao-Jing Wang, and Pavel Osten (Oct. 2017). "Brain-wide Maps Reveal Stereotyped Cell-Type-Based Cortical

Architecture and Subcortical Sexual Dimorphism". In: *Cell* 171.2, 456–469.e22. ISSN: 00928674. DOI: 10.1016/j.cell.2017.09.020 (cit. on p. 48).

Klimczak, Patrycja, Arianna Rizzo, Esther Castillo-Gómez, Marta Perez-Rando, Yaiza Gramuntell, Marc Beltran, and Juan Nacher (2021). "Parvalbumin Interneurons and Perineuronal Nets in the Hippocampus and Retrosplenial Cortex of Adult Male Mice After Early Social Isolation Stress and Perinatal NMDA Receptor Antagonist Treatment". In: *Frontiers in Synaptic Neuroscience* 13, p. 733989. ISSN: 1663-3563. DOI: 10.3389/fnsyn.2021.733989 (cit. on p. 56).

Köppe, Gerlinde, Gert Brückner, Kurt Brauer, Wolfgang Härtig, and Volker Bigl (Mar. 1, 1997). "Developmental patterns of proteoglycan-containing extracellular matrix in perineuronal nets and neuropil of the postnatal rat brain". In: *Cell and Tissue Research* 288.1, pp. 33–41. ISSN: 1432-0878. DOI: 10.1007/s004410050790 (cit. on p. 31).

Kwok, Jessica C. F., Daniela Carulli, and James W. Fawcett (2010). "In vitro modeling of perineuronal nets: hyaluronan synthase and link protein are necessary for their formation and integrity". In: *Journal of Neurochemistry* 114.5. _eprint: https://onlinelibrary.wiley.com/doi/pdf/10.1111/j.1471-4159.2010.06878.x, pp. 1447–1459. ISSN: 1471-4159. DOI: 10.1111/j.1471-4159.2010.06878.x (cit. on pp. 31, 48).

LeBlanc, Jocelyn J., Geneva DeGregorio, Eleonora Centofante, Vanessa K. Vogel-Farley, Katherine Barnes, Walter E. Kaufmann, Michela Fagiolini, and Charles A. Nelson (2015). "Visual evoked potentials detect cortical processing deficits in Rett syndrome". In: *Annals of Neurology* 78.5, pp. 775–786. ISSN: 1531-8249. DOI: 10.1002/ana.24513 (cit. on pp. 68, 82).

Lehman, Sharon S. (Sept. 2012). "Cortical visual impairment in children: identification, evaluation and diagnosis". In: *Current Opinion in Ophthalmology* 23.5, pp. 384–387. ISSN: 1040-8738. DOI: 10.1097/ICU.0b013e3283566b4b (cit. on p. 69).

Lehmann, Konrad and Siegrid Löwel (Sept. 1, 2008). "Age-Dependent Ocular Dominance Plasticity in Adult Mice". In: *PLOS ONE* 3.9. Publisher: Public Library of Science, e3120. ISSN: 1932-6203. DOI: 10.1371/journal.pone.0003120 (cit. on p. 8).

Lein, Ed S. et al. (Jan. 2007). "Genome-wide atlas of gene expression in the adult mouse brain". In: *Nature* 445.7124. Number: 7124 Publisher: Nature Publishing Group, pp. 168–176. ISSN: 1476-4687. DOI: 10.1038/nature05453 (cit. on pp. 32, 48, 54, 56, 62, 64).

Levelt, Christiaan N. and Mark Hübener (2012). "Critical-Period Plasticity in the Visual Cortex". In: *Annual Review of Neuroscience* 35.1, pp. 309–330. DOI: 10.1146/annurev-neuro-061010-113813 (cit. on p. 4).

Lorincz, Andrea and Zoltan Nusser (Dec. 31, 2008). "Cell-Type-Dependent Molecular Composition of the Axon Initial Segment". In: *Journal of Neuroscience* 28.53. Publisher: Society for Neuroscience Section: Articles, pp. 14329–14340. ISSN: 0270-6474, 1529-2401. DOI: 10.1523/JNEUROSCI.4833-08.2008 (cit. on p. 50).

Lozupone, Catherine and Rob Knight (Dec. 2005). "UniFrac: a New Phylogenetic Method for Comparing Microbial Communities". In: *Applied and Environmental Microbiology* 71.12, pp. 8228–8235. ISSN: 0099-2240, 1098-5336. DOI: 10.1128/AEM.71.12.8228-8235.2005 (cit. on p. 7).

Luczynski, Pauline, Monica Tramullas, Maria Viola, Fergus Shanahan, Gerard Clarke, Siobhain O'Mahony, Timothy G Dinan, and John F Cryan (June 20, 2017). "Microbiota regulates visceral pain in the mouse". In: *eLife* 6. Ed. by Peggy Mason. Publisher:

eLife Sciences Publications, Ltd, e25887. ISSN: 2050-084X. DOI: 10.7554/eLife.25887 (cit. on p. 22).

Luczynski, Pauline, Seán O. Whelan, Colette O'Sullivan, Gerard Clarke, Fergus Shanahan, Timothy G. Dinan, and John F. Cryan (2016). "Adult microbiota-deficient mice have distinct dendritic morphological changes: differential effects in the amygdala and hippocampus". In: *European Journal of Neuroscience* 44.9, pp. 2654–2666. ISSN: 1460-9568. DOI: 10.1111/ejn.13291 (cit. on p. 22).

Lupori, Leonardo, Sara Cornuti, Raffaele Mazziotti, Elisa Borghi, Emerenziana Ottaviano, Michele Dei Cas, Giulia Sagona, Tommaso Pizzorusso, and Paola Tognini (Jan. 2022). "The gut microbiota of environmentally enriched mice regulates visual cortical plasticity". In: *Cell Reports* 38.2, p. 110212. ISSN: 22111247. DOI: 10.1016/j.celrep.2021.110212 (cit. on p. 4).

Lupori, Leonardo, Giulia Sagona, Claudia Fuchs, Raffaele Mazziotti, Antonia Stefanov, Elena Putignano, Debora Napoli, Enrica Strettoi, Elisabetta Ciani, and Tommaso Pizzorusso (Sept. 1, 2019). "Site-specific abnormalities in the visual system of a mouse model of CDKL5 deficiency disorder". In: *Human Molecular Genetics* 28.17, pp. 2851–2861. ISSN: 0964-6906. DOI: 10.1093/hmg/ddz102 (cit. on p. 67).

Mataga, Nobuko, Yoko Mizuguchi, and Takao K. Hensch (Dec. 16, 2004). "Experience-Dependent Pruning of Dendritic Spines in Visual Cortex by Tissue Plasminogen Activator". In: *Neuron* 44.6, pp. 1031–1041. ISSN: 0896-6273. DOI: 10.1016/j.neuron.2004.11.028 (cit. on p. 22).

Mattapallil, Mary J., Eric F. Wawrousek, Chi-Chao Chan, Hui Zhao, Jayeeta Roychoudhury, Thomas A. Ferguson, and Rachel R. Caspi (May 17, 2012). "The Rd8 Mutation of the Crb1 Gene Is Present in Vendor Lines of C57BL/6N Mice and Embryonic Stem Cells, and Confounds Ocular Induced Mutant Phenotypes". In: *Investigative Ophthalmology & Visual Science* 53.6, pp. 2921–2927. ISSN: 1552-5783. DOI: 10.1167/iovs.12-9662 (cit. on p. 85).

Matthews, Russell T., Gail M. Kelly, Cynthia A. Zerillo, Grace Gray, Michael Tiemeyer, and Susan Hockfield (Sept. 1, 2002). "Aggrecan glycoforms contribute to the molecular heterogeneity of perineuronal nets". In: *The Journal of Neuroscience: The Official Journal of the Society for Neuroscience* 22.17, pp. 7536–7547. ISSN: 1529-2401 (cit. on p. 54).

Mazziotti, Raffaele, Leonardo Lupori, Giulia Sagona, Mariangela Gennaro, Grazia Della Sala, Elena Putignano, and Tommaso Pizzorusso (June 15, 2017). "Searching for biomarkers of CDKL5 disorder: early-onset visual impairment in CDKL5 mutant mice". In: *Human Molecular Genetics* 26.12, pp. 2290–2298. ISSN: 0964-6906, 1460-2083. DOI: 10.1093/hmg/ddx119 (cit. on pp. 26, 67, 79).

McKinney, Wes (2010). "Data Structures for Statistical Computing in Python". In: Python in Science Conference. Austin, Texas, pp. 56–61. DOI: 10.25080/Majora-92bf1922-00a (cit. on p. 61).

Melani, Federico, Davide Mei, Tiziana Pisano, Salvatore Savasta, Emilio Franzoni, Anna Rita Ferrari, Carla Marini, and Renzo Guerrini (2011). "CDKL5 gene-related epileptic encephalopathy: electroclinical findings in the first year of life". In: *Developmental Medicine & Child Neurology* 53.4, pp. 354–360. ISSN: 1469-8749. DOI: 10.1111/j.1469-8749.2010.03889.x (cit. on p. 68).

Mika, Agnieszka, Will Van Treuren, Antonio González, Jonathan J. Herrera, Rob Knight, and Monika Fleshner (May 27, 2015). "Exercise Is More Effective at Altering Gut

Microbial Composition and Producing Stable Changes in Lean Mass in Juvenile versus Adult Male F344 Rats". In: *PLOS ONE* 10.5. Publisher: Public Library of Science, e0125889. ISSN: 1932-6203. DOI: 10.1371/journal.pone.0125889 (cit. on p. 21).

Möhle, Luisa, Daniele Mattei, Markus M. Heimesaat, Stefan Bereswill, André Fischer, Marie Alutis, Timothy French, Dolores Hambardzumyan, Polly Matzinger, Ildiko R. Dunay, and Susanne A. Wolf (May 31, 2016). "Ly6Chi Monocytes Provide a Link between Antibiotic-Induced Changes in Gut Microbiota and Adult Hippocampal Neurogenesis". In: *Cell Reports* 15.9, pp. 1945–1956. ISSN: 2211-1247. DOI: 10.1016/j.celrep.2016.04.074 (cit. on p. 5).

Molinari, Florence, Annick Raas-Rothschild, Marlène Rio, Giuseppe Fiermonte, Ferechté Encha-Razavi, Luigi Palmieri, Ferdinando Palmieri, Ziva Ben-Neriah, Noman Kadhom, Michel Vekemans, Tania Attié-Bitach, Arnold Munnich, Pierre Rustin, and Laurence Colleaux (Feb. 1, 2005). "Impaired Mitochondrial Glutamate Transport in Autosomal Recessive Neonatal Myoclonic Epilepsy". In: *The American Journal of Human Genetics* 76.2, pp. 334–339. ISSN: 0002-9297. DOI: 10.1086/427564 (cit. on p. 82).

Monje, Michelle (July 8, 2018). "Myelin Plasticity and Nervous System Function". In: *Annual Review of Neuroscience* 41, pp. 61–76. ISSN: 1545-4126. DOI: 10.1146/annurev-neuro-080317-061853 (cit. on p. 56).

Moseley, Brian D., Radhika Dhamija, Elaine C. Wirrell, and Katherine C. Nickels (Feb. 1, 2012). "Historic, Clinical, and Prognostic Features of Epileptic Encephalopathies Caused by CDKL5 Mutations". In: *Pediatric Neurology* 46.2, pp. 101–105. ISSN: 0887-8994. DOI: 10.1016/j.pediatrneurol.2011.11.007 (cit. on pp. 68, 69, 82).

Murakami, Mari and Paola Tognini (2020). "The Circadian Clock as an Essential Molecular Link Between Host Physiology and Microorganisms". In: *Frontiers in Cellular and Infection Microbiology* 9. ISSN: 2235-2988 (cit. on p. 5).

Murakami, Mari, Paola Tognini, Yu Liu, Kristin L Eckel-Mahan, Pierre Baldi, and Paolo Sassone-Corsi (Sept. 2016). "Gut microbiota directs PPAR γ -driven reprogramming of the liver circadian clock by nutritional challenge". In: *EMBO reports* 17.9, pp. 1292–1303. ISSN: 1469-221X, 1469-3178. DOI: 10.15252/embr.201642463 (cit. on p. 26).

Murmu, Reena Prity, Wen Li, Anthony Holtmaat, and Jia-Yi Li (Aug. 7, 2013). "Dendritic Spine Instability Leads to Progressive Neocortical Spine Loss in a Mouse Model of Huntington's Disease". In: *Journal of Neuroscience* 33.32. Publisher: Society for Neuroscience Section: Articles, pp. 12997–13009. ISSN: 0270-6474, 1529-2401. DOI: 10.1523/JNEUROSCI.5284-12.2013 (cit. on p. 29).

Naba, Alexandra, Karl R. Clauser, Huiming Ding, Charles A. Whittaker, Steven A. Carr, and Richard O. Hynes (Jan. 1, 2016). "The extracellular matrix: Tools and insights for the "omics" era". In: *Matrix Biology* 49, pp. 10–24. ISSN: 0945-053X. DOI: 10.1016/j.matbio.2015.06.003 (cit. on pp. 50, 64).

Naka, K. I. and W. a. H. Rushton (1966). "S-potentials from colour units in the retina of fish (Cyprinidae)". In: *The Journal of Physiology* 185.3, pp. 536–555. ISSN: 1469-7793. DOI: 10.1113/jphysiol.1966.sp008001 (cit. on p. 87).

Napoli, Debora, Leonardo Lupori, Raffaele Mazziotti, Giulia Sagona, Sara Bagnoli, Muntaha Samad, Erika Kelmer Sacramento, Joanna Kirkpartick, Elena Putignano, Siwei Chen, Eva Terzibasi Tozzini, Paola Tognini, Pierre Baldi, Jessica CF Kwok, Alessandro Cellerino, and Tommaso Pizzorusso (Nov. 5, 2020). "MiR-29 coordinates

age-dependent plasticity brakes in the adult visual cortex". In: *EMBO reports* 21.11. ISSN: 1469-221X, 1469-3178. DOI: 10.15252/embr.202050431 (cit. on p. 32).

Nicholson, Jeremy K., Elaine Holmes, James Kinross, Remy Burcelin, Glenn Gibson, Wei Jia, and Sven Pettersson (June 8, 2012). "Host-Gut Microbiota Metabolic Interactions". In: *Science* 336.6086, pp. 1262–1267. ISSN: 0036-8075, 1095-9203. DOI: 10.1126/science.1223813 (cit. on p. 5).

Nithianantharajah, Jess and Anthony J. Hannan (Sept. 2006). "Enriched environments, experience-dependent plasticity and disorders of the nervous system". In: *Nature Reviews Neuroscience* 7.9. Number: 9 Publisher: Nature Publishing Group, pp. 697–709. ISSN: 1471-0048. DOI: 10.1038/nrn1970 (cit. on p. 4).

Nithianantharajah, Jess, Hannah Levis, and Mark Murphy (May 1, 2004). "Environmental enrichment results in cortical and subcortical changes in levels of synaptophysin and PSD-95 proteins". In: *Neurobiology of Learning and Memory* 81.3, pp. 200–210. ISSN: 1074-7427. DOI: 10.1016/j.nlm.2004.02.002 (cit. on p. 20).

Ogiwara, Ikuo, Hiroyuki Miyamoto, Noriyuki Morita, Nafiseh Atapour, Emi Mazaki, Ikuyo Inoue, Tamaki Takeuchi, Shigeyoshi Itohara, Yuchio Yanagawa, Kunihiko Obata, Teiichi Furuichi, Takao K. Hensch, and Kazuhiro Yamakawa (May 30, 2007). "Nav1.1 Localizes to Axons of Parvalbumin-Positive Inhibitory Interneurons: A Circuit Basis for Epileptic Seizures in Mice Carrying an Scn1a Gene Mutation". In: *The Journal of Neuroscience* 27.22, pp. 5903–5914. ISSN: 0270-6474. DOI: 10.1523/JNEUROSCI.5270-06.2007 (cit. on p. 50).

Oh, Seung Wook et al. (Apr. 2014). "A mesoscale connectome of the mouse brain". In: *Nature* 508.7495. Number: 7495 Publisher: Nature Publishing Group, pp. 207–214. ISSN: 1476-4687. DOI: 10.1038/nature13186 (cit. on pp. 32, 47, 54).

Olson, Christine A., Helen E. Vuong, Jessica M. Yano, Qingxing Y. Liang, David J. Nusbaum, and Elaine Y. Hsiao (June 14, 2018). "The Gut Microbiota Mediates the Anti-Seizure Effects of the Ketogenic Diet". In: *Cell* 173.7, 1728–1741.e13. ISSN: 0092-8674. DOI: 10.1016/j.cell.2018.04.027 (cit. on p. 21).

Oohashi, Toshitaka, Midori Edamatsu, Yoko Bekku, and Daniela Carulli (Dec. 1, 2015). "The hyaluronan and proteoglycan link proteins: Organizers of the brain extracellular matrix and key molecules for neuronal function and plasticity". In: *Experimental Neurology*. Deciphering sugar chain-based signals regulating integrative neuronal functions 274, pp. 134–144. ISSN: 0014-4886. DOI: 10.1016/j.expneurol.2015.09.010 (cit. on p. 48).

Oray, Serkan, Ania Majewska, and Mriganka Sur (Dec. 16, 2004). "Dendritic Spine Dynamics Are Regulated by Monocular Deprivation and Extracellular Matrix Degradation". In: *Neuron* 44.6, pp. 1021–1030. ISSN: 0896-6273. DOI: 10.1016/j.neuron.2004.12.001 (cit. on p. 22).

Orrù, Graziella, William Pettersson-Yeo, Andre F. Marquand, Giuseppe Sartori, and Andrea Mechelli (Apr. 1, 2012). "Using Support Vector Machine to identify imaging biomarkers of neurological and psychiatric disease: A critical review". In: *Neuroscience & Biobehavioral Reviews* 36.4, pp. 1140–1152. ISSN: 0149-7634. DOI: 10.1016/j.neubiorev.2012.01.004 (cit. on p. 87).

Paine, S. M. L., P. Munot, J. Carmichael, K. Das, M. A. Weber, P. Prabhakar, and T. S. Jacques (2012). "The neuropathological consequences of CDKL5 mutation". In: *Neuropathology and Applied Neurobiology* 38.7, pp. 744–747. ISSN: 1365-2990. DOI: 10.1111/j.1365-2990.2012.01292.x (cit. on pp. 68, 82).

Pantazopoulos, Harry, Tsung-Ung W. Woo, Maribel P. Lim, Nicholas Lange, and Sabina Berretta (Feb. 2010). "Extracellular matrix-glial abnormalities in the amygdala and entorhinal cortex of subjects diagnosed with schizophrenia". In: *Archives of General Psychiatry* 67.2, pp. 155–166. ISSN: 1538-3636. DOI: 10.1001/archgenpsychiatry.2009.196 (cit. on p. 31).

Paolicelli, Rosa C., Giulia Bolasco, Francesca Pagani, Laura Maggi, Maria Scianni, Patrizia Panzanelli, Maurizio Giustetto, Tiago Alves Ferreira, Eva Guiducci, Laura Dumas, Davide Ragozzino, and Cornelius T. Gross (Sept. 9, 2011). "Synaptic Pruning by Microglia Is Necessary for Normal Brain Development". In: *Science* 333.6048. Publisher: American Association for the Advancement of Science, pp. 1456–1458. DOI: 10.1126/science.1202529 (cit. on p. 22).

Patnala, Radhika, Thiruma V. Arumugam, Neelima Gupta, and S. Thameem Dheen (Oct. 1, 2017). "HDAC Inhibitor Sodium Butyrate-Mediated Epigenetic Regulation Enhances Neuroprotective Function of Microglia During Ischemic Stroke". In: *Molecular Neurobiology* 54.8, pp. 6391–6411. ISSN: 1559-1182. DOI: 10.1007/s12035-016-0149-z (cit. on p. 22).

Paxinos, George, Glenda Halliday, Charles Watson, and Mustafa S. Kassem (Mar. 21, 2020). *Atlas of the Developing Mouse Brain*. Google-Books-ID: KDLXDwAAQBAJ. Academic Press. 386 pp. ISBN: 978-0-12-822646-9 (cit. on p. 88).

Pedregosa, Fabian, Gaël Varoquaux, Alexandre Gramfort, Vincent Michel, Bertrand Thirion, Olivier Grisel, Mathieu Blondel, Peter Prettenhofer, Ron Weiss, Vincent Dubourg, Jake Vanderplas, Alexandre Passos, David Cournapeau, Matthieu Brucher, Matthieu Perrot, and Édouard Duchesnay (2011). "Scikit-learn: Machine Learning in Python". In: *Journal of Machine Learning Research* 12.85, pp. 2825–2830. ISSN: 1533-7928 (cit. on p. 61).

Pereira, Francisco, Tom Mitchell, and Matthew Botvinick (Mar. 1, 2009). "Machine learning classifiers and fMRI: A tutorial overview". In: *NeuroImage*. Mathematics in Brain Imaging 45.1, S199–S209. ISSN: 1053-8119. DOI: 10.1016/j.neuroimage.2008.11.007 (cit. on p. 87).

Pham, Therese M., Bengt Winblad, Ann-Charlotte Granholm, and Abdul H. Mohammed (Aug. 1, 2002). "Environmental influences on brain neurotrophins in rats". In: *Pharmacology Biochemistry and Behavior* 73.1, pp. 167–175. ISSN: 0091-3057. DOI: 10.1016/S0091-3057(02)00783-9 (cit. on p. 20).

Pirbhoy, Patricia S., Maham Rais, Jonathan W. Lovelace, Walker Woodard, Khaleel A. Razak, Devin K. Binder, and Iryna M. Ethell (2020). "Acute pharmacological inhibition of matrix metalloproteinase-9 activity during development restores perineuronal net formation and normalizes auditory processing in Fmr1 KO mice". In: *Journal of Neurochemistry* 155.5. _eprint: https://onlinelibrary.wiley.com/doi/pdf/10.1111/jnc.15037, pp. 538–558. ISSN: 1471-4159. DOI: 10.1111/jnc.15037 (cit. on p. 48).

Pizzo, Riccardo, Antonia Gurgone, Enrico Castroflorio, Elena Amendola, Cornelius Gross, Marco Sassoè-Pognetto, and Maurizio Giustetto (2016). "Lack of Cdkl5 Disrupts the Organization of Excitatory and Inhibitory Synapses and Parvalbumin Interneurons in the Primary Visual Cortex". In: *Frontiers in Cellular Neuroscience* 10. ISSN: 1662-5102 (cit. on p. 83).

Pizzorusso, Tommaso, Nicoletta Berardi, and Lamberto Maffei (May 24, 2007). "A Richness that Cures". In: *Neuron* 54.4, pp. 508–510. ISSN: 0896-6273. DOI: 10.1016/j.neuron.2007.05.003 (cit. on p. 5).

Pizzorusso, Tommaso, Paolo Medini, Nicoletta Berardi, Sabrina Chierzi, James W. Fawcett, and Lamberto Maffei (Nov. 8, 2002). "Reactivation of Ocular Dominance Plasticity in the Adult Visual Cortex". In: *Science* 298.5596, pp. 1248–1251. ISSN: 0036-8075, 1095-9203. DOI: 10.1126/science.1072699 (cit. on p. 31).

Praag, Henriette van, Gerd Kempermann, and Fred H. Gage (Dec. 2000). "Neural consequences of enviromental enrichment". In: *Nature Reviews Neuroscience* 1.3. Number: 3 Publisher: Nature Publishing Group, pp. 191–198. ISSN: 1471-0048. DOI: 10.1038/35044558 (cit. on p. 21).

Puchades, Maja A., Gergely Csucs, Debora Ledergerber, Trygve B. Leergaard, and Jan G. Bjaalie (May 29, 2019). "Spatial registration of serial microscopic brain images to three-dimensional reference atlases with the QuickNII tool". In: *PLOS ONE* 14.5. Publisher: Public Library of Science, e0216796. ISSN: 1932-6203. DOI: 10.1371/journal.pone.0216796 (cit. on p. 60).

Rampon, Claire, Cecilia H. Jiang, Helin Dong, Ya-Ping Tang, David J. Lockhart, Peter G. Schultz, Joe Z. Tsien, and Yinghe Hu (Nov. 7, 2000). "Effects of environmental enrichment on gene expression in the brain". In: *Proceedings of the National Academy of Sciences* 97.23. Publisher: Proceedings of the National Academy of Sciences, pp. 12880–12884. DOI: 10.1073/pnas.97.23.12880 (cit. on p. 20).

Reichelt, Amy C., Dominic J. Hare, Timothy J. Bussey, and Lisa M. Saksida (July 2019). "Perineuronal Nets: Plasticity, Protection, and Therapeutic Potential". In: *Trends in Neurosciences* 42.7, pp. 458–470. ISSN: 1878-108X. DOI: 10.1016/j.tins.2019.04.003 (cit. on pp. 31, 55).

Reichelt, Amy C., Claire A. Lemieux, Oren Princz-Lebel, Ashmita Singh, Timothy J. Bussey, and Lisa M. Saksida (Mar. 10, 2021). "Age-dependent and region-specific alteration of parvalbumin neurons, perineuronal nets and microglia in the mouse prefrontal cortex and hippocampus following obesogenic diet consumption". In: *Scientific Reports* 11.1, p. 5593. ISSN: 2045-2322. DOI: 10.1038/s41598-021-85092-x (cit. on p. 32).

Ren, Shaoqing, Kaiming He, Ross Girshick, and Jian Sun (2015). "Faster R-CNN: Towards Real-Time Object Detection with Region Proposal Networks". In: *Advances in Neural Information Processing Systems*. Vol. 28. Curran Associates, Inc. (cit. on p. 60).

Ricciardi, Sara, Federica Ungaro, Melanie Hambrock, Nils Rademacher, Gilda Stefanelli, Dario Brambilla, Alessandro Sessa, Cinzia Magagnotti, Angela Bachi, Elisa Giarda, Chiara Verpelli, Charlotte Kilstrup-Nielsen, Carlo Sala, Vera M. Kalscheuer, and Vania Broccoli (Sept. 2012). "CDKL5 ensures excitatory synapse stability by reinforcing NGL-1–PSD95 interaction in the postsynaptic compartment and is impaired in patient iPSC-derived neurons". In: *Nature Cell Biology* 14.9. Number: 9 Publisher: Nature Publishing Group, pp. 911–923. ISSN: 1476-4679. DOI: 10.1038/ncb2566 (cit. on pp. 68, 83).

Romberg, C., S. Yang, R. Melani, M. R. Andrews, A. E. Horner, M. G. Spillantini, T. J. Bussey, J. W. Fawcett, T. Pizzorusso, and L. M. Saksida (Apr. 17, 2013). "Depletion of Perineuronal Nets Enhances Recognition Memory and Long-Term Depression in the Perirhinal Cortex". In: *Journal of Neuroscience* 33.16, pp. 7057–7065. ISSN: 0270-6474, 1529-2401. DOI: 10.1523/JNEUROSCI.6267-11.2013 (cit. on p. 31).

Rooks, Michelle G. and Wendy S. Garrett (June 2016). "Gut microbiota, metabolites and host immunity". In: *Nature Reviews Immunology* 16.6. Number: 6 Publisher: Nature

Publishing Group, pp. 341–352. ISSN: 1474-1741. DOI: 10.1038/nri.2016.42 (cit. on p. 5).

Rosenzweig, Mark R. and Edward L. Bennett (June 1, 1996). "Psychobiology of plasticity: effects of training and experience on brain and behavior". In: *Behavioural Brain Research*. Synaptic Plasticity of the Cortex 78.1, pp. 57–65. ISSN: 0166-4328. DOI: 10.1016/0166-4328(95)00216-2 (cit. on pp. 4, 20).

Rossier, J., A. Bernard, J.-H. Cabungcal, Q. Perrenoud, A. Savoye, T. Gallopin, M. Hawrylycz, M. Cuénod, K. Do, A. Urban, and Ed S. Lein (Feb. 2015). "Cortical fast-spiking parvalbumin interneurons enwrapped in the perineuronal net express the metallopeptidases Adamts8, Adamts15 and Neprilysin". In: *Molecular Psychiatry* 20.2. Number: 2 Publisher: Nature Publishing Group, pp. 154–161. ISSN: 1476-5578. DOI: 10.1038/mp.2014.162 (cit. on p. 48).

Rusconi, Laura, Lisa Salvatoni, Laura Giudici, Ilaria Bertani, Charlotte Kilstrup-Nielsen, Vania Broccoli, and Nicoletta Landsberger (Oct. 31, 2008). "CDKL5 Expression Is Modulated during Neuronal Development and Its Subcellular Distribution Is Tightly Regulated by the C-terminal Tail *". In: *Journal of Biological Chemistry* 283.44. Publisher: Elsevier, pp. 30101–30111. ISSN: 0021-9258, 1083-351X. DOI: 10.1074/jbc.M804613200 (cit. on pp. 68, 82).

Sajo, Mari, Graham Ellis-Davies, and Hirofumi Morishita (Sept. 7, 2016). "Lynx1 Limits Dendritic Spine Turnover in the Adult Visual Cortex". In: *Journal of Neuroscience* 36.36. Publisher: Society for Neuroscience Section: Articles, pp. 9472–9478. ISSN: 0270-6474, 1529-2401. DOI: 10.1523/JNEUROSCI.0580-16.2016 (cit. on p. 22).

Sale, Alessandro, José Fernando Maya Vetencourt, Paolo Medini, Maria Cristina Cenni, Laura Baroncelli, Roberto De Pasquale, and Lamberto Maffei (June 2007). "Environmental enrichment in adulthood promotes amblyopia recovery through a reduction of intracortical inhibition". In: *Nature Neuroscience* 10.6. Number: 6 Publisher: Nature Publishing Group, pp. 679–681. ISSN: 1546-1726. DOI: 10.1038/nn1899 (cit. on pp. 4, 9, 20).

Sarnaik, Rashmi, Hui Chen, Xiaorong Liu, and Jianhua Cang (June 2014). "Genetic disruption of the On visual pathway affects cortical orientation selectivity and contrast sensitivity in mice". In: *Journal of Neurophysiology* 111.11. Publisher: American Physiological Society, pp. 2276–2286. ISSN: 0022-3077. DOI: 10.1152/jn.00558.2013 (cit. on p. 87).

Sawilowsky, Shlomo (Nov. 1, 2009). "New Effect Size Rules of Thumb". In: *Journal of Modern Applied Statistical Methods* 8.2. ISSN: 1538 - 9472. DOI: 10.22237/jmasm/1257035100 (cit. on p. 79).

Schafer, Dorothy P., Emily K. Lehrman, Amanda G. Kautzman, Ryuta Koyama, Alan R. Mardinly, Ryo Yamasaki, Richard M. Ransohoff, Michael E. Greenberg, Ben A. Barres, and Beth Stevens (May 24, 2012). "Microglia Sculpt Postnatal Neural Circuits in an Activity and Complement-Dependent Manner". In: *Neuron* 74.4, pp. 691–705. ISSN: 0896-6273. DOI: 10.1016/j.neuron.2012.03.026 (cit. on p. 22).

Schecter, Rachel W., Erin E. Maher, Christina A. Welsh, Beth Stevens, Alev Erisir, and Mark F. Bear (Nov. 1, 2017). "Experience-Dependent Synaptic Plasticity in V1 Occurs without Microglial CX3CR1". In: *Journal of Neuroscience* 37.44. Publisher: Society for Neuroscience Section: Research Articles, pp. 10541–10553. ISSN: 0270-6474, 1529-2401. DOI: 10.1523/JNEUROSCI.2679-16.2017 (cit. on p. 22).

Schroeder, Bjoern O. and Fredrik Bäckhed (Oct. 2016). "Signals from the gut microbiota to distant organs in physiology and disease". In: *Nature Medicine* 22.10. Number: 10 Publisher: Nature Publishing Group, pp. 1079–1089. ISSN: 1546-170X. DOI: 10.1038/nm.4185 (cit. on p. 5).

Schroeder, Ethan, Li Yuan, Eunju Seong, Cheryl Ligon, Nicholas DeKorver, C.B. Gurumurthy, and Jyothi Arikkath (June 1, 2019). "Neuron-Type Specific Loss of CDKL5 Leads to Alterations in mTOR Signaling and Synaptic Markers". In: *Molecular Neurobiology* 56.6, pp. 4151–4162. ISSN: 1559-1182. DOI: 10.1007/s12035-018-1346-8 (cit. on p. 83).

Seeger, G., K. Brauer, W. Härtig, and G. Brückner (Jan. 1994). "Mapping of perineuronal nets in the rat brain stained by colloidal iron hydroxide histochemistry and lectin cytochemistry". In: *Neuroscience* 58.2, pp. 371–388. ISSN: 0306-4522. DOI: 10.1016/0306-4522(94)90044-2 (cit. on p. 31).

Segata, Nicola, Jacques Izard, Levi Waldron, Dirk Gevers, Larisa Miropolsky, Wendy S Garrett, and Curtis Huttenhower (2011). "Metagenomic biomarker discovery and explanation". In: *Genome Biology* 12.6, R60. ISSN: 1465-6906. DOI: 10.1186/gb-2011-12-6-r60 (cit. on pp. 7, 26).

Silingardi, Davide, Manuela Scali, Giulio Belluomini, and Tommaso Pizzorusso (2010). "Epigenetic treatments of adult rats promote recovery from visual acuity deficits induced by long-term monocular deprivation". In: *European Journal of Neuroscience* 31.12, pp. 2185–2192. ISSN: 1460-9568. DOI: 10.1111/j.1460-9568.2010.07261.x (cit. on p. 22).

Slaker, Megan, Jesse Barnes, Barbara A. Sorg, and Jeffrey W. Grimm (Dec. 15, 2016). "Impact of Environmental Enrichment on Perineuronal Nets in the Prefrontal Cortex following Early and Late Abstinence from Sucrose Self-Administration in Rats". In: *PLOS ONE* 11.12. Publisher: Public Library of Science, e0168256. ISSN: 1932-6203. DOI: 10.1371/journal.pone.0168256 (cit. on p. 20).

Song, Suk-Young, Minji Chae, Ji Hea Yu, Min Young Lee, Soonil Pyo, Yoon-Kyum Shin, Ahreum Baek, Jung-Won Park, Eun Sook Park, Ja Young Choi, and Sung-Rae Cho (2018). "Environmental Enrichment Upregulates Striatal Synaptic Vesicle-Associated Proteins and Improves Motor Function". In: *Frontiers in Neurology* 9. ISSN: 1664-2295 (cit. on p. 20).

Stalpers, Xenia L., Liesbeth Spruijt, Helger G. Yntema, and Aad Verrips (Jan. 1, 2012). "Clinical Phenotype of 5 Females With a CDKL5 Mutation". In: *Journal of Child Neurology* 27.1. Publisher: SAGE Publications Inc, pp. 90–93. ISSN: 0883-0738. DOI: 10.1177/0883073811413832 (cit. on pp. 68, 69, 82).

Stanislaw, Harold and Natasha Todorov (Mar. 1, 1999). "Calculation of signal detection theory measures". In: *Behavior Research Methods, Instruments, & Computers* 31.1, pp. 137–149. ISSN: 1532-5970. DOI: 10.3758/BF03207704 (cit. on p. 88).

Sun, Yujiao Jennifer, J. Sebastian Espinosa, Mahmood S. Hoseini, and Michael P. Stryker (Oct. 22, 2019). "Experience-dependent structural plasticity at pre- and postsynaptic sites of layer 2/3 cells in developing visual cortex". In: *Proceedings of the National Academy of Sciences* 116.43. Publisher: Proceedings of the National Academy of Sciences, pp. 21812–21820. DOI: 10.1073/pnas.1914661116 (cit. on p. 22).

Tang, Sheng, I.-Ting Judy Wang, Cuiyong Yue, Hajime Takano, Barbara Terzic, Katarina Pance, Jun Y. Lee, Yue Cui, Douglas A. Coulter, and Zhaolan Zhou (Aug. 2, 2017). "Loss of CDKL5 in Glutamatergic Neurons Disrupts Hippocampal Microcircuitry and

Leads to Memory Impairment in Mice". In: *Journal of Neuroscience* 37.31. Publisher: Society for Neuroscience Section: Research Articles, pp. 7420–7437. ISSN: 0270-6474, 1529-2401. DOI: 10.1523/JNEUROSCI.0539-17.2017 (cit. on p. 83).

Thukral, Ashwani K (2017). "A review on measurement of Alpha diversity in biology". In: *Agricultural Research Journal* 54.1, p. 1. ISSN: 2395-1435, 2395-146X. DOI: 10.5958/2395-146X.2017.00001.1 (cit. on p. 7).

Tognini, Paola (2017). "Gut Microbiota: A Potential Regulator of Neurodevelopment". In: *Frontiers in Cellular Neuroscience* 11. ISSN: 1662-5102 (cit. on p. 5).

Tognini, Paola, Ilaria Manno, Joyce Bonaccorsi, Maria Cristina Cenni, Alessandro Sale, and Lamberto Maffei (Apr. 11, 2012). "Environmental Enrichment Promotes Plasticity and Visual Acuity Recovery in Adult Monocular Amblyopic Rats". In: *PLOS ONE* 7.4. Publisher: Public Library of Science, e34815. ISSN: 1932-6203. DOI: 10.1371/journal.pone.0034815 (cit. on p. 4).

Trazzi, Stefania, Marianna De Franceschi, Claudia Fuchs, Stefano Bastianini, Rocchina Viggiano, Leonardo Lupori, Raffaele Mazziotti, Giorgio Medici, Viviana Lo Martire, Elisa Ren, Roberto Rimondini, Giovanna Zoccoli, Renata Bartesaghi, Tommaso Pizzorusso, and Elisabetta Ciani (May 1, 2018). "CDKL5 protein substitution therapy rescues neurological phenotypes of a mouse model of CDKL5 disorder". In: *Human Molecular Genetics* 27.9, pp. 1572–1592. ISSN: 0964-6906. DOI: 10.1093/hmg/ddy064 (cit. on pp. 67, 80).

Trazzi, Stefania, Claudia Fuchs, Rocchina Viggiano, Marianna De Franceschi, Emanuele Valli, Paulina Jedynak, Finn K. Hansen, Giovanni Perini, Roberto Rimondini, Thomas Kurz, Renata Bartesaghi, and Elisabetta Ciani (Sept. 15, 2016). "HDAC4: a key factor underlying brain developmental alterations in CDKL5 disorder". In: *Human Molecular Genetics* 25.18, pp. 3887–3907. ISSN: 0964-6906. DOI: 10.1093/hmg/ddw231 (cit. on pp. 82, 83).

Tremaroli, Valentina and Fredrik Bäckhed (Sept. 2012). "Functional interactions between the gut microbiota and host metabolism". In: *Nature* 489.7415. Number: 7415 Publisher: Nature Publishing Group, pp. 242–249. ISSN: 1476-4687. DOI: 10.1038/nature11552 (cit. on p. 5).

Tremblay, Robin, Soohyun Lee, and Bernardo Rudy (July 20, 2016). "GABAergic interneurons in the neocortex: From cellular properties to circuits". In: *Neuron* 91.2, pp. 260–292. ISSN: 0896-6273. DOI: 10.1016/j.neuron.2016.06.033 (cit. on p. 54).

Ueno, Hiroshi, Kazuki Fujii, Shunsuke Suemitsu, Shinji Murakami, Naoya Kitamura, Kenta Wani, Shozo Aoki, Motoi Okamoto, Takeshi Ishihara, and Keizo Takao (June 1, 2018). "Expression of aggrecan components in perineuronal nets in the mouse cerebral cortex". In: *IBRO Reports* 4, pp. 22–37. ISSN: 2451-8301. DOI: 10.1016/j.ibror.2018.01.002 (cit. on pp. 31, 32, 54).

Van Groen, Thomas and J. Michael Wyss (2003). "Connections of the retrosplenial granular b cortex in the rat". In: *Journal of Comparative Neurology* 463.3. _eprint: https://onlinelibrary.wiley.com/doi/pdf/10.1002/cne.10757, pp. 249–263. ISSN: 1096-9861. DOI: 10.1002/cne.10757 (cit. on p. 56).

Vann, Seralynne D., John P. Aggleton, and Eleanor A. Maguire (Nov. 2009). "What does the retrosplenial cortex do?" In: *Nature Reviews Neuroscience* 10.11, pp. 792–802. ISSN: 1471-003X, 1471-0048. DOI: 10.1038/nrn2733 (cit. on p. 56).

Vidal, George S., Maja Djurisic, Kiana Brown, Richard W. Sapp, and Carla J. Shatz (Oct. 7, 2016). "Cell-Autonomous Regulation of Dendritic Spine Density by PirB". In: *eNeuro*

3.5, ENEURO.0089–16.2016. ISSN: 2373-2822. DOI: 10.1523/ENEURO.0089-16.2016 (cit. on p. 22).

Villa, Katherine L., Kalen P. Berry, Jaichandar Subramanian, Jae Won Cha, Won Chan Oh, Hyung-Bae Kwon, Yoshiyuki Kubota, Peter T. C. So, and Elly Nedivi (Feb. 17, 2016). "Inhibitory Synapses Are Repeatedly Assembled and Removed at Persistent Sites In Vivo". In: *Neuron* 89.4, pp. 756–769. ISSN: 0896-6273. DOI: 10.1016/j.neuron.2016.01.010 (cit. on p. 22).

Virtanen, Pauli et al. (Mar. 2020). "SciPy 1.0: fundamental algorithms for scientific computing in Python". In: *Nature Methods* 17.3. Number: 3 Publisher: Nature Publishing Group, pp. 261–272. ISSN: 1548-7105. DOI: 10.1038/s41592-019-0686-2 (cit. on p. 61).

Vries, Saskia E. J. de et al. (Jan. 2020). "A large-scale standardized physiological survey reveals functional organization of the mouse visual cortex". In: *Nature Neuroscience* 23.1. Number: 1 Publisher: Nature Publishing Group, pp. 138–151. ISSN: 1546-1726. DOI: 10.1038/s41593-019-0550-9 (cit. on p. 32).

Wang, Bor-Shuen, Liang Feng, Mingna Liu, Xiaorong Liu, and Jianhua Cang (Oct. 2, 2013). "Environmental Enrichment Rescues Binocular Matching of Orientation Preference in Mice that Have a Precocious Critical Period". In: *Neuron* 80.1, pp. 198–209. ISSN: 0896-6273. DOI: 10.1016/j.neuron.2013.07.023 (cit. on p. 20).

Wang, I-Ting Judy, Megan Allen, Darren Goffin, Xinjian Zhu, Andrew H. Fairless, Edward S. Brodkin, Steve J. Siegel, Eric D. Marsh, Julie A. Blendy, and Zhaolan Zhou (Dec. 26, 2012). "Loss of CDKL5 disrupts kinome profile and event-related potentials leading to autistic-like phenotypes in mice". In: *Proceedings of the National Academy of Sciences* 109.52. Publisher: Proceedings of the National Academy of Sciences, pp. 21516–21521. DOI: 10.1073/pnas.1216988110 (cit. on pp. 68, 82).

Wang, Quanxin et al. (May 14, 2020). "The Allen Mouse Brain Common Coordinate Framework: A 3D Reference Atlas". In: *Cell* 181.4, 936–953.e20. ISSN: 0092-8674. DOI: 10.1016/j.cell.2020.04.007 (cit. on pp. 32, 59).

Waskom, Michael L. (Apr. 6, 2021). "seaborn: statistical data visualization". In: *Journal of Open Source Software* 6.60, p. 3021. ISSN: 2475-9066. DOI: 10.21105/joss.03021 (cit. on p. 65).

Williamson, Sarah L., Laura Giudici, Charlotte Kilstrup-Nielsen, Wendy Gold, Gregory J. Pelka, Patrick P. L. Tam, Andrew Grimm, Dionigio Prodi, Nicoletta Landsberger, and John Christodoulou (Feb. 1, 2012). "A novel transcript of cyclin-dependent kinase-like 5 (CDKL5) has an alternative C-terminus and is the predominant transcript in brain". In: *Human Genetics* 131.2, pp. 187–200. ISSN: 1432-1203. DOI: 10.1007/s00439-011-1058-x (cit. on p. 89).

Wong, Tzu-Tsung (Sept. 1, 2015). "Performance evaluation of classification algorithms by k-fold and leave-one-out cross validation". In: *Pattern Recognition* 48.9, pp. 2839–2846. ISSN: 0031-3203. DOI: 10.1016/j.patcog.2015.03.009 (cit. on p. 63).

Xu, Huixin, Eilrayna Gelyana, Molly Rajsombath, Ting Yang, Shaomin Li, and Dennis Selkoe (Aug. 31, 2016). "Environmental Enrichment Potently Prevents Microglia-Mediated Neuroinflammation by Human Amyloid β-Protein Oligomers". In: *Journal of Neuroscience* 36.35. Publisher: Society for Neuroscience Section: Articles, pp. 9041–9056. ISSN: 0270-6474, 1529-2401. DOI: 10.1523/JNEUROSCI.1023-16.2016 (cit. on pp. 14, 22).

Yamawaki, Yosuke, Norika Yoshioka, Kanako Nozaki, Hikaru Ito, Keisuke Oda, Kana Harada, Satomi Shirawachi, Satoshi Asano, Hidenori Aizawa, Shigeto Yamawaki, Takashi Kanematsu, and Hiroyuki Akagi (Feb. 1, 2018). "Sodium butyrate abolishes lipopolysaccharide-induced depression-like behaviors and hippocampal microglial activation in mice". In: *Brain Research* 1680, pp. 13–38. ISSN: 0006-8993. DOI: 10.1016/j.brainres.2017.12.004 (cit. on p. 22).

Ye, Qian and Qing-long Miao (Aug. 8, 2013). "Experience-dependent development of perineuronal nets and chondroitin sulfate proteoglycan receptors in mouse visual cortex". In: *Matrix Biology* 32.6, pp. 352–363. ISSN: 0945-053X. DOI: 10.1016/j.matbio.2013.04.001 (cit. on p. 31).

Zhang, Bing, Stefan Kirov, and Jay Snoddy (July 1, 2005). "WebGestalt: an integrated system for exploring gene sets in various biological contexts". In: *Nucleic Acids Research* 33 (suppl_2), W741–W748. ISSN: 0305-1048. DOI: 10.1093/nar/gki475 (cit. on p. 64).

Zhang, Yonghong, Lucas Matt, Tommaso Patriarchi, Zulfiqar A Malik, Dhrubajyoti Chowdhury, Deborah K Park, Alessandra Renieri, and James B Ames (June 17, 2014). "Capping of the N-terminus of PSD-95 by calmodulin triggers its postsynaptic release". In: *The EMBO Journal* 33.12. Publisher: John Wiley & Sons, Ltd, pp. 1341–1353. ISSN: 0261-4189. DOI: 10.1002/embj.201488126 (cit. on p. 68).

Zhao, Shitao, Jianqiang Sun, Kentaro Shimizu, and Koji Kadota (Mar. 1, 2018). "Silhouette Scores for Arbitrary Defined Groups in Gene Expression Data and Insights into Differential Expression Results". In: *Biological Procedures Online* 20.1, p. 5. ISSN: 1480-9222. DOI: 10.1186/s12575-018-0067-8 (cit. on p. 48).

Zhu, Yong-Chuan, Dan Li, Lu Wang, Bin Lu, Jing Zheng, Shi-Lin Zhao, Rong Zeng, and Zhi-Qi Xiong (May 28, 2013). "Palmitoylation-dependent CDKL5–PSD-95 interaction regulates synaptic targeting of CDKL5 and dendritic spine development". In: *Proceedings of the National Academy of Sciences* 110.22. Publisher: Proceedings of the National Academy of Sciences, pp. 9118–9123. DOI: 10.1073/pnas.1300003110 (cit. on pp. 68, 83).

Zingg, Brian, Houri Hintiryan, Lin Gou, Monica Y. Song, Maxwell Bay, Michael S. Bienkowski, Nicholas N. Foster, Seita Yamashita, Ian Bowman, Arthur W. Toga, and Hong-Wei Dong (Feb. 27, 2014). "Neural Networks of the Mouse Neocortex". In: *Cell* 156.5, pp. 1096–1111. ISSN: 0092-8674. DOI: 10.1016/j.cell.2014.02.023 (cit. on pp. 48, 54).

Appendices

Supplmental information for Part II

1 Supplementary table ST1 - Coarse-ontology brain regions

Name	Acronym	regionID
Isocortex	Isocortex	315
Olfactory areas	OLF	698
Hippocampal formation	HPF	1089
Cortical subplate	CTXsp	703
Striatum	STR	477
Pallidum	PAL	803
Thalamus	TH	549
Hypothalamus	HY	1097
Midbrain	MB	313
Pons	P	771
Medulla	MY	354
Cerebellum	CB	512

2 Supplementary table ST2 - Cortical regions

Name	Acronym	RegionID
Frontal pole cerebral cortex	FRP	184
Primary motor area	MOp	985
Secondary motor area	MOs	993
Primary somatosensory area - nose	SSp-n	353
Primary somatosensory area - barrel field	SSp-bfd	329
Primary somatosensory area - lower limb	SSp-ll	337
Primary somatosensory area - mouth	SSp-m	345
Primary somatosensory area - upper limb	SSp-ul	369
Primary somatosensory area - trunk	SSp-tr	361
Primary somatosensory area - unassigned	SSp-un	182305689
Supplemental somatosensory area	SSs	378
Gustatory areas	GU	1057
Visceral area	VISC	677
Dorsal auditory area	AUDd	1011
Primary auditory area	AUDp	1002
Posterior auditory area	AUDpo	1027
Ventral auditory area	AUDv	1018
Anterolateral visual area	VISal	402
Anteromedial visual area	VISam	394
Lateral visual area	VISl	409
Primary visual area	VISp	385

Name	Acronym	RegionID
Posterolateral visual area	VISpl	425
posteromedial visual area	VISpm	533
Laterointermediate area	VISli	312782574
Postrhinal area	VISpor	312782628
Anterior cingulate area - dorsal part	ACAd	39
Anterior cingulate area - ventral part	ACAv	48
Prelimbic area	PL	972
Infralimbic area	ILA	44
Orbital area - lateral part	ORBl	723
Orbital area - medial part	ORBm	731
Orbital area - ventrolateral part	ORBvl	746
Agranular insular area - dorsal part	AId	104
Agranular insular area - posterior part	AIp	111
Agranular insular area - ventral part	AIv	119
Retrosplenial area - lateral agranular part	RSPagl	894
Retrosplenial area - dorsal part	RSPd	879
Retrosplenial area - ventral part	RSPv	886
Anterior area	VISa	312782546
Rostrolateral visual area	VISrl	417
Temporal association areas	TEa	541
Perirhinal area	PERI	922
Ectorhinal area	ECT	895

3 Supplementary table ST3 - Mid-ontology brain regions

Name	Acronym	Parent Area	regionID
Primary motor area	MOp	Isocortex	985
Secondary motor area	MOs	Isocortex	993
Supplemental somatosensory area	SSs	Isocortex	378
Gustatory areas	GU	Isocortex	1057
Visceral area	VISC	Isocortex	677
Dorsal auditory area	AUDd	Isocortex	1011
Primary auditory area	AUDp	Isocortex	1002
Posterior auditory area	AUDpo	Isocortex	1027
Ventral auditory area	AUDv	Isocortex	1018
Anterolateral visual area	VISal	Isocortex	402
Anteromedial visual area	VISam	Isocortex	394
Lateral visual area	VISl	Isocortex	409
Primary visual area	VISp	Isocortex	385
Posterolateral visual area	VISpl	Isocortex	425
posteromedial visual area	VISpm	Isocortex	533
Laterointermediate area	VISli	Isocortex	312782574
Postrhinal area	VISpor	Isocortex	312782628
Prelimbic area	PL	Isocortex	972
Infralimbic area	ILA	Isocortex	44
Anterior area	VISa	Isocortex	312782546
Rostrolateral visual area	VISrl	Isocortex	417
Temporal association areas	TEa	Isocortex	541
Perirhinal area	PERI	Isocortex	922
Ectorhinal area	ECT	Isocortex	895
Main olfactory bulb	MOB	Olfactory areas	507
Accessory olfactory bulb	AOB	Olfactory areas	151
Anterior olfactory nucleus	AON	Olfactory areas	159
Taenia tecta	TT	Olfactory areas	589

Name	Acronym	Parent Area	regionID
Dorsal peduncular area	DP	Olfactory areas	814
Piriform area	PIR	Olfactory areas	961
Nucleus of the lateral olfactory tract	NLOT	Olfactory areas	619
Piriform-amygdalar area	PAA	Olfactory areas	788
Postpiriform transition area	TR	Olfactory areas	566
Field CA1	CA1	Hippocampal formation	382
Field CA2	CA2	Hippocampal formation	423
Field CA3	CA3	Hippocampal formation	463
Dentate gyrus	DG	Hippocampal formation	726
Fasciola cinerea	FC	Hippocampal formation	982
Induseum griseum	IG	Hippocampal formation	19
Parasubiculum	PAR	Hippocampal formation	843
Postsubiculum	POST	Hippocampal formation	1037
Presubiculum	PRE	Hippocampal formation	1084
Subiculum	SUB	Hippocampal formation	502
Prosubiculum	ProS	Hippocampal formation	484682470
Hippocampo-amygdalar transition area	HATA	Hippocampal formation	589508447
Area prostriata	APr	Hippocampal formation	484682508
Claustrum	CLA	Cortical subplate	583
Lateral amygdalar nucleus	LA	Cortical subplate	131
Basolateral amygdalar nucleus	BLA	Cortical subplate	295
Basomedial amygdalar nucleus	BMA	Cortical subplate	319
Posterior amygdalar nucleus	PA	Cortical subplate	780
Caudoputamen	CP	Striatum	672
Nucleus accumbens	ACB	Striatum	56
Fundus of striatum	FS	Striatum	998
Olfactory tubercle	OT	Striatum	754
Septofimbrial nucleus	SF	Striatum	310
Septohippocampal nucleus	SH	Striatum	333
Anterior amygdalar area	AAA	Striatum	23
Bed nucleus of the accessory olfactory tract	BA	Striatum	292
Central amygdalar nucleus	CEA	Striatum	536
Intercalated amygdalar nucleus	IA	Striatum	1105
Medial amygdalar nucleus	MEA	Striatum	403
Substantia innominata	SI	Pallidum	342
Magnocellular nucleus	MA	Pallidum	298
Medial septal nucleus	MS	Pallidum	564
Diagonal band nucleus	NDB	Pallidum	596
Triangular nucleus of septum	TRS	Pallidum	581
Bed nuclei of the stria terminalis	BST	Pallidum	351
Bed nucleus of the anterior commissure	BAC	Pallidum	287
Ventral anterior-lateral complex of the thalamus	VAL	Thalamus	629
Ventral medial nucleus of the thalamus	VM	Thalamus	685
Ventral posterolateral nucleus of the thalamus	VPL	Thalamus	718
Ventral posteromedial nucleus of the thalamus	VPM	Thalamus	733
Posterior triangular thalamic nucleus	PoT	Thalamus	563807435
Subparafascicular area	SPA	Thalamus	609
Peripeduncular nucleus	PP	Thalamus	1044
Medial geniculate complex	MG	Thalamus	475
Dorsal part of the lateral geniculate complex	LGd	Thalamus	170
Lateral posterior nucleus of the thalamus	LP	Thalamus	218
Posterior complex of the thalamus	PO	Thalamus	1020
Posterior limiting nucleus of the thalamus	POL	Thalamus	1029
Suprageniculate nucleus	SGN	Thalamus	325
Anteroventral nucleus of thalamus	AV	Thalamus	255
Anteromedial nucleus	AM	Thalamus	127
Anterodorsal nucleus	AD	Thalamus	64
Interanteromedial nucleus of the thalamus	IAM	Thalamus	1120
Interanterodorsal nucleus of the thalamus	IAD	Thalamus	1113
Lateral dorsal nucleus of thalamus	LD	Thalamus	155
Intermediodorsal nucleus of the thalamus	IMD	Thalamus	59
Mediodorsal nucleus of thalamus	MD	Thalamus	362
Submedial nucleus of the thalamus	SMT	Thalamus	366
Perireunensis nucleus	PR	Thalamus	1077
Paraventricular nucleus of the thalamus	PVT	Thalamus	149

Name	Acronym	Parent Area	regionID
Parataenial nucleus	PT	Thalamus	15
Nucleus of reuniens	RE	Thalamus	181
Xiphoid thalamic nucleus	Xi	Thalamus	560581559
Rhomboid nucleus	RH	Thalamus	189
Central medial nucleus of the thalamus	CM	Thalamus	599
Paracentral nucleus	PCN	Thalamus	907
Central lateral nucleus of the thalamus	CL	Thalamus	575
Parafascicular nucleus	PF	Thalamus	930
Posterior intralaminar thalamic nucleus	PIL	Thalamus	560581563
Reticular nucleus of the thalamus	RT	Thalamus	262
Intergeniculate leaflet of the lateral geniculate complex	IGL	Thalamus	27
Intermediate geniculate nucleus	IntG	Thalamus	563807439
Ventral part of the lateral geniculate complex	LGv	Thalamus	178
Subgeniculate nucleus	SubG	Thalamus	321
Medial habenula	MH	Thalamus	483
Lateral habenula	LH	Thalamus	186
Supraoptic nucleus	SO	Hypothalamus	390
Accessory supraoptic group	ASO	Hypothalamus	332
Paraventricular hypothalamic nucleus	PVH	Hypothalamus	38
Arcuate hypothalamic nucleus	ARH	Hypothalamus	223
Anterodorsal preoptic nucleus	ADP	Hypothalamus	72
Anteroventral preoptic nucleus	AVP	Hypothalamus	263
Anteroventral periventricular nucleus	AVPV	Hypothalamus	272
Dorsomedial nucleus of the hypothalamus	DMH	Hypothalamus	830
Median preoptic nucleus	MEPO	Hypothalamus	452
Medial preoptic area	MPO	Hypothalamus	523
Vascular organ of the lamina terminalis	OV	Hypothalamus	763
Posterodorsal preoptic nucleus	PD	Hypothalamus	914
Parastrial nucleus	PS	Hypothalamus	1109
Subparaventricular zone	SBPV	Hypothalamus	347
Suprachiasmatic nucleus	SCH	Hypothalamus	286
Subfornical organ	SFO	Hypothalamus	338
Ventromedial preoptic nucleus	VMPO	Hypothalamus	576073699
Ventrolateral preoptic nucleus	VLPO	Hypothalamus	689
Anterior hypothalamic nucleus	AHN	Hypothalamus	88
Lateral mammillary nucleus	LM	Hypothalamus	210
Medial mammillary nucleus	MM	Hypothalamus	491
Supramammillary nucleus	SUM	Hypothalamus	525
Medial preoptic nucleus	MPN	Hypothalamus	515
Dorsal premammillary nucleus	PMd	Hypothalamus	980
Ventral premammillary nucleus	PMv	Hypothalamus	1004
Ventromedial hypothalamic nucleus	VMH	Hypothalamus	693
Posterior hypothalamic nucleus	PH	Hypothalamus	946
Lateral hypothalamic area	LHA	Hypothalamus	194
Lateral preoptic area	LPO	Hypothalamus	226
Preparasubthalamic nucleus	PST	Hypothalamus	356
Parasubthalamic nucleus	PSTN	Hypothalamus	364
Perifornical nucleus	PeF	Hypothalamus	576073704
Retrochiasmatic area	RCH	Hypothalamus	173
Subthalamic nucleus	STN	Hypothalamus	470
Tuberal nucleus	TU	Hypothalamus	614
Zona incerta	ZI	Hypothalamus	797
Median eminence	ME	Hypothalamus	10671
Inferior colliculus	IC	Midbrain	4
Nucleus of the brachium of the inferior colliculus	NB	Midbrain	580
Nucleus sagulum	SAG	Midbrain	271
Parabigeminal nucleus	PBG	Midbrain	874
Midbrain trigeminal nucleus	MEV	Midbrain	460
Subcommissural organ	SCO	Midbrain	599626923
Ventral tegmental area	VTA	Midbrain	749
Paranigral nucleus	PN	Midbrain	607344830
Midbrain reticular nucleus	MRN	Midbrain	128
Periaqueductal gray	PAG	Midbrain	795
Anterior pretectal nucleus	APN	Midbrain	215
Medial pretectal area	MPT	Midbrain	531

Name	Acronym	Parent Area	regionID
Nucleus of the optic tract	NOT	Midbrain	628
Nucleus of the posterior commissure	NPC	Midbrain	634
Olivary pretectal nucleus	OP	Midbrain	706
Posterior pretectal nucleus	PPT	Midbrain	1061
Cuneiform nucleus	CUN	Midbrain	616
Red nucleus	RN	Midbrain	214
Oculomotor nucleus	III	Midbrain	35
Medial accesory oculomotor nucleus	MA3	Midbrain	549009211
Edinger-Westphal nucleus	EW	Midbrain	975
Trochlear nucleus	IV	Midbrain	115
Paratrochlear nucleus	Pa4	Midbrain	606826663
Ventral tegmental nucleus	VTN	Midbrain	757
Anterior tegmental nucleus	AT	Midbrain	231
Lateral terminal nucleus of the accessory optic tract	LT	Midbrain	66
Dorsal terminal nucleus of the accessory optic tract	DT	Midbrain	75
Medial terminal nucleus of the accessory optic tract	MT	Midbrain	58
Pedunculopontine nucleus	PPN	Midbrain	1052
Interfascicular nucleus raphe	IF	Midbrain	12
Interpeduncular nucleus	IPN	Midbrain	100
Rostral linear nucleus raphe	RL	Midbrain	197
Central linear nucleus raphe	CLI	Midbrain	591
Dorsal nucleus raphe	DR	Midbrain	872
Nucleus of the lateral lemniscus	NLL	Pons	612
Principal sensory nucleus of the trigeminal	PSV	Pons	7
Parabrachial nucleus	PB	Pons	867
Superior olivary complex	SOC	Pons	398
Barrington's nucleus	B	Pons	280
Dorsal tegmental nucleus	DTN	Pons	880
Posterodorsal tegmental nucleus	PDTg	Pons	599626927
Pontine central gray	PCG	Pons	898
Pontine gray	PG	Pons	931
Supragenual nucleus	SG	Pons	318
Supratrigeminal nucleus	SUT	Pons	534
Tegmental reticular nucleus	TRN	Pons	574
Motor nucleus of trigeminal	V	Pons	621
Peritrigeminal zone	P5	Pons	549009215
Accessory trigeminal nucleus	Acs5	Pons	549009219
Parvicellular motor 5 nucleus	PC5	Pons	549009223
Intertrigeminal nucleus	I5	Pons	549009227
Superior central nucleus raphe	CS	Pons	679
Locus ceruleus	LC	Pons	147
Laterodorsal tegmental nucleus	LDT	Pons	162
Nucleus incertus	NI	Pons	604
Pontine reticular nucleus	PRNr	Pons	146
Nucleus raphe pontis	RPO	Pons	238
Subceruleus nucleus	SLC	Pons	350
Sublaterodorsal nucleus	SLD	Pons	358
Area postrema	AP	Medulla	207
Dorsal cochlear nucleus	DCO	Medulla	96
Ventral cochlear nucleus	VCO	Medulla	101
Cuneate nucleus	CU	Medulla	711
Gracile nucleus	GR	Medulla	1039
External cuneate nucleus	ECU	Medulla	903
Nucleus of the trapezoid body	NTB	Medulla	642
Nucleus of the solitary tract	NTS	Medulla	651
Paratrigeminal nucleus	Pa5	Medulla	589508451
Abducens nucleus	VI	Medulla	653
Facial motor nucleus	VII	Medulla	661
Accessory facial motor nucleus	ACVII	Medulla	576
Nucleus ambiguus	AMB	Medulla	135
Dorsal motor nucleus of the vagus nerve	DMX	Medulla	839
Gigantocellular reticular nucleus	GRN	Medulla	1048
Infracerebellar nucleus	ICB	Medulla	372
Inferior olivary complex	IO	Medulla	83
Intermediate reticular nucleus	IRN	Medulla	136

Name	Acronym	Parent Area	regionID
Inferior salivatory nucleus	ISN	Medulla	106
Linear nucleus of the medulla	LIN	Medulla	203
Lateral reticular nucleus	LRN	Medulla	235
Magnocellular reticular nucleus	MARN	Medulla	307
Medullary reticular nucleus	MDRN	Medulla	395
Parvicellular reticular nucleus	PARN	Medulla	852
Parasolitary nucleus	PAS	Medulla	859
Nucleus of Roller	NR	Medulla	177
Nucleus prepositus	PRP	Medulla	169
Parapyramidal nucleus	PPY	Medulla	1069
Lateral vestibular nucleus	LAV	Medulla	209
Medial vestibular nucleus	MV	Medulla	202
Spinal vestibular nucleus	SPIV	Medulla	225
Superior vestibular nucleus	SUV	Medulla	217
Nucleus x	x	Medulla	765
Hypoglossal nucleus	XII	Medulla	773
Nucleus y	y	Medulla	781
Nucleus raphe magnus	RM	Medulla	206
Nucleus raphe pallidus	RPA	Medulla	230
Nucleus raphe obscurus	RO	Medulla	222
Lingula (I)	LING	Cerebellum	912
Central lobule	CENT	Cerebellum	920
Culmen	CUL	Cerebellum	928
Declive (VI)	DEC	Cerebellum	936
Folium-tuber vermis (VII)	FOTU	Cerebellum	944
Pyramus (VIII)	PYR	Cerebellum	951
Uvula (IX)	UVU	Cerebellum	957
Nodulus (X)	NOD	Cerebellum	968
Simple lobule	SIM	Cerebellum	1007
Ansiform lobule	AN	Cerebellum	1017
Paramedian lobule	PRM	Cerebellum	1025
Copula pyramidis	COPY	Cerebellum	1033
Paraflocculus	PFL	Cerebellum	1041
Flocculus	FL	Cerebellum	1049
Fastigial nucleus	FN	Cerebellum	989
Interposed nucleus	IP	Cerebellum	91
Dentate nucleus	DN	Cerebellum	846
Vestibulocerebellar nucleus	VeCB	Cerebellum	589508455
fiber tracts	fiber tracts	root	1009